



2006-01-25

Fuel-NO_x Formation during Low-Grade Fuel Combustion in a Swirling-Flow Burner

Chunyang Wu

Brigham Young University - Provo

Follow this and additional works at: <http://scholarsarchive.byu.edu/etd>

 Part of the [Chemical Engineering Commons](#)

Recommended Citation

Wu, Chunyang, "Fuel-NO_x Formation during Low-Grade Fuel Combustion in a Swirling-Flow Burner" (2006). *All Theses and Dissertations*. Paper 352.

This Dissertation is brought to you for free and open access by BYU ScholarsArchive. It has been accepted for inclusion in All Theses and Dissertations by an authorized administrator of BYU ScholarsArchive. For more information, please contact scholarsarchive@byu.edu.

FUEL-NO_x FORMATION DURING LOW-GRADE FUEL
COMBUSTION IN A SWIRLING-FLOW BURNER

by

Chunyang Wu

A dissertation submitted to the faculty of

Brigham Young University

in partial fulfillment of the requirement for the degree of

Doctor of Philosophy

Department of Chemical Engineering

Brigham Young University

April 2006

Copyright © 2006 Chunyang Wu

All Rights Reserved

BRIGHAM YOUNG UNIVERSITY

GRADUATE COMMITTEE APPROVAL

of a dissertation submitted by

Chunyang Wu

This dissertation has been read by each member of the following graduate committee and by major vote has been found to be satisfactory

Date

Larry L. Baxter, Chair

Date

Dale R. Tree

Date

Merrill M. Beckstead

Date

William C. Hecker

Date

John L. Oscarson

BRIGHAM YOUNG UNIVERSITY

As chair of the candidate's graduate committee, I have read the dissertation of Chunyang Wu in its final form and have found that (1) its format, citations, and bibliographical style are consistent and acceptable and fulfill university requirements; (2) its illustrative materials including figures, tables, and charts are in place; and (3) the final manuscript is satisfactory to the graduate committee and is ready for submission to the university library.

Date

Larry L. Baxter
Chair, Graduate Committee

Accepted by the Department

William G. Pitt
Graduate Coordinator

Accepted for the college

Alan R. Parkinson
Dean, Ira A. Fulton College of Engineering and
Technology

ABSTRACT

FUEL-NO_x FORMATION DURING LOW-GRADE FUEL COMBUSTION IN A SWIRLING-FLOW BURNER

Chunyang Wu

Department of Chemical Engineering

Doctor of Philosophy

Insufficient knowledge of fireside behavior in the near-burner region during biomass combustion is one of major factors preventing widespread use of this renewable fuel in pulverized coal power plants. The current research is aimed to investigate the impact of biomass cofiring on NO formation in the near-burner region through interpretation of computational fluid dynamics (CFD) predictions and data collected from a series of biomass tests in a pilot-scale (0.2 MW), swirling flow burner.

Two-dimensional gas species mole fraction data were collected with state-of-the-art instruments from nine experiments, composing one herbaceous biomass (straw), one woody biomass (sawdust), a low sulfur sub-bituminous coal (Blind Canyon) and a high sulfur bituminous coal (Pittsburgh #8) and their mixtures of different mass fractions with the same swirl setting. Velocity and temperature are calculated from CFD modeling with

FLUENTTM, supplemented with hot-wire anemometer measurements. For the first time, a reverse flow region was predicted during solid fuel combustion simulations for the reactor used.

Interpretation of the results was carried on with two original methods: stoichiometric maps and normalized species mole fraction profiles. The impacts of biomass on combustion in the swirling flows were analyzed from several aspects: aerodynamics, fuel properties (particle size, volatile content, and fix-carbon content), and NO formation routes.

The species maps show the low-grade fuel combustion under swirling flows is composed of two zones: a high species-gradient combustion region attached to the inlet and flat-profiles dominant across the rest of the reactor. Results from tests involving biomass clearly demonstrate the expansion of the combustion region. CFD calculations demonstrate that there is no obvious alteration of the reverse-flow region by biomass combustion. The larger average particle size of biomass generates a combustion region with further penetration into the reactor.

In certain tests involving biomass, more NH₃ than HCN was detected in several biomass experiments, though limited by the data collection method and low fuel-nitrogen fuels used (sawdust). Supplemented with kinetic calculations with CHEMKIN, it was found that NO formation is dependent on the nitrogen forms in the parent fuels.

ACKNOWLEDEMENTS

This research was generously supported by Brigham Young University Professorship and Elsam Technology Inc., Denmark. Sincere gratitude is expressed to Professor Larry L. Baxter for his invaluable guidance encouraging me to progress in the field of combustion engineering. I greatly appreciate tremendous precious advice from Professor Dale R. Tree during the experiments. Special thanks to Bradley Damstedt for his assistance in facility refurbishments and during the experiments, and I wish him the best luck in completing his dissertation. I am thankful to Dr. Karthik Pudappakkam and Dr. Søren Knudsen Kær for their help in the combustion modeling. I appreciate the assistance from the Department of Chemical Engineering and Advanced Combustion Engineering Research Center at Brigham Young University.

Dedicated to my family, the completion of this work is one of the best ways to show my wholehearted gratitude to my parents and especially my wife, Ying Gao, for their immense support from all aspects.

Table of Contents

List of Tables	x
List of Figures	xi
Chapter 1 Introduction	1
Chapter 2 Literature Review	9
2.1 Generic swirling flow burner	9
2.2 Fuel-N conversion during low-grade fuel combustion.....	12
2.3 Experimental measurements and modeling results of swirling flows.....	21
2.4 Summary	31
Chapter 3 Research Objective.....	33
Chapter 4 Descriptions of Experiments	35
4.1. The Burner Flow Reactor (BFR)	35
4.2. Gas sampling apparatus	41
4.2.1. Sampling probe	41
4.2.2. Cyclone, particle filter, and heated gas path lines	42
4.2.3. Gas analyzers	42
4.3. Fuel selection and feeding system	45
4.4. Combustion experiment and data collection description.....	48
4.5. Safety issues.....	52
4.6. Summary	54
Chapter 5 Computational Fluid Dynamics (CFD) Calculations	55
5.1 Modeling purpose and strategy description.....	55
5.2 Modeling of the swirl-generator under cold-flow conditions	58
5.3 Combustion modeling description.....	63
5.4 Modeling strategy verification	66
5.5 Summary	72
Chapter 6 Results and Discussions	73
6.1 Consistency between the two analyzers	73
6.2 Description of the gas species profiles	76
6.2.1 Benchmark: pure coal test (Test BC)	77
6.2.2 Comparison of maps from biomass tests to that of Test BC	86
6.3 Experimental data analysis	89
6.3.1 Stoichiometric ratio maps.....	89
6.3.2 Gas species normalized mole fractions (1-D profile).....	92
6.4 Features of biomass combustion under swirling flows	93
6.4.1 Flow pattern.....	95

6.4.2 Influence of biomass properties: particle size and volatile content.....	98
6.5 NO _x formation during biomass combustion under swirling flows.....	104
6.5.1 Measurements of HCN and NH ₃	105
6.5.2 Analysis of NO emission data	113
6.5.3 1-D profiles of NO.....	122
6.5.4 Kinetic evidence on the fate of NO _x intermediates	123
6.5.5 Summary.....	130
Chapter 7 Summary and Conclusion	133
Chapter 8 Research Limitation and Recommendations.....	137
References.....	141
Appendices.....	151
Appendix A. Literature review on NO _x from low-grade fuel combustion.....	153
Generation classification of NO _x formation from combustion	153
Modeling in fuel-NO _x research	155
Detailed gas-phase kinetic schemes involving fuel-N chemistry	156
Reduced fuel-N kinetic models	159
Fuel-nitrogen chemistry in biomass gasification and reburning	160
Present status of biomass cofiring	162
Technical barriers of cofiring	165
NO _x from cofiring.....	170
Appendix B. Recasting the refractory liner in the BFR	173
Overview	173
Safety Issues	173
Equipment	173
Execution.....	174
Finishing Up.....	176
Appendix C. Calibration of coal and biomass feeders	177
Appendix D. Calibration of air and natural feed rates.....	179
Appendix E. Description of the sampling probe.....	181
Appendix F. Description of the cyclone and mount	185
Appendix G. CFD calculation description	187
Three dimensional modeling.....	187
Two dimensional combustion modeling	191
Continuous phase.....	191
Discrete phase.....	196
Particle tracking.....	196
Devolatilization	197
Char oxidation	200
NO _x formation mechanism.....	201
Appendix H. Additional cofiring maps	207
Appendix I. Derivation of the species profiles modification equation	211
Appendix J. Kinetics calculations with the GRI-Mech 3.0 mechanism.....	215

List of Tables

Table 2.1	Experiment data shows NH ₃ concentrations are much higher than HCN in the pyrolysis of selected biomass fuels (Brink et al. 2001)	17
Table 4.1	Interference table of the Horiba gas analyzer (HoribaInc. 2000)	45
Table 4.2	The physical properties of the fuels used in the current project.	47
Table 4.3	Experiment layout for the tests with different fuels and their mass ratios....	47
Table 4.4	The set-up feed rate of fuel and air flow rates under the test conditions.	48
Table 4.5	The response time of both analyzers under the testing conditions (unit: minute).	51
Table 5.1	Composition and thermal properties inputs during the cofiring PDF calculations.	64
Table 5.2	Parameters selected and inputs in the combustion modeling.....	66
Table 6.1	NO emissions in the reacted-gas region during current project.....	118
Table 6.2	Compositions of the initial gas mixtures in the kinetic simulations	126

List of Figures

Figure 2.1	Operating scheme of a non-premixed swirling flow burner	10
Figure 2.2	The conversion of fuel nitrogen versus nitrogen contents of different fuels.....	14
Figure 2.3	Molecular structures of pyridine, pyrrole, benzene, amide and amine	17
Figure 2.4	Reaction path diagram illustrating major steps in volatile-N conversion in flames for HCN and NH ₃ at moderate fuel-N concentrations (Glarborg et al. 2003).	21
Figure 2.5	Mean axial velocity contours at three swirl settings: 0 (left), 0.5 (middle), and 1.5 (right) (Pickett et al. 1999).	24
Figure 2.6	Temperature (K) contours with different swirl settings, adapted from (Tree et al. 1998).....	25
Figure 2.7	Contours of mean CO ₂ mole concentration (%) (Tree 2002).	26
Figure 2.8	Contours of mean CO mole concentrations (ppm) under different swirl settings, adapted from (Tree 2002)	27
Figure 2.9	Contours of mean O ₂ mole concentration (%) under different swirl settings, adapted from (Tree 2002).	27
Figure 2.10	Contours of mean NO mole concentrations (ppm) under different swirl settings, adapted from (Tree 2002).	28
Figure 2.11	Qualitative description of the flames (Ballester et al. 2005).	30
Figure 2.12	Contours of O ₂ molar concentrations (%) from oak sawdust flame (a) and the bituminous flame (b) (Ballester et al. 2005).	30
Figure 2.13	Contours of NO _x molar concentrations (ppm, vol, db) from oak sawdust flame (a) and the bituminous flame (b) (Ballester et al. 2005).	31
Figure 4.1	BFR system and the combustion chamber.....	37
Figure 4.2	The burner cross section (top) and the lower plate of the swirl-generator (bottom): the center hole is the fluid path, and the triangles are the vanes.....	38
Figure 4.3	Description of the gas sampling system with the BFR.	43
Figure 4.4	The lines represent the measurement locations at different axial distance (cm) from the inlet, where the reactor body meets the cooling water quarl is defined as the zero line.....	52
Figure 5.1	General description of continuous volume during the cold flow modeling: left: the whole reactor of the BFR, with the modeled reactor volume of 1/8 highlighted; right top: a general view of the swirl-generator and the modeled part; right bottom: modeled volume of the swirl-generator, primary air path line and cooling	

	water quarl. A. Primary air/fuel inlet; B. Secondary air inlet; C. vanes of the swirl-generator; D. Wall of primary air pipe.	59
Figure 5.2	Grid set-up in the 3-D CFD calculation. Top: swirl-generator and cooling water quarl; bottom: BFR body.	60
Figure 5.3	Comparison of the 3-D CFD predictions and the available cold flow LDV data (Pickett et al. 1999) at different axial distances from the end of the primary pipe, operating conditions: a primary air feed rate of 15.6 kg/hr and a secondary feed rate of 175 kg/hr, swirl number = 1.5.	62
Figure 5.4	Comparison of the hot-wire anemometer data with 3-D CFD predictions 15 cm below the zero plane.	63
Figure 5.5	Grids set-up in the near inlet region of the axisymmetric combustion models.	65
Figure 5.6	Axial velocity contours in the Black Thunder simulations ($\phi = 1.1$, swirl number = 1.5).	67
Figure 5.7	Comparison of the hot-flow axial, tangential velocity profiles from the CFD prediction and the LDV data at different axial distances (15 cm and 30 cm) (Tree 2002) during the Black Thunder test ($\phi = 1.1$, swirl number = 1.5).	68
Figure 5.8	Comparison of the hot-flow axial, tangential velocity profiles from the CFD prediction and the LDV data at different axial distances (55 cm and 71 cm) (Tree 2002) during the Black Thunder test ($\phi = 1.1$, swirl number = 1.5).	68
Figure 5.9	Comparison of the gas flow temperature profiles from the CFD prediction and the experimental data at different axial distances (Nazeer 1997) during the Black Thunder test ($\phi = 1.1$, swirl number = 1.5).	70
Figure 6.1	Comparison of the real-time reading at the same position by the Horiba and MKS analyzers: SO ₂ and CO ₂ , during one cofiring case only (50% straw 50% Blind Canyon) and three cases (straw, Blind Canyon, and 70% straw 30% Blind Canyon), respectively.	74
Figure 6.2	Comparison of the real-time reading at the same position by the Horiba and MKS analyzers: CO and NO during three cases (straw, Blind Canyon, and 70% straw 30% Blind Canyon).	75
Figure 6.3	Comparison of major species contours from two Blind Canyon tests under same operating conditions. Both fuel and air entries locate at the top of the reactor, and the radial location unit is cm.	79
Figure 6.4	CFD prediction contours of streamline functions, axial velocity, reverse flow, gas-phase temperature, and major species (O ₂ , CO, and CO ₂) volume fractions from simulation of Test BC in the BFR.	80
Figure 6.5	Results of replicate NO, O ₂ , CO ₂ , and CO measurements during two Blind Canyon tests positioned at an axial distance of 12 cm below the zero line (on a 3% O ₂ basis).	84
Figure 6.6	Species maps of the two pure biomass: Test S (straw) and Test SD (sawdust)	87
Figure 6.7	Species maps of the two cofiring tests: Test 50S50BC (50% straw	

	and 50% Blind Canyon, wt) and Test 70S30BC (70% straw and 30% Blind Canyon, wt).....	91
Figure 6.8	Contours of CO, CO ₂ and axial reverse flow velocity from simulations of straw combustion.	94
Figure 6.9	Contours of CO, CO ₂ and axial reverse flow velocity from simulations of Blind Canyon combustion.....	95
Figure 6.10	The reverse flow contours (m/s) predicted from simulations of the pure fuel tests.	96
Figure 6.11	Comparison of reverse flow contours from the two cofiring tests and their corresponding pure fuel tests involving straw and Blind Canyon.	97
Figure 6.12	Distribution of particle size of biomass and coal used.	98
Figure 6.13	Comparisons of CFD predictions top: CO (ppm); bottom: CO ₂ (vol %) of Test BC, Test SD, and Test S.	100
Figure 6.14	1-D profiles of CO (top), CO ₂ (middle), and O ₂ (bottom) during pure fuel tests (The dot-lines describe the trends of normalized results of Test BC along the reactor axis).....	101
Figure 6.15	Stoichiometric ratio maps of the test of Blind Canyon coal and cofiring tests calculated based on Equation 6.3.....	103
Figure 6.16	1-D profiles of CO (top), CO ₂ (middle), and O ₂ (bottom) during cofiring tests compared to that of Test BC (The lines show the trend of the normalized results of Test BC along the reactor axis)	104
Figure 6.17	Temporal variations in NH ₃ and HCN concentrations compared to CO concentration in the swirling section of the BFR. (a) NH ₃ with CO during Test S (b) HCN with CO during Test BC.	107
Figure 6.18	Two dimensional maps of HCN and NH ₃ from Test BC. NH ₃ data are below detection limits and the indicated patterns are not significant.....	108
Figure 6.19	NH ₃ and HCN maps from Test S, Test 70S30BC, and Test 50S50 BC. The unit of radial distance from the centerline is cm.	109
Figure 6.20	NH ₃ and HCN maps from Test SD. The unit of radial distance from the centerline is cm.	110
Figure 6.21	Comparison of NH ₃ and HCN data at same position from Test SD and Test P.....	110
Figure 6.22	NH ₃ and HCN maps from Test 70SD30P. The unit of radial distance from the centerline is cm.	111
Figure 6.23	The modified HCN and NH ₃ spatial profiles from the tests of Blind Canyon, straw and their cofiring mixtures based on Equation 6.4, with the assumption that the fuel-lean eddies are pure air.....	113
Figure 6.24	Comparison of axisymmetric NO maps (unit: ppm).....	116
Figure 6.25	The relation between the measured and the interpolated NO emissions (mole fraction on a 3% excess O ₂ basis) in the present project.....	121
Figure 6.26	The relation between the measured and the interpolated NO emissions in a non-swirling flow burner. (Baxter 2002)	121
Figure 6.27	NO 1-D profiles from pure fuel tests (a) and cofiring tests (b)	

	(The lines show the trends of normalized results of Test BC along the reactor axis).....	123
Figure 6.28	Comparison the thermal stability of HCN and NH ₃ in the fuel-rich region with the Kilpinen 97 mechanism.	128
Figure 6.29	Comparison the chemical stability of HCN (Case 2) and NH ₃ (Case 3) in the flame front with the Kilpinen 97 mechanism.	129
Figure 6.30	Calculated profiles of TFN and NO from cases where only one type of NO _x intermediate exists in the initial mixture, with lines representing results from HCN mixtures (Case 2) and markers denoting NH ₃ blends (Case 3) with the Kilpinen 97 mechanism.	131

Chapter 1 Introduction

Energy represents one of the most critical and ubiquitous resources for all stages of human development. At the start of the twenty-first century, 85% of the total energy supplies were produced by combustion in all regions of the world. The primary non-combustion sources of energy, such as nuclear, hydroelectric, wind, solar, and hydrothermal, are anticipated to produce limited or smaller rather than larger supplies in the future. Therefore, combustion is and will be one of the most significant engineering processes impacting both national and global interests, and combustion will retain this dominant role for the foreseeable future.

Several fundamental social interests, including the environment, economics, security, political interdependencies, and sustainability, are impacted by combustion. Contemporary combustion research focuses on following objectives:

1. Reducing operating costs, including increasing the burning efficiency and lowering the cost of fuels or the flexibility of systems to accommodate a wide range (and price) of fuels
2. Minimizing the emission of pollutants from combustion processes. Data (PowerScorecard 2000) show that the generation of electric power produces more pollution than any other single industry in the United States, accounting for:

- 67% of sulfur dioxide emissions that contributes to *acid rain* and *small particle/aerosol* formation
- 25% of NO_x emissions that contribute to *urban smog*, *small particle*, and *ground-level ozone* generation
- 40% of carbon dioxide emissions that contributes to potential *global climate change*

3. Maximizing availability/reliability of equipment to provide uninterrupted power with minimal scheduled shutdown time and minimal risk of unscheduled shutdowns

Over the last 30 years, most of the developed world has made tremendous progress in reducing the environmental impacts of combustion systems; In the US, for example, the average pollutant emissions were reduced 25% even as energy use was increased by over 40% (EPA 2000). This trend will continue, driven by increasingly stringent environmental regulations and innovative technological solutions for the next two decades with respect to traditional pollutants (SO_x, NO_x, heavy metals, etc.). However, environmental concerns centering on potential global climate change, greenhouse gas emission in particular, are emerging as a new and major issue for combustion processes. These concerns represent much more challenging issues for combustion than have traditional pollutants, because over 85% of the green house gases are CO₂, the major combustion product, rather than fuel impurities like nitrogen, sulfur, and ash-forming inorganic materials. Successful resolution of greenhouse gas issues will require more innovative engineering and will probably come at higher economic and energy costs than is typical for traditional pollutants. Substitution of fossil fuels with renewable energy sources represents one of the most promising methods. Biomass is

among the most plentiful and inexpensive forms of renewable energy. The motivation for this research is to improve our understanding of co-firing coal and biomass to achieve more fuel flexibility while decreasing emissions of both impurities and greenhouse gases while utilizing existing facilities.

Fossil-derived fuels play a dominant role in the power-generation industry. Petroleum and natural gas continue to be the most convenient fuels because of their relatively low cost as well as ease of handling and combustion. Coal has been one of the dominant fuels since the industrial revolution because of its high heating value, widespread abundance, relatively low cost, and easy processing. Worldwide resources of crude oil and natural gas may only last for another century, while coal reserves could possibly last for several centuries at present consumption rates (Coda Zabetta 2002). Coal-fired power plants produce over half of the electricity in many industrialized and developing countries. In the U.S., the fleet of over 400 coal plants is responsible for more than 50 percent, about 2 billion megawatthours, of electricity in 2002 (DOE 2003). Coal combustion yields diverse emissions. Coal power plants are presently responsible for 90% of sulfur oxides, 80% of nitrogen oxides (NO_x), and 80% of carbon dioxide emissions associated with electricity generation (DOE 2003), although it produces only 53% of the power. The large quantities of coal consumption (approximately 1 billion tons/yr in the US) make coal a dominant contributor of anthropogenic emissions of traditional pollutants and will demand that significant solutions for coal-related issues be deployable at large scale and in broad application. Driven by the political and social concerns about the environmental impacts caused by using fossil fuels, renewable energy supplementary power is highly encouraged by many industrial countries. One of the most

promising candidates is biomass, which can provide a sound and economic approach to both waste reduction and energy production since the thermal processing equipment for biomass and coal is similar.

Firing biomass is an effective method to combat global warming and to reduce reliance on imported energy sources. The term “biomass” encompasses diverse fuels derived from timber, agriculture and food processing wastes, municipal waste, sewage sludge, animal manure, animal products, and energy crops that are specifically grown or reserved for electricity generation.

The capital investment for a dedicated biomass power plant is high. This can be avoided by cofiring or simultaneously firing biomass as a supplementary fuel with the base fuel in existing coal-fired facilities. Cofiring increases fuel diversity and takes advantage of the relatively high efficiencies obtainable in coal-fired power plants. Furthermore, this method reduces emission of greenhouse gases and can reduce other pollutants from power generating facilities.

Biomass and coal have fundamentally different fuel properties. For instance, biomass is generally a more volatile fuel and has higher oxygen content than coal. Biomass typically contains less sulfur than coal, which translates into lower sulfur emissions as higher blending ratios of biomass are used. Finally, the use of biomass can mitigate CO₂ emission and the emission of other traditional pollutants. The CO₂ emissions from fossil fuel combustion represent an environmental threat without a current commercial control technology except fuel switching. By contrast, in sustainable biomass-fired systems, carbon dioxide is consumed during plant growth at the same rate it is produced. An important point is that it is the sustainable growth of biomass that

makes it CO₂ neutral, not an inherent property of biomass. Indeed, biomass combustion produces slightly more CO₂ per unit energy than coal combustion in most cases (Baxter 2002). In a sustainable process, the CO₂ is captured as soon as it is generated. Furthermore, sulfur can be trapped in the ash in the form of alkali and alkaline earth compounds. Clean biomass fuels have very low concentrations of heavy metals, although some forms of biomass fuels, notably municipal waste and demolition waste, may have high heavy metal concentrations. At present, most biomass power plants burn wood-based material derived from the lumber/paper industries, agricultural byproducts, or construction/demolition wood wastes. Given the capacity for plants to regenerate, these fuels are considered to be renewable. Biomass provides 12% of the energy in combustion worldwide, while in industrialized countries it provides less than 3% (Dayton 2002b), which demonstrates its potential as a dominant energy reserve.

Biomass currently represents the second largest amount of renewable energy in US behind hydrothermal power. However, biomass has many disadvantages compared to fossil fuels. Its physical form is rarely homogeneous, and the energy density is commonly 1/10 or less than that of coal on an as-received basis. Some biomass fuels (especially some grasses and straws) include potassium and chlorine in forms that are more reactive than coal, which leads to greater high-temperature corrosion and accelerated fouling and slagging in boilers. NO_x emissions, typically lower than coal for wood-based systems but sometimes exacerbated by high-nitrogen in some herbaceous biomass fuels, set process limits for several commercial biomass power plants.

Swirling flows facilities are among the most widely used NO_x reduction devices associated with commercial-scale coal combustion facilities, because of their benefits to

combustion efficiency, ignition and flame stability and emissions reduction (Arai 2000; Correa 1998; Kitto et al. 1998) . An understanding of fuel nitrogen in coal and the process by which NO formation from fuel nitrogen is reduced has been discussed extensively in the literature. Global and detailed mechanisms have been written to describe the nitrogen evolution (Alzueta et al. 1998; Brink et al. 2001; Coda Zabetta et al. 2000). Data obtained from pilot- or commercial-scale tests involving nitrogen evolution with coal/biomass co-firing under swirling flows are scarce (Ballester et al. 2005). The mechanisms involved in this process are not completely understood. The issues are summarized as follows.

1. Combustion conditions and fuel characteristics are among the major factors affecting NO_x emissions. One of the major difficulties in predicting NO_x formation is an estimation of the nitrogen released in the volatiles compared to nitrogen remaining in the char (Wargadalam et al. 2000). Biomass generally creates more volatiles, has higher oxygen content, and in the case of wood, usually generates much less ash than coal. Devolatilization reactions dominate the combustion process. Because of the difference in physical properties and chemical behaviors, coal devolatilization models are not useful for biomass without significant modification. Compared to coal, nitrogen release from the fuel proceeds at a different rate and produces different primary species and may be surrounded by various other volatiles which alter the path to NO_x formation relative to coal.

2. The formation of stable NO_x precursors, HCN and NH₃, and the ultimate NO_x concentrations from biomass and coal is possibly impacted by the coal swirling flows when firing biomass and biomass-coal blends (Baxter 2002). The effect of fuel-nitrogen

(fuel-N) functional groups on the ultimate production of NH_3 and HCN is uncertain. For coal, it is commonly recognized that HCN dominates stable primary gas-phase compounds during devolatilization. By contrast, biologically active nitrogen (typically amines) in biomass thermally decomposes to form primarily NH_3 . The fuel-N content in some commonly used biomass derived from biologically inactive materials is too low to be analyzed. Commercial tests show there is a high degree of variability and lack of reproducibility in NO_x emissions, limiting reliable information data.

3. Some industrial processes chemically similar to homogeneous reactions involved in biomass swirling flow operations, such as reburning and combustion of biomass gasification gases in gas turbines, can be predicted very well by detailed-chemistry and ideal flow reactor models (Glarborg et al. 2000). However, the flow pattern in a coal burner is nearly always swirl-stabilized and turbulent, requiring a detailed description of the flow dynamics to gain a correct understanding of formation mechanisms. Current technology can't reliably quantify velocities and temperature in the flow region in industrial-scale combustion facilities.

4. When co-firing biomass, flow patterns of combustion gases through the boiler can be dramatically modified. There may be insignificant chemical interaction between the off-gases from biomass and coal that would alter NO_x emissions. These unclear factors limit the percentage of biomass that can be cofired. Wood-based and herbaceous biomass represent the most common fuels in commercial use. The application of cofiring these fuels in mass fractions of 10 to 30% demonstrates alternative environmental benefits if cofiring can be deployed economically and technically as a system that avoids the cost of installing and operating some other NO_x control system (Ekman et al. 1998). However,

a larger fraction of these fuels in commercial cofiring is limited by many factors, including difficulty in feeding and handling, carbon burnout, emissions, and ash managements. Experimental data with cofiring of high biomass fractions (>50% on a mass basis) are very scarce.

The purpose of the current research is to provide species profiles of major gas species and stable nitrogen compounds in a pilot-scale, swirl-stabilized burner reactor from a series of biomass cofiring tests. A matrix of fuel combinations includes coal and biomass, with a latter's mass fraction up to 100% and 70% in blends. Modeling and limited velocity measurements were used to describe the flow within the reactor. This work increase understanding of gas-phase chemistry and flame structure during biomass firing/cofiring in swirling flow burners under conditions of practical interests.

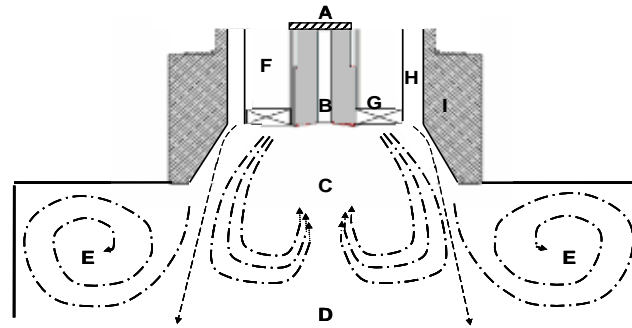
Chapter 2 Literature Review

This part is organized as follows: first, a brief description of the swirling flow burner. Second, NO_x formation from fuel-bound nitrogen during low-grade fuel combustion, especially the origination and consumption of the important intermediates (HCN and NH_3), is described. Third, available data from research on the swirling flow low-grade fuel combustion are summarized. Since biomass has such a big family, as mentioned earlier, only plant-derived fuels, such as wood-based and herbaceous biomass, are considered in this project.

2.1 Generic swirling flow burner

Swirling flow combustion is the subject of intensive experimental and numerical modeling investigations (Zhang and Nieh 2000). Figure 2.1 depicts the operating scheme of a non-premixed swirling flow burner. Before entering the burner, a homogeneous coal flow is produced by the distributor, limiting an increase in fly ash loss-on-ignition (LOI, referring to the unburned carbon in the fly ash). The fuel is drawn by the primary air through the axial injector. Secondary air enters the burner passing through the swirl-generator. When the swirl intensity is high enough, generally with a swirl number (the ratio of tangential momentum to axial momentum) higher than 0.6 (Frassoldati et al. 2005). As this swirl expands in the quarl, the tangential velocity decreases, resulting in an

increase of the centerline pressure in the direction of the flow. This adverse pressure gradient in the direction of the flow breaks down the vortex and forms a reverse flow region near the inlet, which is called internal recirculation zone (IRZ).



- A. Coal flow distributor
- B. Fuel with primary air
- C. Internal recirculation zone (IRZ)
- D. Reaction zone
- E. External recirculation zone (ERZ)
- F. Secondary air
- G. Swirl-generator
- H. Tertiary air
- I. Quarl

Figure 2.1 Operating scheme of a non-premixed swirling flow burner

Generally the IRZ occurs within one and a half burner diameters downstream of the fuel inlet (Kucukgokoglan et al. 2000). In the IRZ, the enhanced turbulence levels suppress the mixing of fuel and air during the initial stage of combustion, resulting in a locally stabilized, moderate-temperature, fuel-rich region, so thermal- NO_x (NO_x formed from oxidation of N_2) formation is minimized, and fuel-N-derived gases such as HCN and NH_3 convert to N_2 rather than NO in this reactive and reducing region (Solero et al. 2000).

Axi-symmetric flow is much easier to obtain under higher swirl numbers (>0.8) (Chen et al. 1999). Because of the wall confinements, reverse flows are also formed in the near-wall region and this is called external recirculation zone (ERZ), characterized by burnt gas flows (Smirnov 1995). The diverging inner surface of the swirl helps smooth the air flows and hold the flame. Overfire air can be injected through the tertiary air inlet, which flows downstream around the ERZ, and completes combustion in the reaction region (Abbas et al. 1994b).

Swirling flow burners achieve their sustained operation stability and optimal emission reduction performance through the combined interaction of homogeneous fuel feeding, appropriate air splitting, and the proper mixing degree of air/fuel in the ERZ (NETL 2005). Any imbalance will possibly cause burners to operate under over-rich or over-lean conditions.

The ultimate purpose of swirling flow combustion research is to provide optimal burner design to minimize NO_x emissions with high combustion efficiency (Widmann et al. 1999). Fuel- NO_x (NO_x generated from fuel-bound nitrogen) accounts for over 90% of the NO_x formed during coal (Zhang 2000) and biomass (Baxter 2002) combustion systems. Because NO is the major NO_x component in low-grade fuel combustion (Dayton 2002a; Pershing and Wendt 1977), the formation of other NO_x components such as NO_2 are neglected in the present study. NO formation during pulverized fuel combustion is a complex process. For a better understanding, a set of subprocesses need considering, including fuel devolatilization, volatile oxidation, char oxidation, flow characterization, and turbulence, etc. Many articles on these subprocesses are available (Abbas et al. 1994a; Beer and Chigier 1972; Chen et al. 1992; Chen and Niksa 1992; De Soete 1975; Eatough

and Smoot 1996; Epple et al. 1995; Glarborg et al. 2003; Pershing and Wendt 1977; Poinsoot and Veynante 2001; Rigby et al. 2001; Smoot 1993; Smoot 1997; Solomon et al. 1992; Stubington et al. 1997), and a complete review is beyond the current project. Reaction paths of fuel-N from different low-grade fuel combustion stages are described as follows.

2.2 Fuel-N conversion during low-grade fuel combustion

Low-grade fuel combustion process can be separated into two processes: devolatilization and oxidation (Chum and Overend 2001; Smoot 1993). Devolatilization is the process whereby mass evolves from the fuel by thermal decomposition to form gases and tars. The amount of volatiles formed is a function of the initial fuel structure, particle temperature, and the heating rate (Glarborg et al. 2003). Most work was focused on coal devolatilization (Solomon et al. 1992), and less is known about the phenomena of biomass and alternative fuels (Jenkins et al. 1998; Leppalahti and Koljonen 1995b). One main reason is coal has been the primary fuel used for power generation. Another reason is that the complex composition and structure of biomass and a shortage of a comprehensive compilation of biomass combustion behaviors (Diebold and Bridgwater 1997).

Coal devolatilization includes of two consecutive processes: primary and secondary devolatilization (Chen et al. 1992; Chen and Niksa 1992; Fletcher et al. 1992). During primary devolatilization, tar is composed of fragments vaporizing from the cleavage of weak aliphatic bonds in the solid fuel matrix, consisting of hundreds to thousands of organic species. CO₂, light aliphatic gases, and H₂O are released with the

breakage of the functional groups. Secondary devolatilization includes the decomposition of tar and the remaining solid. Additional gas species such as CH_4 , CO , and H_2 are released. The remaining aliphatic side-chains are released and ring condensation occurs in the solid matrix. For coal, this step occurs at temperatures above 1150 K and is strongly temperature and rank dependent (Li and Nelson 1996).

Once the volatiles are formed, the remaining solid is classified as char. Char mass is decreased by oxidation. Generally, devolatilization and char combustion are successive processes. However, they can be simultaneous processes depending on the reaction conditions and particle size (Veras et al. 1999). Compared to coal, biomass exhibit lower char yields and higher yields of both tar and gases due to their much higher volatile content (Leppalahti 1995).

During low-grade fuel combustion, the conversion of fuel-N to NO depends on the identity of the parent fuel nitrogen compound, the local combustion environment, and the initial fuel concentration (Smoot et al. 1998). This project is dedicated to the study of gas-phase reactions during pulverized fuel combustion with an emphasis on NO_x , thus only fuel-N fate in the volatiles is reviewed, including gas species, tar and soot.

The overall reaction sequence for fuel- NO_x is fairly well established (Glarborg et al. 2003): when particle combustion begins, fuel-N distributes between the volatiles and the solid char matrix. The distribution of nitrogen between char and volatiles, as well as the volatile nitrogen composition, depends mainly on fuel structure and temperature.

Figure 2.2 shows the difference in fuel- NO_x conversion among different categories of fuels, by depicting the conversion of fuel-N to NO , N_2O and HCN versus the nitrogen content of the fuels measured in the laboratory-scale combustor at an

operating temperature of 800°C and 10-kPa oxygen (Diebold and Bridgwater 1997). The fuels adopted in the analyses are classified into three types according to their behavior and nitrogen content: Low N-content (< 2% wt, daf) with high N-conversion (>30%) (I); Medium N-content (1-4% wt, daf) with medium N-conversion (> 20%) (II); High-nitrogen content (> 4% wt, daf) with low N-conversion (< 20%) (III).

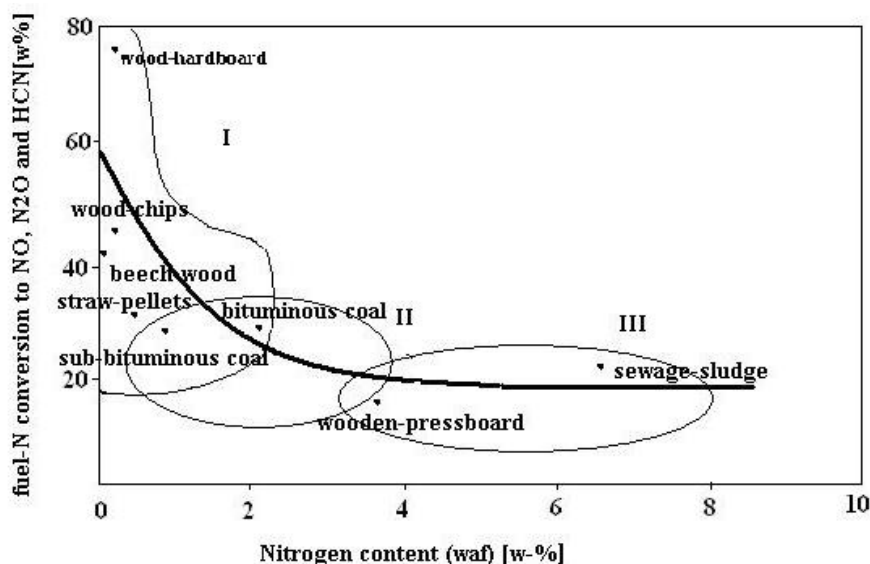


Figure 2.2 The conversion of fuel nitrogen versus nitrogen contents of different fuels, reproduced from Diebold et al. (Diebold and Bridgwater 1997)

Although some data from thermogravimetric-mass spectroscopy show no relationship between parent fuel nitrogen structure and nitrogen evolution (Smoot et al. 1998), an increasing number of investigations show that the forms of nitrogen in fuel provide clues to the fuel-N conversion routes during the initial stages of combustion (Aho et al. 1993). This relation between nitrogen functional groups (functionality) in fuels and NO_x precursors may indicate the conversion of fuel-N from the condensed phase to NO_x precursors in the primary zone of a coal burner (Glarborg et al. 2000).

Nitrogen occurs in coal principally as a heteroatom in aromatic rings (Nelson et al. 1992b). Modern analytical techniques (NMR, FTIR, XPS, etc.) indicate coal contains four major structures: aromatic clusters, aliphatic bridges and loops, side-chains, and oxygen groups. X-ray Photoelectron Spectroscopy (XPS) results indicate that nitrogen occurs in three forms in coal: pyrrolic, pyridinic, and quaternary. Almost all of the nitrogen (up to 100%) is located in pyrrolic and pyridinic nitrogen in high rank coals with pyridinic nitrogen up to 40% (Pels et al. 1995).

The nitrogen mass fraction in typical biomass is usually between 0.1 to 2% (wt, dry ash free basis) which is a much wider range than coal, and biomass has much more family members than that of coal, therefore the nitrogen functionality in biomass is expected to vary widely with fuel types (Jenkins et al. 1998).

Some insight into nitrogen functionalities in biomass comes from nitrogen behavior in the parent plants. In the nitrogen metabolism in higher plants (such as trees and high grasses), nitrate (NO_3^-) and ammonium (NH_4^+) are the major sources of nitrogen taken up by the roots. In the plant body, nitrate is converted to ammonia, which forms amino acids, amides and related compounds through a complex biochemical process. Amino acids are a source of protein that can be converted to amines, which are important components of bio-membranes (Marschner 1990). Essentially all nitrogen in living plants occurs in amine forms, that is, is bound with single bonds to neighboring carbon atoms. Therefore, one can expect at least two types of nitrogen functional groups in biomass: amine and amide.

Devolatilization accounts for the main part (> 90%) of nitrogen oxides during low-grade fuel combustion (Chen and Niksa 1992; Liang and Kozinski 2000; Winter et al.

1997; Winter et al. 1999b). The fraction of nitrogen released during coal devolatilization varies by fuel type, temperature, and the residence time (Baxter et al. 1996). It increases with decreasing coal rank (Bassilakis et al. 1993). There are two types of nitrogen release: aromatic compounds and light nitrogen species such as HCN and NH₃ (Chen et al. 1992; Chen and Niksa 1992; Smoot 1993). During primary devolatilization, most nitrogen is released in the form of aromatic compounds (Chen and Niksa 1992; Fletcher et al. 1992; Kelemen et al. 1998; Watt et al. 1996). The pyridinic compounds has a higher thermal stability than pyrrolic species, and the latter might be converted into pyridinic or quaternary compounds with increasing temperatures (Aho et al. 1993). Part of quaternary nitrogen may be formed as intermediates during the oxidation of the pyridinic nitrogen to NO_x (Nelson et al. 1992b). The quaternary nitrogen in lower rank coals transforms to pyridinic forms and remains in the coal char (Kelemen et al. 1995).

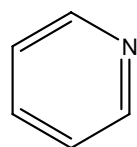
For low rank coals, nitrogen mainly evolves during the secondary devolatilization in the form of light-nitrogen species (HCN and NH₃) (Glarborg et al. 2003). The formation of NH₃ requires the presence of condensed phase carbonaceous materials rich in hydrogen. In the condensed phase, the thermally more stable N-containing structures may be hydrogenated slowly by the H radicals to NH₃. Because of the lack of donatable hydrogen atoms in these aromatic compounds, more HCN than NH₃ commonly evolves during pyrolysis of pyridinic and pyrrolic compounds (Aho et al. 1993). The stable C=N bonds probably also contribute to higher HCN concentrations.

Devolatilization of bituminous coals produces mainly HCN, while more NH₃ evolves from lower rank coals and biomass (Leppalahti 1995). Some experimental data from selected biomass pyrolysis experiments appear in Table 2.1. These are associated

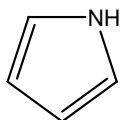
with the presence of quaternary nitrogen which is present in larger quantities in low rank coals (Zhang 2000). For biomass, the source of NH_3 is presumably direct cleavage of amino groups and amides. Figure 2.3 illustrates the basic molecular structures of amides and amines, compared with that of benzene, pyridine and pyrrole. The energy required for the conversion from C-N bonds in amine or amides to $\text{C}\equiv\text{N}$ bonds in HCN (about 580 kJ/mol) is much higher than that needed from amine or amide C-N bonds to form N-H bonds in ammonia (about 80 kJ/mol)(Ebbing and Wrighton 1987). This indicates that NH_3 rather than HCN could be the primary product in biomass devolatilization.

Table 2.1 Experiment data shows NH_3 concentrations are much higher than HCN in the pyrolysis of selected biomass fuels (Brink et al. 2001)

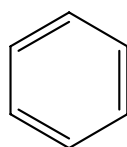
Fuel Tested	HCN	NH_3	
Wood and paper	25 – 45 mg/m^3	800 – 1000 mg/m^3	(Leppalahti et al. 1999)
Peat	520 – 930 ppm	3170 – 4600 ppm	(Leppalahti and Koljonen 1995a)
Peat and wood	5 – 30% (Wt)	70 – 95% (Wt)	(Coda Zabetta et al. 2000)
Black liquor	None	About 100% (Wt)	(Veras et al. 1999)



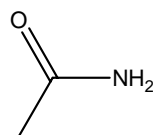
pyridine



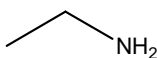
pyrrole



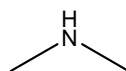
benzene



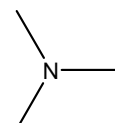
ethylamide



ethylamine



dimethylamine



trimethylamine

Figure 2.3 Molecular structures of pyridine, pyrrole, benzene, amide and amine

A large fraction of HCN and NH₃ may come from cracking reactions of the tar, and the remaining tar nitrogen may be incorporated into soot through structural rearrangements during devolatilization (Nelson et al. 1992a). However, there is very limited knowledge on the rates and products of this thermal degradation of the tar, partly because of its large number of different compounds and the dependence of the decomposition on both the parent fuel and the process conditions (Glarborg et al. 2003). Current knowledge of the tar chemistry comes from tar structural analyses from model compounds and experiments of tar pyrolysis and oxidation.

The tar nitrogen resides largely in similar structures as in the parent coal (Nelson et al. 1992a). At temperatures below 1100 K, thermal degradation of tar yields small amounts of light gas-phase nitrogen, possibly from the cleavage of the side-chains in the tar molecules. Under higher temperatures (1400 K), significant release of gaseous nitrogen species, mainly HCN, results from the rupture of the heterocyclic structures (Wojtowicz et al. 2000). The nitrogen release from tars of different coal types is very similar (Zhang 2000), which indicates that the reactivity of the tar-nitrogen functionalities during secondary devolatilization is rank independent. However, this may not be valid for biomass fuels, and differences have been reported for nitrogen reactivity of tars from coal, peat and bark (Leppalahti 1995).

The nitrogen content in the soot appears to be proportional to the nitrogen fraction in the parent coal (Rigby et al. 2001). Little is known about the fate of the soot-N. Since the coal soot nitrogen was shown high thermal stability (Perry et al. 2000), its fate is possibly analogous with that of char nitrogen, which is partly oxidized to NO (Glarborg et al. 2003).

Besides direct release from the solid matrix, NH_3 can be produced from hydrogenation of HCN on the surface of char, depending on heating rate and particle size (Baumann and Moller 1991). HCN is converted to NH_x at reaction times less than 1 s at 1 atm, and in a fuel-rich environment ($\text{SR} = 0.6\text{--}0.8$) (Chen and Ma 1996). With longer reaction time, NH_3 may become the main product in the reaction of lignite due to the catalytic effect of the lignite ash (Winter et al. 1999a).

The fuel-N transformation in the gas-phase was studied mostly with model compounds. It should be cautioned that the differences in experimental conditions and in transformation pathways make a detailed comparison of the data for different model compounds very difficult. Even pseudo first-order rate constants are difficult to compare because of the different experimental conditions (Glarborg et al. 2003).

Investigations of inert pyrolysis of several model nitrogen compounds including pyrrole and pyridine at temperatures in the range 1100–1400 K show that nitrogen present in these compounds is converted primarily to HCN (Terentis et al. 1992): at 1373 K, HCN accounts for 100% of the nitrogen from pyridine. It is noteworthy that the decomposition products of pyridinic and pyrrolic model compounds do not include NH_3 . However, if the model compound contains oxygen functional groups (hydroxyl, carboxyl or carbonyl groups), NH_3 may be formed during pyrolysis (Hamalainen et al. 1994).

Most work in the past on gas-phase fuel nitrogen conversion has focused on HCN and NH_3 . The oxidation chemistry of HCN has been studied under flame conditions across various types of facilities from shock tubes (Higashihara et al. 1983) to flow reactors (Glarborg and Miller 1994; Houser et al. 1988; Wargadalam et al. 2000). NH_3 has even more results for the high temperature ($>1400\text{K}$) chemistry (Coda Zabetta et al.

2000; Coda Zabetta and Kilpinen 2001b; Glarborg et al. 1998; Glarborg et al. 2000; Glarborg and Miller 1994; Kilpinen et al. 1999). In addition, a number of modeling studies and reviews of ammonia chemistry have been reported (Dean and Bozzelli 2000; Glarborg et al. 2003). Under fuel-lean conditions, both species are oxidized to NO with high conversions, since with high temperatures prevailing in flames the nitrogen atom in the light nitrogen species is sequentially stripped of the bound H and C atoms, ending up as NH, as shown in Figure 2.4. Even though the nitrogen species initially follow different oxidation paths, the steps that determine the selectivity towards NO and N₂ are possibly similar. All species feed into the amine radical pool (the dashed box in Figure 2.4), where the subsequent reactions of NH and N might only depend on the flame conditions, i.e. stoichiometry, temperature, total fixed nitrogen level, etc. Hydrogen cyanide is converted to NH in a sequence of reactions mainly involving CN and NCO, while ammonia is oxidized through NH₂. For this reason nitrogen volatiles partitioning is often of little importance for NO formation. However, the similarities between N-oxidation pathways of HCN and NH₃ break down at lower temperatures or under very fuel-rich conditions (Glarborg et al. 2003), where the reaction path NH₃ → NH₂ → N₂ (directly or via NNH) is promoted rather than the sequence NH₃ → NH₂ → NH → N (Skreiberg et al. 2004). Furthermore, alternative detailed pathways provide different routes to both N₂ and NO than appear in the simplified diagram of Figure 2.4.

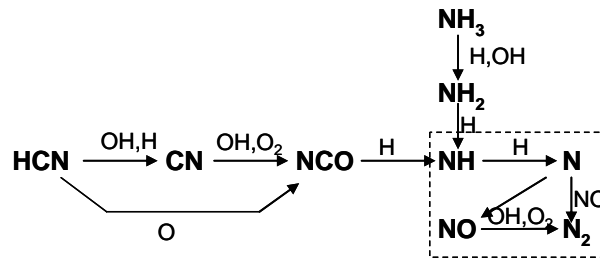


Figure 2.4 Reaction path diagram illustrating major steps in volatile-N conversion in flames for HCN and NH_3 at moderate fuel-N concentrations (Glarborg et al. 2003).

2.3 Experimental measurements and modeling results of swirling flows

During the development and commercialization of non-premixed swirling flow burners, many investigations have been carried out to clarify the phenomena in the near burner swirling region. However, even swirling cold-flow dynamics is not fully understood (German and Mahmud 2005). State-of-the-art technologies such as laser Doppler velocimetry (LDV) has been used to quantify the velocity profiles under both swirling cold flow and combustion conditions (Nazeer et al. 1999; Pollard et al. 2005; Solero et al. 2000). CFD simulations provide relevant evaluations of burner flows in a cost-effective manner.

Different turbulence models were adopted to investigate the swirling flow under cold flow conditions, including the well established Reynolds-averaged Navier–Stokes equation (RANS) models: the standard $k-\varepsilon$ (Kucukgokoglan et al. 2000), RNG $k-\varepsilon$ (Zhou et al. 2003) and the realizable $k-\varepsilon$ (Widmann et al. 1999) turbulence models.

As one of the key tools to predict and study combustion instabilities encountered in swirling flows, large eddy simulation (LES) has become a standard tool in analyzing turbulent combustion dynamics (Caraeni et al. 2000; Peters and Weber 1997). Predictions of a non-reacting, particle-laden, swirling flow in a coaxial-jet combustor show much more precise flow description with LES than with the RANS models (Apte et al. 2003), but for reasons of cost and complexity, the application of LES is limited to fairly simple geometries (Poinsot and Veynante 2001). As soon as real complex geometries of the facilities are considered, such as the flows between vanes of swirl-generators, these structured meshes must be replaced by unstructured grids, resulting in a tremendous increase in computing expenses.

Characterizing the complex interaction between swirling reverse flow, energy transport, and turbulent chemistry, swirling reacting flow is one of the most important and challenging areas in modern CFD (Frassoldati et al. 2005). In modeling reacting swirling flows, the main approach is to use different mathematical models to describe the flow dynamics and heat transfer, which can yield detailed information on velocity and temperature fields. But their predictions of chemical species concentrations are much less accurate, especially, species such as NO_x which are reacting on the same order of time scale as that of the mixing dynamics in highly turbulent flows (Faravelli et al. 2001). Furthermore, it is necessary to use a very refined numerical mesh for a good prediction in the near-burner region. This increases computational expense to predict NO_x in the gas-phase swirling combustion flows.

During solid fuel swirling flow combustion, the structure of the recirculation zones, which are critical for flame stabilization, are complex. Transient effects of

localized extinction and reignition processes on the structure of swirling flames depend on many subtle factors. However, in spite of these limitations, CFD models can still be used to predict temperature and velocity fields and it has been demonstrated that gas-phase CFD methods are useful tools for evaluating pulverized fuel swirling flow burner design (Coelho et al. 2001).

For solid fuel swirling flow combustions, comprehensive experiment data sets should contain information from both condensed and gas phases under different swirling conditions. These data sets include spatial temperature, velocity distribution from phases, major gas species (CO, CO₂, O₂, NO, important NO_x intermediates) profiles, size distribution, burnout and composition of particles, transmission, and heat flux.

Complete data sets can be obtained through laboratory- or pilot-scale facilities detailing different characteristic subprocesses of solid fuel reactions and interrelation of the fluid dynamics, reaction, and flame structure in the near-burner region (Widmann et al. 1999). Complete data sets are very limited for pulverized fuels (Ballester et al. 2005). A few examples of coal combustion experimental data can be found in the open literature (Abbas et al. 1994b; Schnell et al. 1993; Tree et al. 1998; Tree and Clark 2000).

A representative set involving pulverized coal in a swirl stabilized burner was available for analysis. The data was taken on the same facility to be used in this project (Pickett et al. 1999). The data set has been used for the validation of the commercial CFD models developed by ACERC, pulverized coal gasification and combustion-three dimensional (PCGC-3). (This reactor has been modified and upgraded for the present project, and a detailed description is provided in the experiment section.)

Pure Black Thunder coal tests with an overall stoichiometric ratio of 1.1 provide benchmark information for the reburning project. Three swirl intensity settings were selected, with preset swirl numbers of 0, 0.5, and 1.5, respectively. LDV was used to collect spatial velocity profiles. As plotted in Figure 2.5, the central jet with a zero swirl number transitions into an IRZ and a radially oriented jet with a swirl number of 0.5. When the swirl number increases to 1.5, the intensity of the reverse flow swirl is increased and helps stabilize the flame.

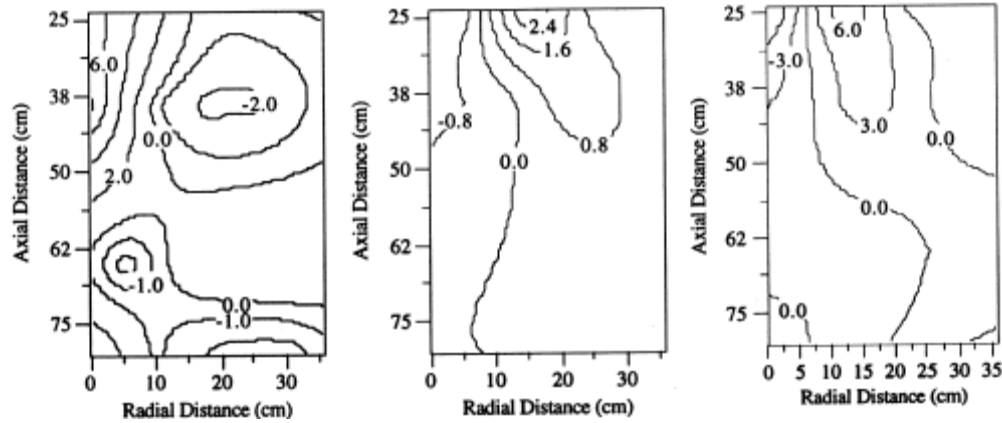


Figure 2.5 Mean axial velocity contours at three swirl settings: 0 (left), 0.5 (middle), and 1.5 (right) (Pickett et al. 1999).

Gas-phase temperatures were measured with a suction pyrometer. Figure 2.6 shows temperature contours. With the increase of swirl, the high-temperature core moves up and extends radially, indicating that the IRZ helps stabilize the flame and shorten the flame axially towards the inlet, accompanied with a radial extension of the flame front. The peak temperature drops because of a better mixing of air and fuel caused by the recirculating flows. At the highest swirling intensity ($S = 1.5$), the radial profiles are generally flat at an axial distance greater than 55 cm from the inlet, with a distinct

decrease in centerline temperature as distance from the inlet increases. The large temperature gradients near the walls were reported to be an artifact caused by the sampling system, drawing air from outside the reactor, and don't represent real temperatures.

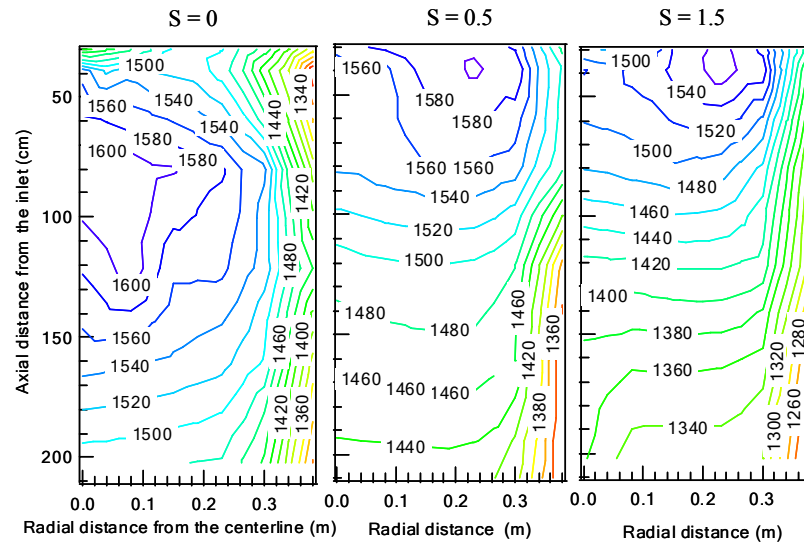


Figure 2.6 Temperature (K) contours with different swirl settings, adapted from (Tree et al. 1998).

Figure 2.7 presents CO₂ concentration contours that show a similar trend to that of gas temperature. High concentrations of CO₂, about 16% in these tests, indicate exhaust gas where reactions have completed. The particle samples collected from the 1.5 swirl number test show that the coal burnout reached 99% at axial distance greater than 80 cm.

The CO concentration profiles, plotted in Figure 2.8, demonstrate an interesting trend compared to those of the gas temperature with increasing swirl intensity. The high CO region, whose boundaries are 14 cm from the centerline and 70 cm from the inlet at zero swirl setting, expands to an axial distance of about 100 cm and radially across the

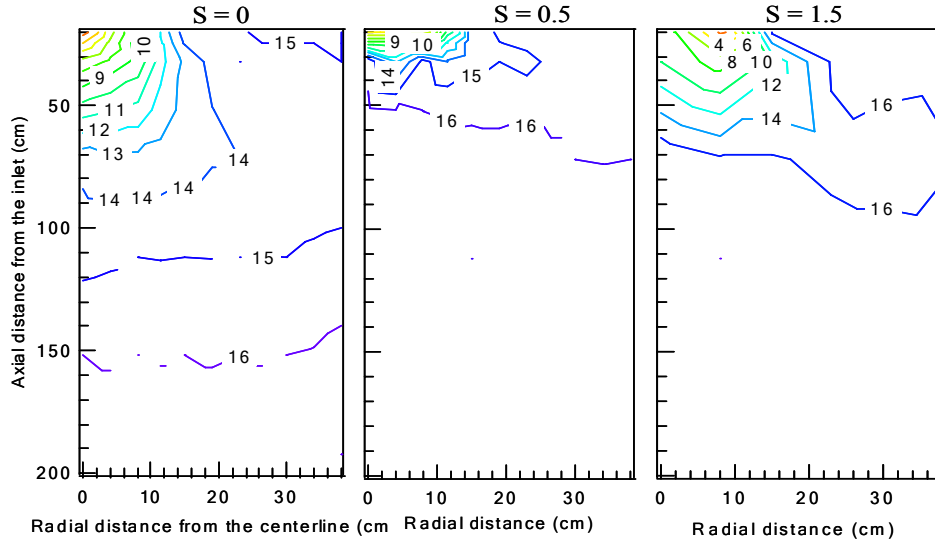


Figure 2.7 Contours of mean CO_2 mole concentration (%) (Tree 2002).

whole reactor. With even higher swirl intensity, this region shrinks axially to about 50 cm from the inlet, maintaining the radial extension across the whole reactor. The peak value drops with higher swirl during the 1.5 swirl test, indicating the diluting effect of the reverse turbulent flows on sampling. During the 1.5 swirl test, in the reactor top section, the near-wall region is characterized with both high CO and high CO_2 concentrations. This can be attributed to the possible existence of an ERZ in this high swirl intensity case, which brings mixtures having high CO concentrations into the exhaust gas.

O_2 concentration contours show some interesting aspects, as seen in Figure 2.9. The high O_2 concentration core shrinks toward the inlet from 0 to 0.5 swirl number, followed by an axial expansion during the 1.5 swirl number test. Contrary to the data from gas combustion mentioned earlier, an O_2 -deficient region was not found in the coal tests. Combined with the CO contours, it is obvious that there is a high O_2 and high CO region located in the IRZ during all the three tests, indicating this location must experience fluctuations of oxidizing and reducing conditions.

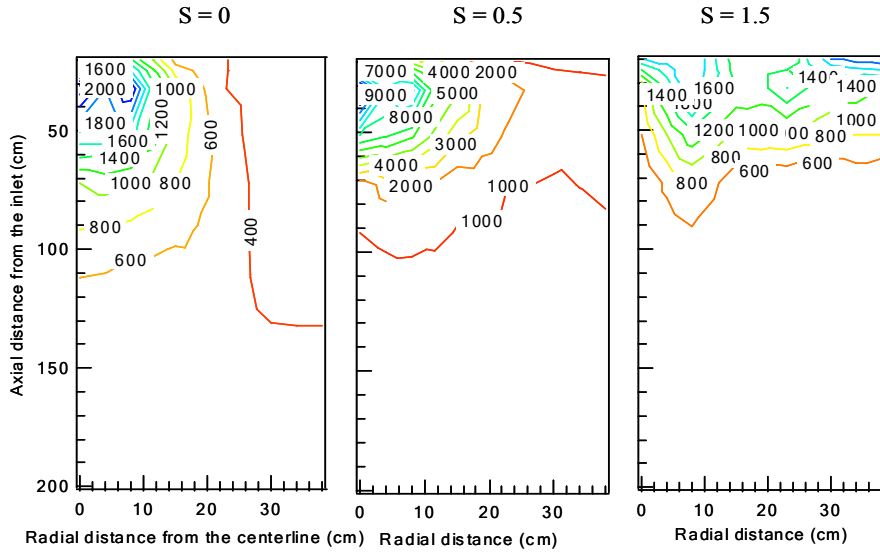


Figure 2.8 Contours of mean CO mole concentrations (ppm) under different swirl settings, adapted from (Tree 2002)

Also in Figure 2.10, NO profiles show a monotonic trend along the centerline during the 0 to 0.5 swirl number tests. In the top centerline region, low concentrations of NO appear. In the exhaust gas, NO has a concentration ranging from 650 to 700 ppm. In the 1.5 swirl number test, at axial distances greater than 90 cm, NO concentration monotonically decreases from 650 ppm to about 450 ppm.

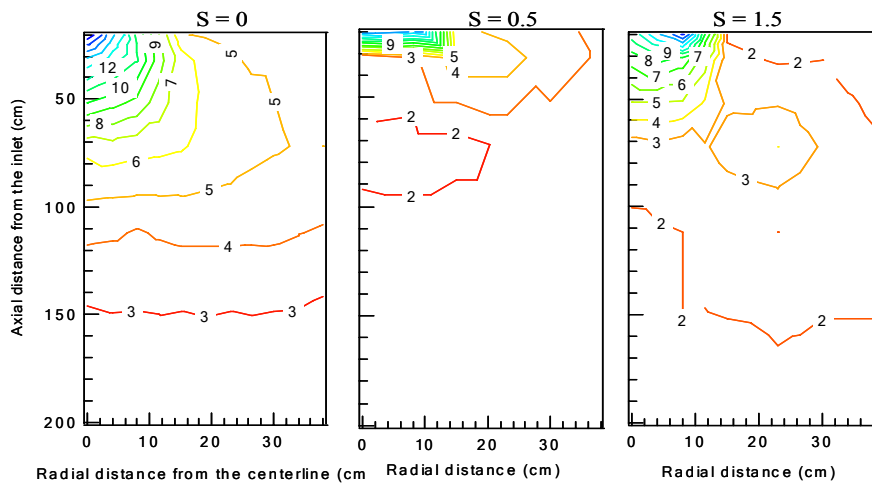


Figure 2.9 Contours of mean O₂ mole concentration (%) under different swirl settings, adapted from (Tree 2002).

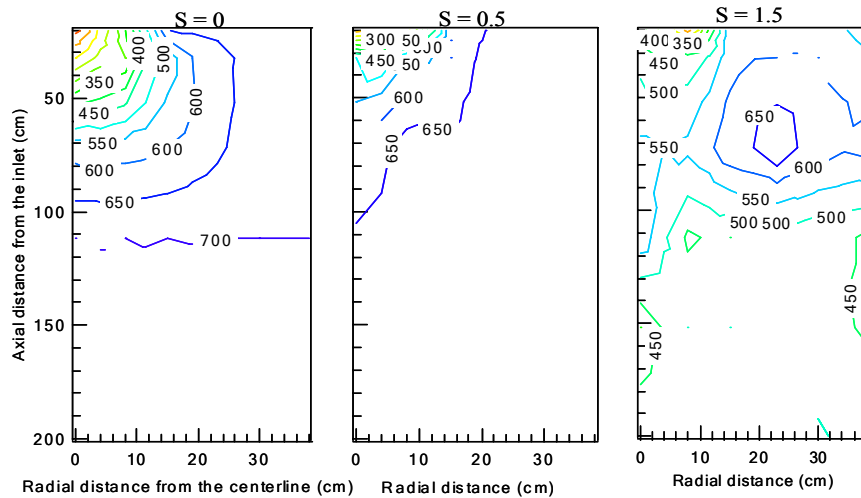


Figure 2.10 Contours of mean NO mole concentrations (ppm) under different swirl settings, adapted from (Tree 2002).

Combined with the coal data sets, experimental data of the biomass flames in the near-burner region could provide important benchmark for possible fuel-switching strategies. Although much of the information available for coal could be transferable to biomass combustion (Williams et al. 2001), there are still areas lacking information. Especially, detailed experimental biomass flame data under swirling flows are very rare, the only available set in the open literature is the research by Ballester et al (Ballester et al. 2005), involving three kinds of pure pulverized fuels, including a lignite, a bituminous coal, and oak sawdust. These single fuel tests have a swirl number of 1.02, with an excess air of 9% for lignite and bituminous coal tests and 14% for the sawdust test. Spatial distribution data of four species, O_2 , CO, NO, and unburned hydrocarbon (UHB), were reported from all three tests.

For a better distribution of fuel particles, the injector was composed of a central hole surrounded by smaller peripheral orifices. With highly swirling secondary air, a

rapid mixing zone was generated, and the burner could be seen as a combination of a single central jet and an annular jet, characterized with both high penetration and high mixing. Figure 2.11 shows the result that during all the tests, in addition to the IRZ close to the inlet, there exists a secondary reacting zone downstream. In this region, fuel particles penetrating the IRZ ignite and gradually deplete O_2 , resulting in a fuel-rich core. This was confirmed by both O_2 profiles from the tests. Outside the core, particles were centrifuged to different degrees depending on their location and particle size, resulting in a conical shape flame, which was confirmed by visual observations.

The fact that oak sawdust has a much higher volatile content (78.84 % wt) than that of the bituminous coal (23.8 % wt) caused a significant increase of gaseous fuel in the near inlet region, and this was postulated as the primary reason the flame appeared much more luminous and had a larger diameter near the quarl, indicating a significant increase of gaseous fuel in this region. The existence of the two combustion stages is more evident for biomass than the bituminous coal, as indicated by the O_2 and NO_x profiles indicated in Figure 2.12 and Figure 2.13. This is possibly caused by the longer devolatilization time and a higher inertia and penetration length of the biomass particles during combustion.

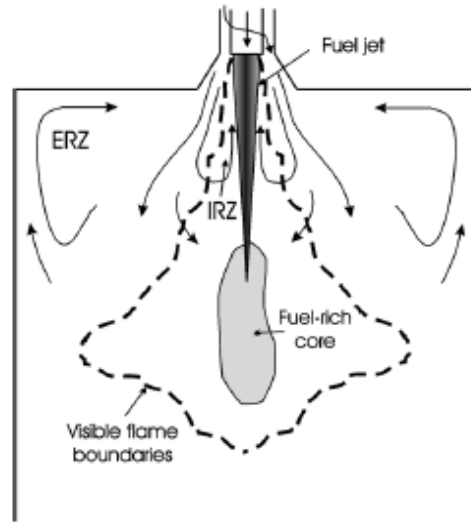


Figure 2.11 Qualitative description of the flames (Ballester et al. 2005).

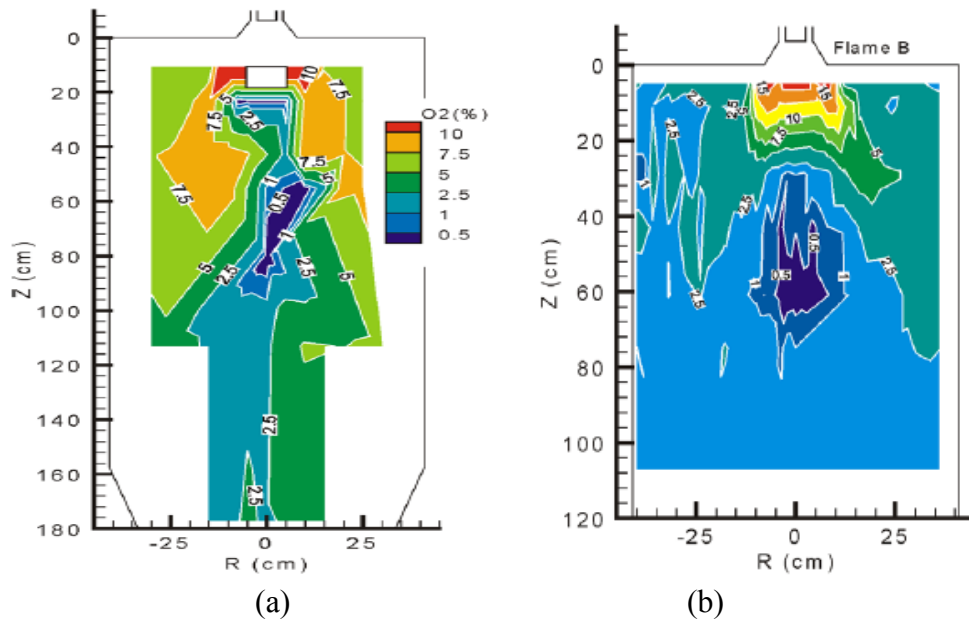


Figure 2.12 Contours of O_2 molar concentrations (%) from oak sawdust flame (a) and the bituminous flame (b) (Ballester et al. 2005).

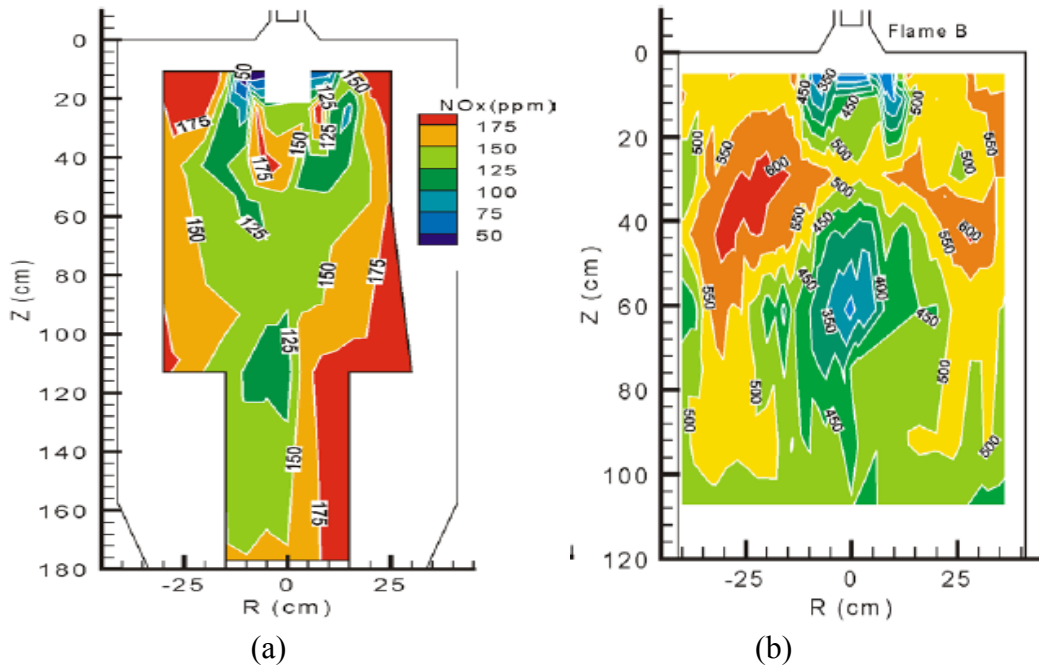


Figure 2.13 Contours of NO_x molar concentrations (ppm, vol, db) from oak sawdust flame (a) and the bituminous flame (b) (Ballester et al. 2005).

2.4 Summary

In this chapter, the operating characteristics of a generic swirling flow burner were introduced. Research on the modeling and experiments to verify these characteristics were briefly reviewed. For a better understanding of nitrogen oxides formation study in the near-burner region, fuel-N evolution during low-grade fuel combustion was summarized. Over the past thirty years, the phenomenological models describing the formation of NO_x in coal combustion have been relatively well developed compared with that of biomass. The understanding of coal-NO_x formation mechanisms contributes to a comparatively well-developed gas-phase mechanism that is broadly applicable. Analogous to the fact that HCN is the major NO_x precursors from the unsaturated aromatic nitrogen compounds during coal combustion, it is assumed that NH₃ appears as dominant NO_x intermediate during biomass devolatilization. However, the

relative amounts of nitrogen-containing intermediates and stable compounds produced from a mixture of coal and biomass is far from being well developed. The experimental data of the fate of biomass fuel-N in swirling flow burners are scarce. There is little information on the impact of swirl on the near-burner light nitrogen gas species profiles during low-grade fuel combustions. A more comprehensive literature review related to this dissertation appears in Appendix A.

Chapter 3 Research Objective

NO_x formation/depletion during pulverized low-grade fuel combustion in commercial burners is a highly complex process that is incompletely understood. Experimental data during biomass-coal cofiring are virtually non-existent.

The primary goal of the current research is to provide a set of accurate species data with supporting velocity and temperature predictions documenting flame structure and NO_x formation during biomass firing, coal firing and cofiring tests in a swirling flow burner. Specifically, two-dimensional (axisymmetric) spatial profiles (maps) of NO, HCN, NH₃, O₂, CO, and CO₂ concentrations are measured in a pilot-scale, cylindrical, down-fired combustor operated with a swirl-stabilized burner, complemented with cold-flow velocity data and CFD predictions. Also, a solid-fuel combustion model simulates the non-premixed swirling flow burner and provides reasonable velocity and temperature predictions, validated by the available LDV and suction pyrometer data, respectively, from the previous CPR advanced reburning project.

This data analysis reveals the differences and similarities in the coal vs. biomass flames, which are caused by fuel properties. At the same time, NO emission during the tests provides a basis for future industrial application. Different detailed NO_x formation/depletion mechanisms provide kinetic evidence of the differences between coal and biomass during swirling flow combustion.

Finally, this project determines experimentally and explains theoretically the impacts of fuel-N forms on light nitrogen gases generation under conditions and fuel types representative of commercial coal-biomass cofiring burner operations, providing data reflecting the near-burner behavior in cofiring tests.

Chapter 4 Descriptions of Experiments

This section describes the swirling-flow, pulverized fuel burner, the gas sampling systems, fuel characterization, feed systems, and operation of the burner system.

4.1. The Burner Flow Reactor (BFR)

The available BYU coal-combustion facilities represented a great resource for this work, but the facilities lacked the capability for biomass firing at the beginning the current project. Substantial alterations have been completed in three areas:

- a) Refurbished the Burner Flow Reactor (BFR). The investigator modified the existing pilot-scale, pulverized-fuel reactor to simulate biomass/coal cofiring. The refurbishment of the BFR included recasting the refractory walls and window plugs, and recalibration of the swirl-generator, primary air, secondary air, and natural gas (used for warming-up) flow rates. The inner refractory liner of the BFR was rebuilt at the beginning of this project, and a detailed procedure description is provided in Appendix B. The electrical heaters in the walls, which had rarely if ever been used and which represented a significant safety hazard, were removed prior to recasting.
- b) Designed and constructed a biomass fuel-feeding and gas sampling systems. All combustion tests were completed with coal and biomass directly mixed from two separate

and driven by constant-speed auger-motors. Each feeder has independent control, enabling different fuel ratios. The coal feeder has a much finer control than the biomass feeder. Both feeders have calibrated feed rates under different settings, as recorded in Appendix C. Separate feeders mitigated the significant problems associated with mixing two dissimilar fuels (different particle sizes, densities, particle shapes, etc.) together and attempting to feed them through a single feeder. A new gas-sampling system was built, including a specially made sampling probe and two gas analyzers with advanced technologies.

Distinguished by its swirling flow, the BFR is an axisymmetric, 0.2 MW, pulverized fuel, down-fired reactor. Fuel and primary air (about 10% of the total air mass feeding during operation) flow through the primary inlet, and secondary air (about 90% of the total air mass) passes through a swirl-generator before entering the reactor. The down-fired design minimizes ash deposition on the burner and simplifies the feeding operation. As depicted in Figure 4.1 (Tree and Clark 2000), each of six sections of the BFR is 40 cm high with an internal diameter of 75 cm, minimizing the wall confinement on the flame. With a total internal height of 240 cm, the BFR somewhat simulates the operation of one burner in a full-size boiler. The inside walls are lined with a refractory layer.

Each section has four vertical access windows located 90° from each other and each is filled with refractory plugs when access to the flame is not desired. The optical windows extend nearly the full height of the section for fine resolution of flame in the axial direction, and these windows provide ample accessibility for use of non-

intrusive/intrusive diagnostic probes, visual observation, and photography (Tree and Clark 2000).

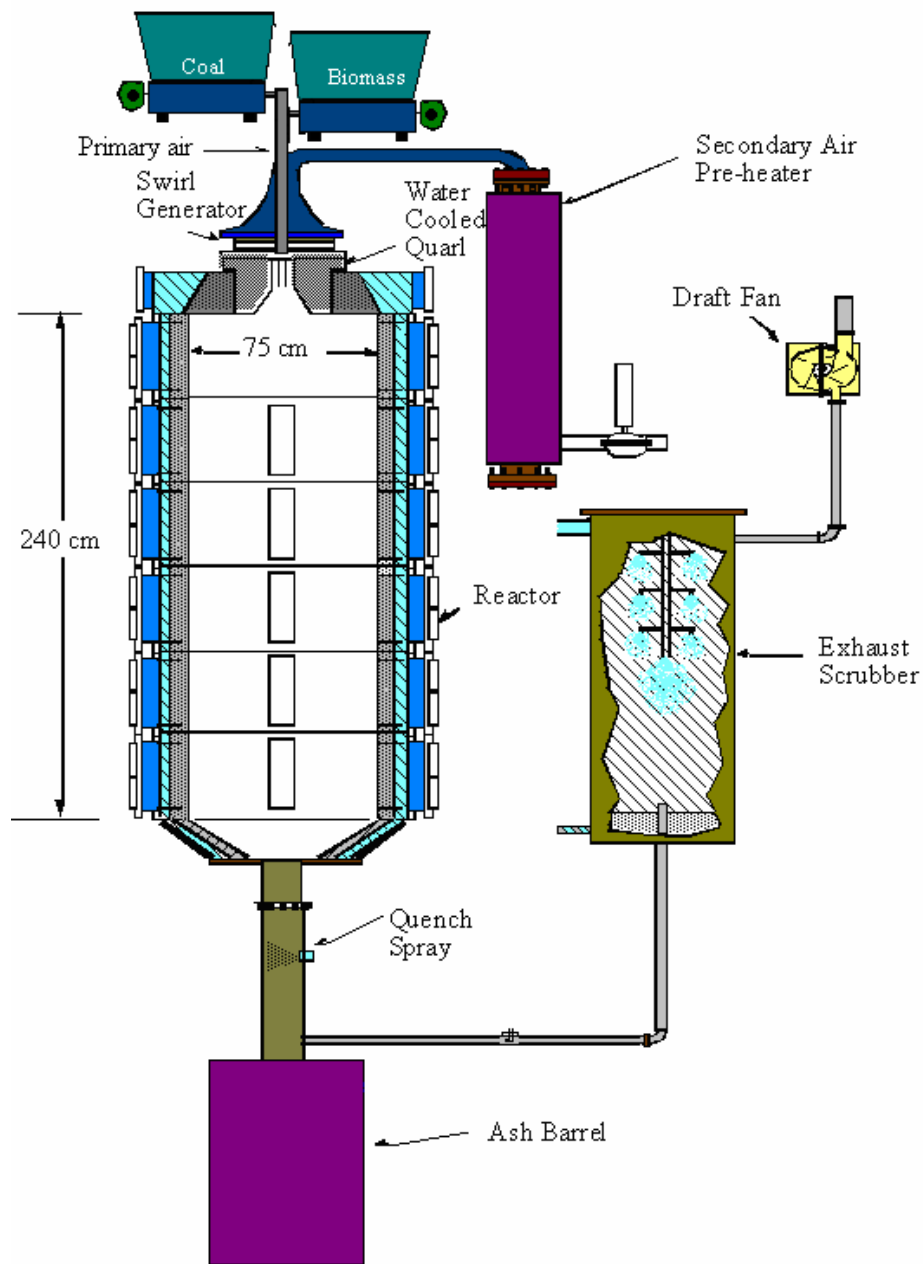


Figure 4.1 BFR system and the combustion chamber.

One of the basic intentions of building the BFR was to measure NO_x profiles with respect to controllable operating conditions. The BFR has demonstrated this capability in the combustion of natural gas and pulverized coal, and the data have helped develop comprehensive, multidimensional combustion models (Eaton et al. 1999).

An adjustable block swirl generator is used to produce swirling flows, and the geometry is detailed in the previous work (Eatough 1991). The swirl-generator in the BFR includes two interlocking plates with eight pairs of identical triangular blocks. The burner cross section and one of the plates is illustrated in Figure 4.2. With the lower plate mounted to the quarl of reactor, the top plate is free to rotate, generating different angles between the triangle vanes of the two plates. The secondary air passes between the two plates, producing a nearly constant tangential velocity profile across the inlet duct. The design represents a generic industrial gas burner, and allows for continuous variation in inlet swirl number and is capable of handling ambient and preheated combustion air.

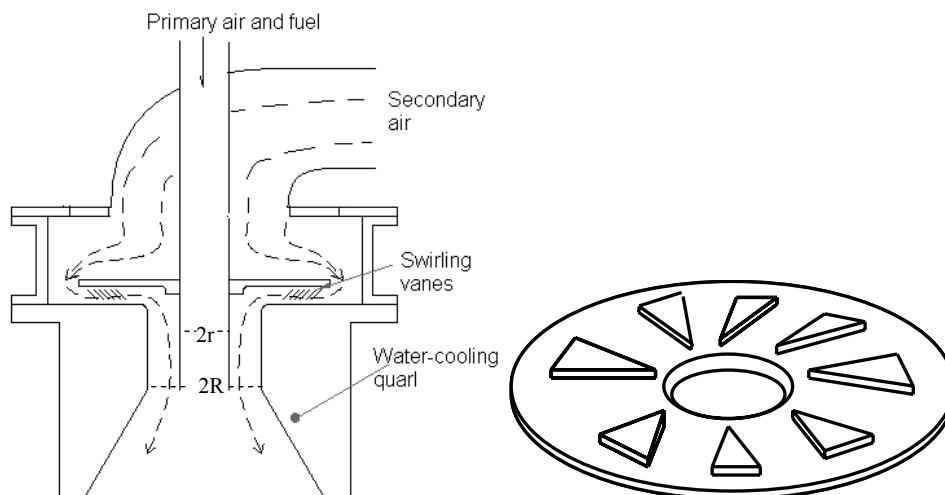


Figure 4.2 The burner cross section (top) and the lower plate of the swirl-generator (bottom): the center hole is the fluid path, and the triangles are the vanes.

The swirl is quantified by swirl number (Beer and Chigier 1972), which is defined as the ratio of the axial flux of tangential momentum to the axial flux of axial momentum:

$$S = \frac{\int_r^R w \rho u 2\pi r dr}{R(\int_r^R (P - P_\infty) 2\pi r dr + \int_r^R u \rho u 2\pi r dr)} \quad 4.1$$

where u , w , and P are the axial and tangential components of the velocity and the static pressure, respectively, in any cross section of the jet, r and R are the outside radius of the primary air pipe and duct radius of the secondary air path right after the swirl generator, respectively, and ρ is the local gas density. The axial flux of the axial momentum includes a turbulent stress term and a pressure term representing the axial thrust. The pressure term is usually ignored, since pressure changes are difficult to measure.

The swirl-generator was calibrated following the methods in the previous project (Eatough 1991). During the swirl-generator calibration, the tangential momentum flux was calculated from the torque required to straighten the flow through a honeycomb calibrator, the axial flux was calculated based on the hot-wire anemometer measurements, with the pressure term neglected.

The previous control system for the BFR was replaced with a new, LabVIEW™-based system. The pressures in the primary and secondary air were measured with pressure transducers. Pressure transducer and thermocouple signals were recorded directly into the computer. The primary air flow rate was calibrated with a commercial gas flowmeter. The secondary air was calibrated with help from external sources (FlowserveCorp. 2002). The results are listed in Appendix D. During this project, several

equations were used to relate gas and orifice properties to mass flow rates. The most theoretically justified of these are as follows. Assuming adiabatic and isentropic flow through the orifice, the mass flow relates to the up- and down-stream pressures as follows

$$\dot{m} = \frac{C_D A_T p_0}{(RT_0)^{1/2}} \left\{ \frac{2k}{k-1} \left(\frac{p}{p_0} \right)^{2/k} \left[1 - \left(\frac{p}{p_0} \right)^{(k-1)/k} \right] \right\}^{1/2} \quad 4.2$$

where \dot{m} is the mass flow rate (kg/hr), p_0 is the stagnation (approximately the upstream) pressure, p is the static pressure in the orifice, C_D is an empirically determined discharge coefficient, A_T is the area of the orifice, and k is the ratio of heat capacities (about 1.4 for air), T_0 is the temperature, and R is the standard gas constant.

However, if the velocity in the orifice is sonic, the static pressure in the orifice is independent of the downstream pressure and becomes a constant fraction of the upstream pressure, making the portion of the above equation in curly brackets a constant that depends only on k . In this case, the equation becomes the well-established choked flow equation, given by

$$\dot{m} = \frac{C_D A_T p_0}{\sqrt{RT_0}} k^{\frac{1}{2}} \left(\frac{2}{k+1} \right)^{\frac{k+1}{2(k-1)}} \quad 4.3$$

In the current project, an orifice diameter of 0.25 in was used, the same as the calibrated value in the previous reburning project (Tree et al. 1998) and consistent with the label on the orifice. Based on this orifice diameter, the above equation fits calibrated flow rate data with a discharge coefficient of 1.203 and a correlation coefficient of 0.998. (In the latest project by another Ph. D. candidate, Brad Damstedt, the diameter was remeasured to be 0.276 in, and the choked flow equation accurately predicts the

secondary air actual flow rates with a correlation coefficient of 1.000 and a discharge coefficient of 0.995.)

4.2. Gas sampling apparatus

4.2.1. Sampling probe

Among the gas species measured in this project, HCN and especially NH_3 are highly water soluble at room temperature. Water contents of combustion gases are quite high (up to 0.2, mole fraction) and water condensation occurs whenever local probe temperatures are below the gas dew point, which occurs commonly with water-cooled probes. Such condensed water has the potential of scrubbing ammonia and hydrogen cyanide from the sampled gases, biasing the measured results. Therefore, a nitrogen-quenched, water-cooled gas-sampling probe was designed and constructed for the current project. A detailed illustration is provided in Appendix E. N_2 was chosen as the quenching gas because it is chemically inert, relatively inexpensive, and meets safety considerations. Nitrogen flowmeters record the dilution effect on the gas samples.

The sampling probe collects the gas mixture. Upon entering the probe, controllable N_2 dilution gas quenched the sample, preventing any further reaction in the probe and lowering the sample dew point to less than ambient temperature. The sample reached room temperature, cooled by the water shell of the probe. At the sample end of the probe, an optical port in the particle collection cup provided confirmation that steam did not condense. If water appeared in the cups, sampling was terminated and adjustments were made such as changing the cooling water flow rate or increasing the N_2 flow rate. The N_2 dilution is used only during HCN and NH_3 measurements.

4.2.2. Cyclone, particle filter, and heated gas path lines

Particles are inevitably aspirated with the gas mixtures during sampling, and they potentially block the sampling path. Furthermore, particles in the gas analyzers may cause noticeable error. Therefore, a cyclone was designed and built into the sampling system. A schematic is provided in Appendix F. As depicted by Figure 4.3, the gas samples and particles passing through the probe reach a cyclone, where larger particles are separated from the main gas flow and drop into the ash collected below the cyclone. The sample is further cleaned by a fine particle filter downstream.

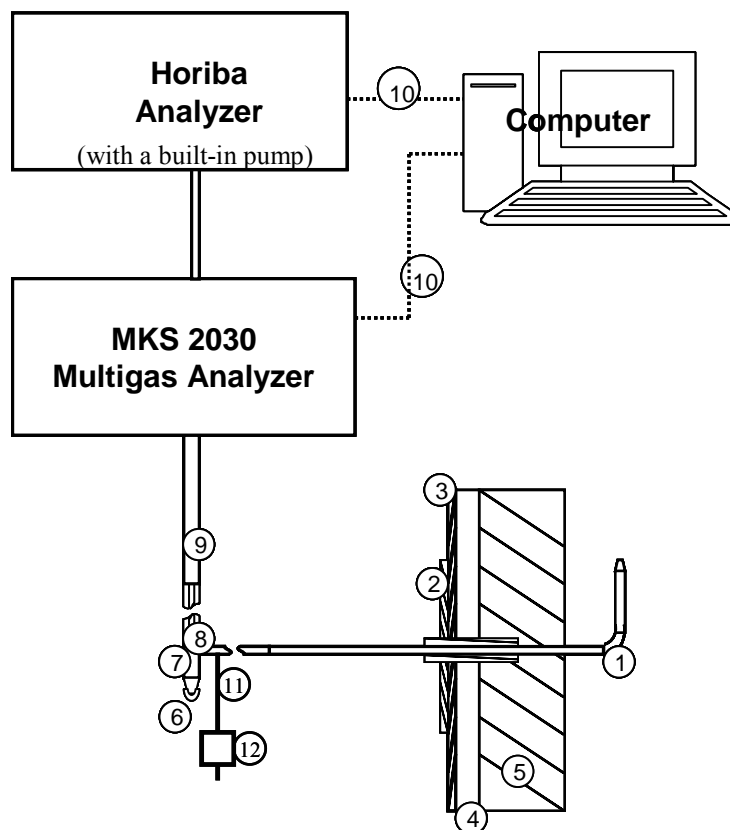
A heated gas path design was included in the sampling system. The line comprises stainless steel tubing wrapped with heating tapes, maintaining a temperature above 100 °C, preventing condensation of steam. Along the heated line, the particle-free gas samples enter the MKS gas analyzer, whose gas inlet has a constant temperature of 150 °C through the sampling process.

4.2.3. Gas analyzers

Two separate gas analyzers provide species concentration data for these measurements, since a single device capable of quantifying all the species studied is not available.

A Horiba PG-250 portable gas analyzer acquired for this project has the capability of continuously quantifying the following gas concentrations (dry measurements) with manufacturer-indicated ranges and precision indicated in parentheses: NO (0 – 25/50/100/250/500/1000/2500 ppm, ±0.01 ppm), O₂ (0 – 5/10/25 vol %, ±0.01%), CO (0

– 200/500/1000/2000/5000 ppm, ± 0.01 ppm), CO₂ (0 – 5/10/20 vol%, $\pm 0.01\%$), and SO₂ (0 – 200/500/1000/3000 ppm, ± 0.01 ppm) (Horiba Inc. 2000). This analyzer has a built-in



1. Gas sampling probe 2. Probe mount 3. The reactor outside wall
 4. Water jacket 5. Refractory liner 6. Particle holder 7. Cyclone
 8. Particle filters 9. The heated sampling line 10. Signal line
 11. N₂ line 12. N₂ rotometer

Figure 4.3 Description of the gas sampling system with the BFR.

pump with a constant operating output (0.4 L/min), acting as the drawing of the gas samples. The interference is illustrated in Table 4.1. Non-dispersive infrared detectors (NDIR) measure CO, CO₂, and SO₂ concentrations. Chemiluminescence provides NO

data. A galvanic cell oxygen analyzer provides oxygen concentrations. The analyzer includes particle filtration systems and minimal sample conditioning. The analyzer's repeatability is $\pm 0.5\%$ of full scale except when CO and NO are above 1000 and 100 ppm, respectively, where repeatability for these gases is $\pm 1\%$ of full scale. Zero drift is no more than $\pm 1\%$ of full scale per day except for the SO₂ analyzer, where zero drift is $\pm 2\%$ of full scale per day. Span drift performs similarly. Linearity is within $\pm 2\%$ of full scale. Minimum detectable limits are no more than 0.5% of full scale. The analyzer is typically calibrated before each experiment using NIST-traceable, certified gases.

The second analyzer is a Multigas 2030 FTIR-spectroscopy based online system equipped with a liquid-nitrogen cooled mercury-cadmium-telluride (MCT) detector with a 0.25 mm x 0.25 mm element. It has a working resolution of 0.5 cm⁻¹, a path length of 5.11 m, and normally averages are between 8 and 64 scans per analysis. The Multigas Analyzer uses the MG2000 quantitative analysis software, which allows users to collect and simultaneously analyze sample streams containing complex gas mixtures.

The Multigas 2030 FTIR online gas analyzer reportedly is capable of ppm to ppb level sensitivity for more than 30 gas species including HCN and NH₃ in a variety of applications including combustion emissions monitoring. The inlet heat of the analyzer can maintain the sample at a constant temperature of 150 °C, and it can perform analysis in gas streams that contain up to 30% water. The zero-calibration is performed with pure nitrogen gas before every use.

Gas samples inside the BFR were collected with the sampling probe. During measurements of HCN and NH₃, the diluting N₂ flow rate through the sampling probe is set at 0.3 L/min to prevent steam from condensing. The gas samples passed through the

Table 4.1 Interference table of the Horiba gas analyzer (HoribaInc. 2000)

Measured component	Interference gas						
	H ₂ O (5 °C saturation)	NO 1000 ppm	C ₃ H ₈ 1000 ppm	SO ₂ 1000 ppm	CO ₂ 20%	CO 5000 ppm	CH ₄ 100 ppm
NO	± 2.0%FS	_____	± 2.0%FS	± 2.0%FS	±	±	_____
SO ₂	± 2.0%FS	± 2.0%FS	± 2.0%FS ¹	_____	± 2.0%FS	± 2.0%FS	± 5.0%FS
CO (≤ 200 ppm)	± 2.0%FS	± 2.0%FS	± 2.0%FS	± 2.0%FS	± 2.0%FS	_____	_____
CO (> 200ppm)	± 1.0%FS	± 2.0%FS	± 1.0%FS	± 1.0%FS	± 1.0%FS	_____	_____
CO ₂	± 2.0%FS	± 2.0%FS	± 2.0%FS	± 2.0%FS	_____	± 2.0%FS	_____
O ₂	± 2.0%FS	± 2.0%FS	± 2.0%FS ²	± 2.0%FS	± 2.0%FS	± 2.0%FS ³	_____

1. The concentration of the interference gas for SO₂ component is C₃H₈ at 100 ppm
2. The concentration of the interference gas for O₂ component is C₃H₈ at 100 ppm
3. The concentration of the interference gas for O₂ component is CO at 15%

cyclone, particle filter, and heated line and arrived at MKS Multigas analyzer, where all gas species except oxygen were quantified. The outflow then entered the Horiba analyzer, where O₂, SO₂, CO₂, CO, and NO were measured.

4.3. Fuel selection and feeding system

In this research, species composition maps (NO, NO₂, HCN, NH₃, O₂, CO, CO₂, and SO₂) were measured as a function of position during a series of coal, biomass, and coal-biomass cofiring tests. The two coals and two biomass fuels selected for these tests represent widely differing examples of each fuel. Nevertheless they represent a small fraction of the potential number of fuel combinations.

Straw is a widely available herbaceous biomass fuel that has relatively high nitrogen content compared with many wood-derived fuels. As a representative

commercial energy a crop, straw has been widely used in the EU, especially Denmark. For example, the annual production of straw is estimated at about 4.2 million tons, and about 3 million tons are cofired.

Currently, about 50% of the US annual wood waste (around 39 million tons) is available as fuel (DOE 2003). Clean wood biomass has proved to be the best candidate for energy production by cofiring in current PC facilities. Sawdust is a common ligneous biomass fuel with low nitrogen content.

In terms of ash management properties during combustion, straw typically exhibits high ash, high alkali, high chlorine, and high silica contents relative to wood. However, wood has high calcium concentrations (as percent of ash). These two fuels cover the range of both fuel types (herbaceous and ligneous) and nitrogen contents likely to be encountered in commercial application.

Two typical commercial coals in the United States, Blind Canyon and Pittsburgh #8, were selected for the current cofiring research. Blind Canyon represents a typical low-sulfur, low-moisture, subbituminous to bituminous coal used principally in the western US. Pittsburgh #8 represents a high-sulfur, low-moisture, high-energy content, low-oxygen, bituminous coal in common use in the Eastern and Midwestern US. These coals span most fuel properties ranges among coals commonly used in US and international power plants.

Proximate and ultimate analysis data for the fuels appear in Table 4.2. Coal and biomass analysis was performed with a LECO CHNS-932 elemental analyzer and oxygen content was obtained by difference. All fuels were prepared (milled and size classified) prior to the tests. One consequence is that all contained less moisture when analyzed than

would be typical in commercial operations. Both biomass fuels were prepared and shipped from Denmark by research collaborators.

Table 4.2 The physical properties of the fuels used in the current project.

	Straw	Sawdust	Blind Canyon	Pittsburg #8
Ash	7.52	0.39	11.42	9.10
Moisture	5.87	5.46	3.06	1.65
<i>Ultimate analysis (wt %, daf)</i>				
Carbon	44.4	48.9	70.3	83.2
Hydrogen	5.72	6.18	5.46	5.32
Sulfur	0.12	0.11	0.54	2.89
Nitrogen	0.91	0.35	1.54	1.64
Oxygen (difference)	48.9	44.5	22.2	6.95
Heating value (MJ/kg, daf)	15.9	18.0	27.8	31.2
Average particle size (μm)	475	345	70	70

Table 4.3 reports the proportional feed rate for nine tests using combinations of the four fuels. The high biomass to coal mass ratio, 70:30, represents the upper limit of common commercial biomass cofiring fractions. Measured fuel and air feed rate parameters appear in Table 4.4. The initial feed rates were measured at stand-by state, i.e. without firing any fuel or primary air flow but by metering fuel from the feeder into a weigh cell. The actual feed rate occasionally deviates from these settings for many reasons. The feed rates listed in the table were calculated from a carbon balance based on measured CO, and CO₂ concentrations (on a dry basis) in the exhaust of the reactor rather than the calibrated feeder results as the former is a more accurate measure of feed rate. Unlike the solid fuel feed rates, the air flows have a robust and accurate flow rates, as was verified through the preliminary natural gas combustion tests.

Table 4.3 Experiment layout for the tests with different fuels and their mass ratios.

Test ID	S	70S30BC	50S50BC	BC	SD	70SD30BC	70SD30P	70S30P	P
Straw	1	0.7	0.5					0.7	
Sawdust					1	0.7	0.7		
Blind		0.3	0.5	1		0.3			
Canyon									
Pittsburg							0.3	0.3	1
#8									

Table 4.4 The set-up feed rate of fuel and air flow rates under the test conditions.

Test ID	Biomass feed rate (kg/hr)	Coal feed rate (kg/hr)	Primary air feed rate (kg/hr)	Secondary air feed rate (kg/hr)	Ratio of primary to secondary feed rates	Equivalence ratio
S	20.74		15	150	0.100	0.64
70S30BC	14.7	6.55	8	145	0.055	0.89
50S50BC	10	10	8	153	0.052	0.90
BC		12.3	11	140	0.079	0.77
SD	19.7		7.3	115	0.063	0.90
70SD30BC	15.6	6.55	15	150	0.100	0.90
70SD30P	15.6	6.47	15	135	0.111	0.92
70S30P	14.7	6.47	15	135	0.111	0.93
P		12	15.4	115	0.134	0.92

4.4. Combustion experiment and data collection description

The BFR warms up using a natural gas flame, with an overall equivalence ratio of 0.9 for about four hours before switching to the solid fuels. The reactor is fully heated, when the target peak wall temperature reaches 1400 K, which is located in the reactor top section, about 10 cm below the origin plane (the plane where the lower end of the quartz meets the main body of the reactor). The wall temperature decreases at a rate of approximately 80 K per section, with the wall temperature in the bottom section about 1000 K.

The operating pressure of the BFR can be adjusted by a gate valve in the exhaust line, controlling the suction by the exhaust fan directly from the atmosphere. A pressure gauge connected to the inside of the reactor monitors the chamber pressure. During warm-up, the reactor operates at negative pressure, meaning the gauge pressure showed a negative value between 0 to -0.5 in H₂O, and any leak is into rather than out of the reactor. During gas sampling, the reactor pressure is positive, ranging from 0.25 to 0.75 in H₂O, minimizing the impact of the air leakage into the reactor on the samples.

A lot of operating experience with coal combustion operations in the BFR has accumulated from former projects. Biomass feeding in the BFR is new in this project and several issues are summarized as follows:

1. The biomass feeder can achieve a maximum feed rate of about 25 kg/hr for straw, and 22 kg/hr for sawdust. In cofiring tests, the biomass feed rate dictated the matching coal feed rates; that is, biomass feed rate is the limiting variable for overall firing rate.
2. Because of difference in fuel physical characteristics (size, shape, density, etc.), sawdust is much more difficult to feed than straw. The feeder calibration indicated that consistent feed rates require that the fuel in the feed hoppers must be maintained above a certain threshold (about 2/3 full). This requires frequent fuel addition into hoppers and careful adjustment of the feeder control.
3. The biomass feed rate is much more easily impacted than that of coal by the reactor chamber positive pressure, which may prevent biomass from being fed smoothly during sampling. This problem could be solved by proper set-up of primary air feed rate and a careful control of the reactor chamber pressure.

In addition to the temperature measured with thermocouples inside the walls of each section of the BFR, the gas species concentrations in the bottom reactor provided criteria for steady-state operation and overall stoichiometric ratio. The reactor was operating under overall fuel-lean conditions. For a certain equivalence ratio, the expected O_2 and CO_2 concentration were calculated assuming complete combustion. For example, in Blind Canyon combustion tests with an equivalence ratio around 0.77, the concentration of CO in the bottom section should be minimal, usually less than 50 ppm, O_2 should be about 6%, and CO_2 should be about 12%. The exhaust gas species monitoring, especially CO, O_2 , and CO_2 , were routinely checked for consistency with the fuel flow rate. If a relative error of greater than 10% was observed between the expected and measured value of these products, data acquisition was suspended until the problem was found and solved.

All the species data in this document represent constant wall temperature conditions and a reasonably constant exhaust O_2 reading, both of which were consistent among similar tests on different days.

The gas sampling began after the reactor reached steady state, with stable wall temperatures and exit gas species concentrations. With the current gas sampling set-up, the Horiba PG-250 gas analyzer and the MKS Multigas 2030 analyzer have different response time with respect to each gas species. For the Horiba gas analyzer, the CO reading changes in less than 1 min after the probe is positioned, and requires another 2 min before the final steady value is reached. The resultant emission value was determined by the mathematical average recorded after a visual inspection demonstrated steady-state. The total time for each species reading to reach the relatively steady state is called the

response time. A detailed description of the response time of each species with the two analyzers appears in Table 4.5.

Table 4.5 The response time of both analyzers under the testing conditions (unit: minute).

	Horiba PG-250	MKS Multigas 2030
CO	3	1
CO ₂	4	1
SO ₂	5	1
NO	4	1
O ₂	4	N/A
NH ₃	N/A	1
HCN	N/A	1

The lines in Figure 4.4 show the axial positions in the BFR used with the current sampling probe. Based on the choice of data collection points in the former project (Tree and Clark 2000), the large concentration gradients of the major gas species were limited to 15 cm around the axis in the top two sections. So, in this region, sampling points were selected at 2.5 cm radial positions, which are close to the diameter of the probe. Intervals of 5 cm were selected outside this region. The inlet line (zero line) is defined as the plane at the exit of the quarl. At least two sample sets from above this line (negative axial distance) appear in each of the maps. Note this reference frame is below that used in previous research with the same facility which defined the exit of the primary air tube as the zero line.

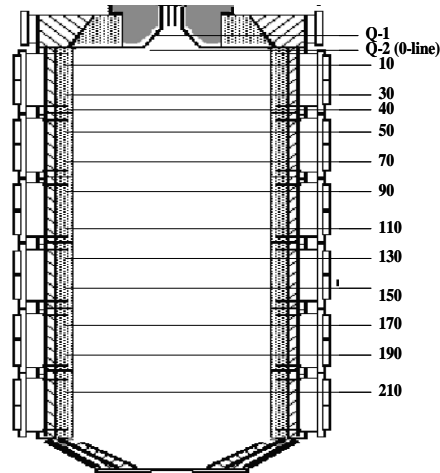


Figure 4.4 The lines represent the measurement locations at different axial distance (cm) from the inlet, where the reactor body meets the cooling water quarl is defined as the zero line.

4.5. Safety issues

Safety represents an overriding consideration in each of the tasks of this project and is routinely reviewed as part of the work. However, several major issues have impacted this project that warrant separate discussion.

The BFR originally included electrical heating elements provided to control wall temperature profiles. This feature of the reactor was responsible for its original name of the controlled profile reactor, or CPR. The wiring of these heaters resulted in high-current taps for the heaters exposed on the exterior of the reactor with flexible wire mesh guards installed to help prevent accidental contact with the wiring. The hazards associated with these relatively exposed wire taps represented unacceptably high risks to both people and equipment in that most of them could easily be pushed onto the conductors, there was provision to prevent water leaks, coal dust, or other potential conductors from shorting the wire taps to the combustor, and there were no in-line ground fault circuit interrupters installed. This main function of these heaters was to

minimize the temperature drop in the axial direction at normal firing rates and to extend the reactor capability to lower firing rates and long residence time. Wall temperatures do slowly decline when firing rates in the combustor are low. The heaters and their wire taps and leads have since been removed, together with the transformers, SCRs and circuits that support them.

There were no hazardous gas (toxic or combustible gas) sensors located in the building (or in any lab of which we were aware) at the time this project began. The potential for generation of hazardous gases during operation is fairly high and this situation was deemed unacceptable. Sensors for the major hazardous gases (CO, HCN, NH₃, SO₂, NO, and combustible gases) now monitor the laboratory. Despite rebuilding the reactor ceramic walls and attempting to prevent any gases from leaking into the test bay by both making an overall airtight reactor (as nearly as possible) and by operating under only slightly positive pressure, we cannot operate the facility in reducing mode over sustained periods of time without CO escaping into the test bay. We have therefore abandoned the intention of operating in overall reducing mode and positive pressure. One unanticipated observation is that the sensors in neighboring reactor bays commonly detect more CO than the one in the bay containing the BFR when operating in reducing mode.

A formal standard operating procedure (SOP) that identifies the purpose of the lab, the people who use it and formal requirements for safety training, the hazards and their mitigation, and the procedures used in starting up the BFR and shutting it down has been through several drafts and is awaiting institutional review. While aspects of this SOP have existed in less formal forms to date, our intention is to formalize the SOP,

obtain institutional review and approval of its contents, and use it to train and document safety aspects of the BFR in the future. When completed, the document will add potentially significant training and documentation requirements for the BFR and its personnel.

There remain a fairly large and dynamic set of safety issues with which we deal on a continuous basis associated with the reactor. Physical Facilities, Risk Management, and the college safety officers are involved in all of these discussions, most of which need not be documented here except to note that all personnel associated with the BFR are expected to maintain safety and environmental protection as the highest priorities for BFR operation, with priorities that exceed those of the research objectives.

4.6. Summary

The pilot-scale, swirl-stabilized burner flow reactor (BFR) was refurbished and upgraded into a facility capable of cofiring biomass with coal that include all of the complexity of commercial systems. This facility provides an aerodynamic and thermal environment representative of the near-burner region of a commercial combustor.

Seven gas species, CO, CO₂, O₂, SO₂, NO, HCN, and NH₃ are measured to enhance the understanding of biomass combustion performance in the near-burner region. A new intrusive sampling system was built, including an N₂-queched probe, a Horiba 250 portable gas analyzer, and a MKS 2300 Multigas analyzer. Combustion tests included nine separate fuels or fuel blends. Spatial profiles of major species from biomass cofiring provide detailed indications of flame structure and dynamics. All the tests were operated under overall fuel-lean conditions with a swirl number of 1.0.

Chapter 5 Computational Fluid Dynamics (CFD) Calculations

This project uses both experimental and modeled velocity fields. The experimental data include original cold-flow data from this project and both cold- and reacting-flow data collected previously in the same reactor.

In the current project, the predicted cold-flow velocity profiles agree with the measured cold-flow profiles, even in the reverse flow regions of the reactor. This level of agreement is attributable to details of the model parameters, structure, and technique introduced in this project. The predicted reacting flow velocity fields agree less well with the measurements, especially near the reactor centerline. While the predictions also contain many uncertainties, they provide a much more flexible tool with respect to reacting temperature and velocity profiles. This section describes the modeling strategy and verification and provides a critical comparison of both original and literature data relative to the model predictions. Gas species profiles are the major subject of this document and are discussed in a separate chapter.

5.1 Modeling purpose and strategy description

In a pilot-scale reactor dominated by turbulence such as the BFR, it is difficult to make accurate point-measurements of fire-side temperature and velocity. In former projects conducted in this reactor, temperature profiles were obtained with a suction pyrometer, and the velocities were obtained with laser Doppler velocimetry (LDV).

While suitable for temperature measurements in laminar, uniform reacting flows (Albrecht et al. 2003), the suction pyrometer technique unavoidably involves an averaging effect, especially in turbulent flows, and adds difficulty in determining the temperature at the measurement point.

The LDV is a non-intrusive, optical measurement technique for the determination of fluid velocity components with high temporal and spatial resolution. As micron-sized liquid or solid particles entrained in a fluid pass through an interference pattern created by the intersection of two laser beams, the scattered light received from the particles fluctuates in intensity. The frequency of this fluctuation determines the component of particle velocity which lies in the plane of the two laser beams and is perpendicular to their bisector.

The swirl-stabilized, low-grade fuel near-burner region is accompanied by high temperature gradients, and in tests burning biomass, the particle sizes are too large for LDV systems (Tree 2002). Therefore, CFD was used to predict the flow pattern and temperature profiles in the BFR. As one of the most widely used CFD tools in both industry and academia, FLUENTTM provides state-of-the-art codes capable of predicting flows involving complex geometries. Its user-friendly interface and high flexibility made FLUENTTM the modeling tool of choice in the current research.

Based on the configuration of the BFR, a non-premixed combustion simulation with a simple turbulence model was adopted. This method should meet the need for reasonable temperature and velocity predictions, which supplement the explanation of the experimental data collected. Because of the complex nature of low-grade fuel devolatilization and oxidation in a turbulent swirling flow, a series of simplified methods

were adopted in the turbulent chemistry for the non-premixed model in FLUENTTM. These simplifications are described detailed in Appendix G. The prediction of major species, including CO₂, O₂, and CO, should at least qualitatively fit the experimental data. As for the highly simplified fuel-NO_x model in the CFD code, the predictions of NO_x and its intermediates are hoped at most to reflect qualitatively the profiles of the experimental data.

In swirling flow burners, the inlet velocity profiles strongly influence flow field features. In this project, a swirl number of 1.0 was selected, and at these conditions limited historical velocity data exist from either cold flow (300 K) or low-grade fuel flames exists. However, historical data sets from a swirl number of 1.5 provide a good benchmark. The strategy adopted here is to develop a three dimensional (3-D) model capable of predicting flows under multiple swirl number settings. The solutions under 1.5 swirl setting are compared to the historical cold flow LDV data and hot-wire anemometer measurements. After validation of the 3-D model, a two dimensional (2-D) combustion model was constructed to predict hot flows, with the corresponding 3-D predictions at the entrance as the inlet conditions.

Verification of this modeling strategy was carried out by comparing predictions with the LDV data and the suction pyrometer temperature measurements with a 1.5 swirl number. Another nine 3-D simulations with the vane angle corresponding to a 1.0 swirl number were carried out, with the same air feeding set-up as that in the nine tests (Table 4.4). The results at the exit of the swirl-generator were adopted as boundary conditions for the nine 2-D axisymmetric combustion simulations, which were to predict reacting flow velocity and temperature profiles.

5.2 Modeling of the swirl-generator under cold-flow conditions

Because of its robustness, calculation economy, and reasonable accuracy for a wide range of turbulent flows, a standard $k - \varepsilon$ turbulence model was adopted to calculate the dynamics of the gas phase in the 3-D simulations.

A non-uniform unstructured mesh composed of 200,000 cells describes the geometry and flow domain of one eighth of the BFR. (The swirl-generator comprises eight pairs of identical vanes, as mentioned earlier, making a 1/8 model appropriate for the simulation.) The swirl-generator vane angle is 8° has a swirl number setting of 1.0 and 12° for a swirl number of 1.5. An illustration of the whole reactor, the modeled volume and the swirl-generator is given as Figure 5.1. Refined discretization was adopted in the flow region around the swirl-generator vanes, providing high resolution for the complexity of the geometry. Dense grids are also selected downstream through the water-cooled quarl to account for the changes of cross-sectional area. In the BFR chamber, numerical grids formed a structured mesh with hexahedral elements. The grids are plotted in Figure 5.2.

The steady-state simulations used the QUICK method, a second-order calculation scheme. The algorithms PRESTO and SIMPLEC were used to interpolate pressure and coupled pressure and velocity, respectively. Simulations of cold flow in the BFR with a 1.5 swirl number were compared with the available LDV data, for a primary air feed rate of 15.6 kg/hr and a secondary air feed rate of 175 kg/hr. Simulation results and experimental data for these conditions at different axial distances are plotted in Figure 5.3.

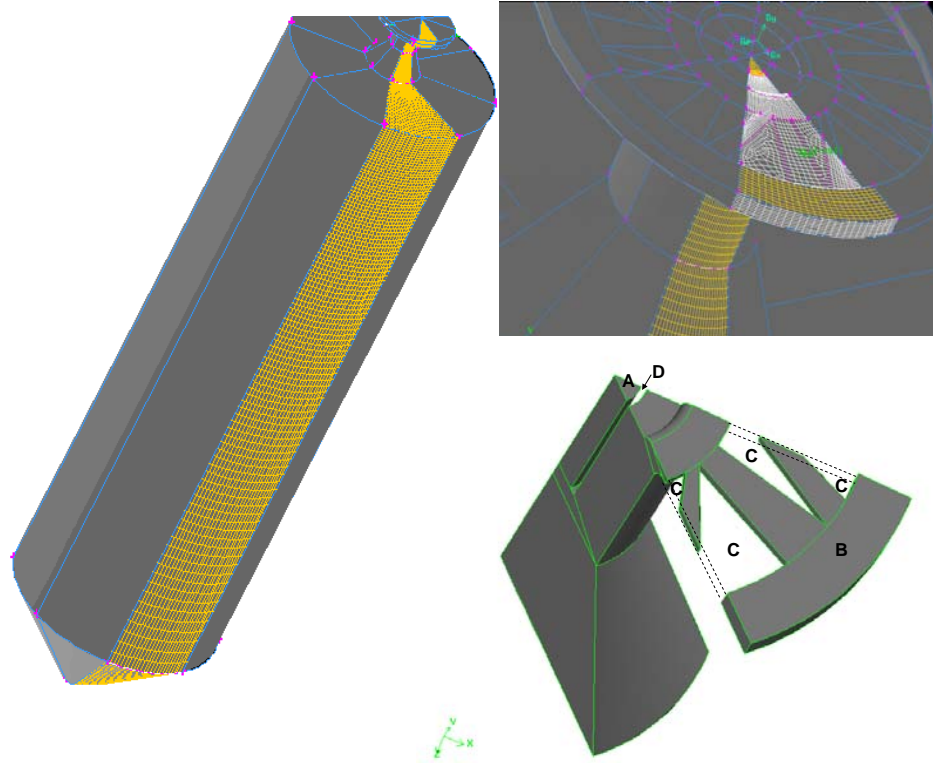


Figure 5.1 General description of continuous volume during the cold flow modeling: left: the whole reactor of the BFR, with the modeled reactor volume of 1/8 highlighted; right top: a general view of the swirl-generator and the modeled part; right bottom: modeled volume of the swirl-generator, primary air path line and cooling water quarl. A. Primary air/fuel inlet; B. Secondary air inlet; C. vanes of the swirl-generator; D. Wall of primary air pipe.

Generally, the predictions from the simple turbulence model (standard $k - \varepsilon$) follow the LDV data trends and are quantitatively accurate predictions for cold flow conditions in many regions. At 5 mm below the primary air pipe, still within the cooling water quarl, good agreement between data and predictions occurs. This is possibly because the confinement of the flow by the relatively small volume of the quarl helps maintain an axisymmetry of the stream. Further downstream, after complete expansion of

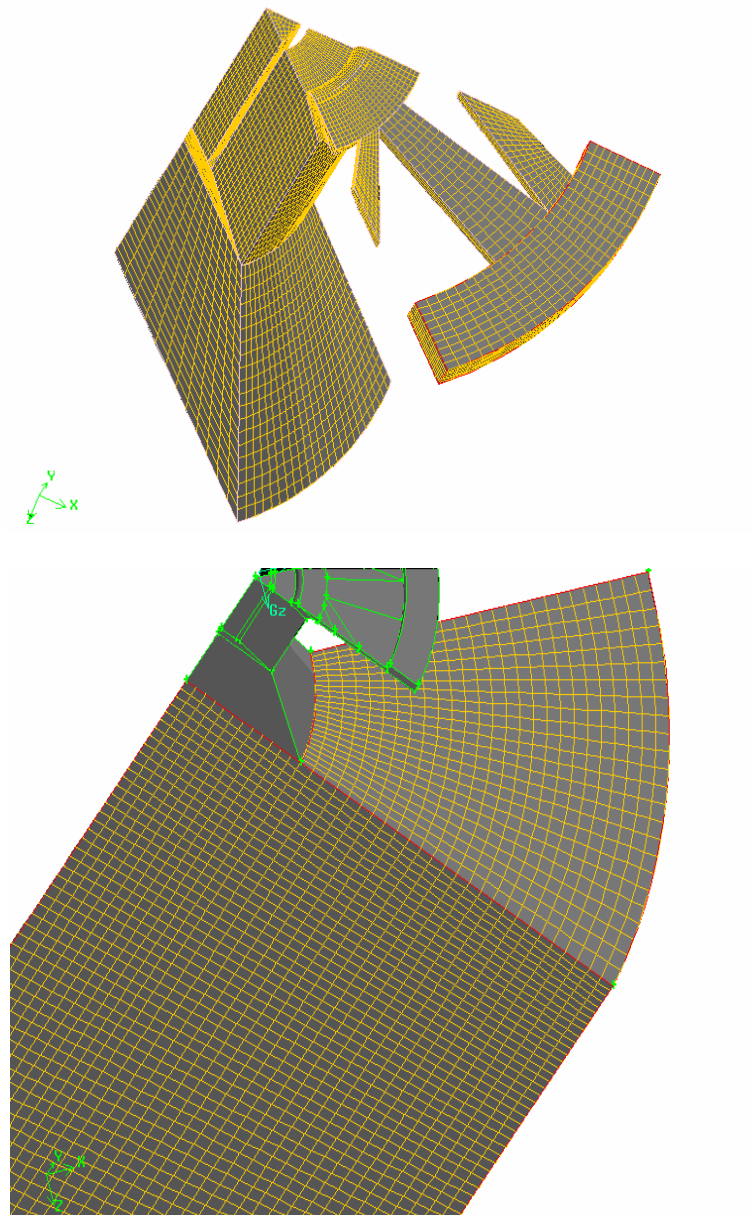


Figure 5.2 Grid set-up in the 3-D CFD calculation. Top: swirl-generator and cooling water quarl; bottom: BFR body.

the reactor cross-section, which is called reactor body zone (RBZ), the flow is fully developed with negligible impact of the wall confinement in the central region.

Radial and tangential velocities of axisymmetric flows must be zero at the centerline. The nonzero tangential velocities observed in the experimental data indicate the flow axis does not always correspond to the geometric axis. The disagreement indicates the flow complexity, even for cold air flow in the swirl burner. These data show that there is no assurance that nominally axisymmetric geometries and boundary conditions produce axisymmetric flows after swirling flow is fully developed in the RBZ. However, predictions will always produce such symmetry in the absence of any asymmetric boundaries or inlet conditions. In the RBZ (240 mm) under cold flow conditions, there is a reverse flow region (with the axial velocity less than zero) close to the centerline. A large gradient in axial velocity exists within 10 cm of the centerline while the axial velocity profile is flat near the reactor interior wall.

Hot-wire anemometer data collected provide additional velocity validation near the inlet. Axial velocity data from both sides of the reactor centerline provide additional measures of data consistency and a measure of the correspondence between reactor and aerodynamic centerlines. The axial velocity data at 15 cm below the origin plane with comparison to the CFD predictions appear in Figure 5.4. The positive velocity direction is towards the outlet. The model quantitatively predicts the axial velocity profiles in the swirling flow region under cold-flow conditions.

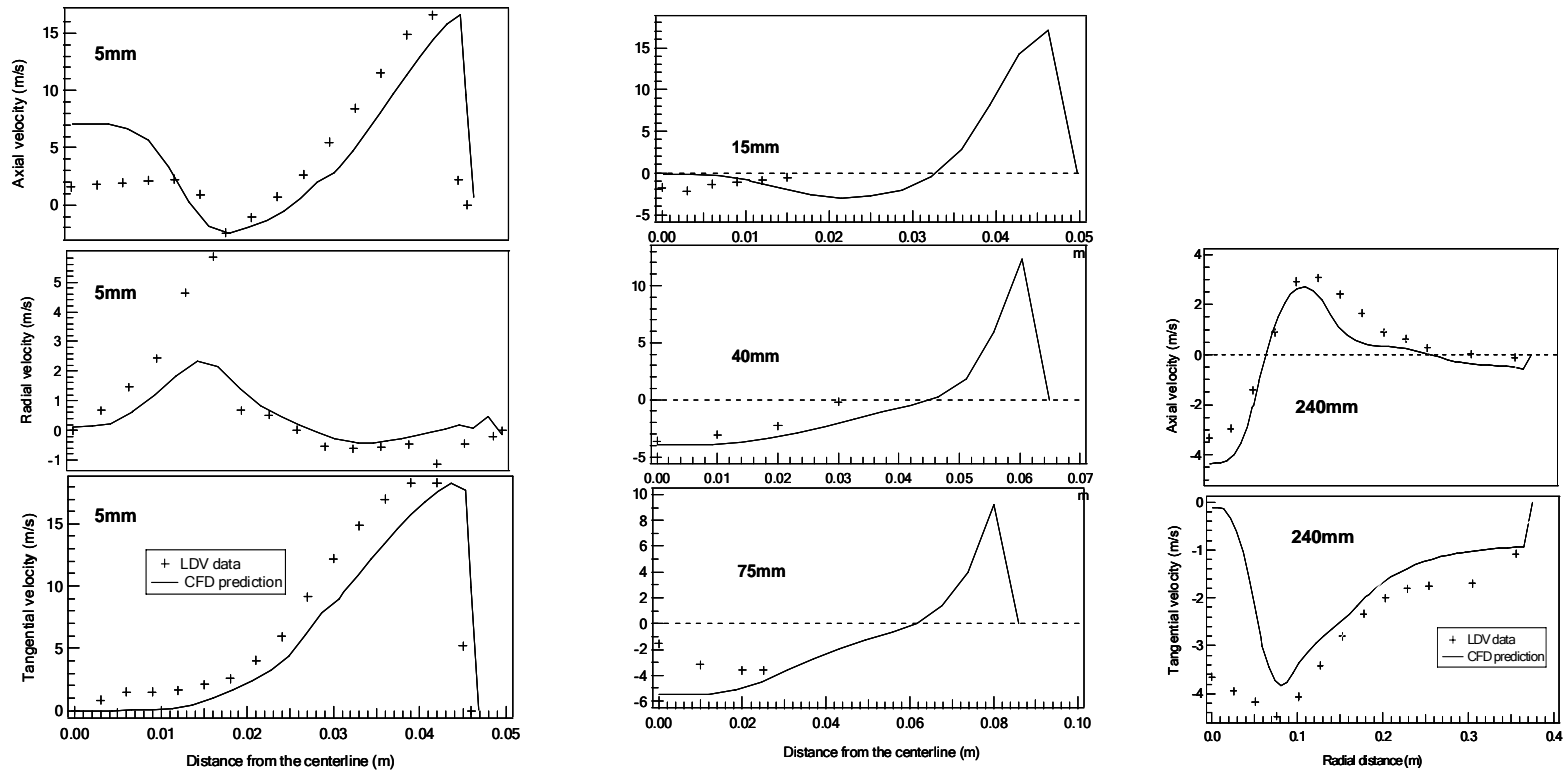


Figure 5.3 Comparison of the 3-D CFD predictions and the available cold flow LDV data (Pickett et al. 1999) at different axial distances from the end of the primary pipe, operating conditions: a primary air feed rate of 15.6 kg/hr and a secondary feed rate of 175 kg/hr, swirl number = 1.5.

Generally, accounting for the geometric complexity of the swirl-generator, the 3-D model developed here reasonably describes flow field information as measured in cold flow tests. With a swirl number of 1.5, in the inlet region, it accurately describes the flow since the geometry of the facility confines the complex flow within a small region, helping to preserve the symmetry. For tests with a swirl number of 1.0, the 3-D models with respective vane angle at air feeding set-up are presumably able to provide reliable inlet velocity information for simulations of the nine tests.

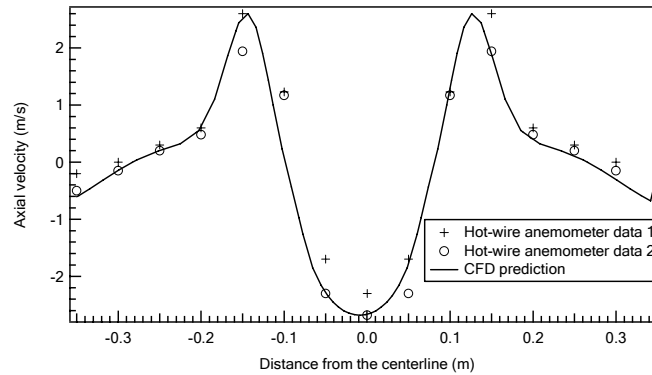


Figure 5.4 Comparison of the hot-wire anemometer data with 3-D CFD predictions 15 cm below the zero plane.

5.3 Combustion modeling description

The combustion modeling involves simulation of a continuous gas-phase flow field and its interactions with the discrete-phase particles traveling through the gas. The particles devolatilize, creating a source of fuel for reaction in the gas phase. The gas flow is described by the time-averaged Eulerian equations of global mass, momentum, energy, and species balances. The discrete-phase (particle-phase) equations are formulated in a Lagrangian framework, and the coupling between phases is introduced through particle sources in the Eulerian gas-phase equations.

The two-dimensional axisymmetric model was selected to describe the swirling flow, because of the axial symmetry of the chamber of the BFR, the inlet conditions, and the much greater computing efficiency for solid fuel combustion simulations compared to 3-D models. The model's detailed descriptions appear in Appendix G.

The elemental composition inputs (mole fractions, on a dry ash free basis) of the probability density function (pdf) calculation are listed in Table 5.1. Here sulfur is not considered because of the limitation inherited from the non-premixed model in FLUENT™.

Table 5.1 Composition and thermal properties inputs during the cofiring PDF calculations.

	50S50BC	70S30BC	70SD30BC	70S30P	70SD30P
Element mole fraction (daf)					
C	0.376	0.343	0.355	0.368	0.380
H	0.441	0.447	0.459	0.443	0.455
N	0.007	0.006	0.004	0.006	0.004
O	0.177	0.204	0.182	0.183	0.161
Net calorific value (MJ/kg)	21.8	19.4	20.9	20.6	22.1
Heat capacity (J/kg K)	1100	1100	1100	1100	1100

Ash is assumed to be inert and its impact on the reactor walls is not considered.

The wall temperature linearly decreases from the BFR top section, based on the temperature profiles monitored during the tests.

The chemical percolation devolatilization (cpd) model simulates particle devolatilization for both coal and biomass. Since biomass has a larger particle size than coal, its char oxidation is modeled by diffusion-limited surface reactions, and coal char oxidation is simulated with a kinetic/diffusion control model. The related parameters in

the combustion modeling are listed in Table 5.2. The adequacy of such models for biomass is suspect and is the subject of a separate investigation (Lu et al. 2005) in this research group. However, these simple models were used to obtain approximate velocity and temperature fields.

In the axisymmetric model, unstructured grids (Figure 5.5) were used from the primary inlet to 80 cm downstream of the quarl, since previous data showed this is where the internal recirculation zone develops.

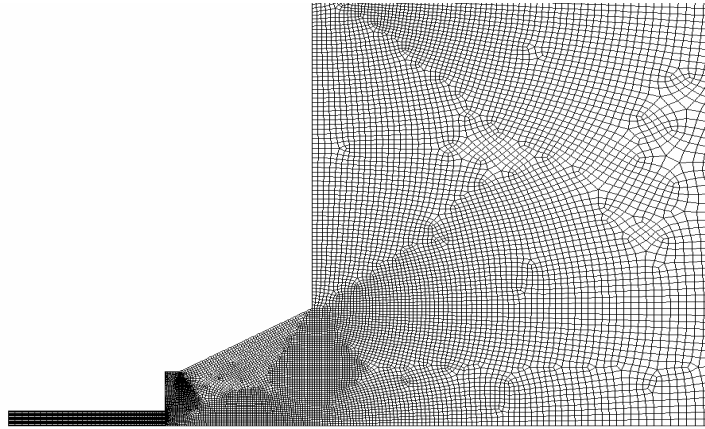


Figure 5.5 Grids set-up in the near inlet region of the axisymmetric combustion models.

Particle shape factor significantly impacts both the motion and reaction of a particle, since the drag and lift forces are both shape factor- and orientation-dependent. It is very significant to take into account the non-sphericity of biomass particles to model biomass combustion more accurately (Lu et al. 2005; Yin et al. 2004). In FLUENTTM, coupled particle rotation equations are resolved to update particle orientation. Spherical coal particles are generally assumed, that is, shape factor (the surface area ratio of the sphere with the same volume as the fuel particle to the latter) is 1.0. In the current project, biomass particles assume a shape factor of 0.2.

Table 5.2 Parameters selected and inputs in the combustion modeling.

	Blind Canyon	Pittsburgh #8	Straw	Sawdust
Rosin Rammler particle size distribution				
Spread parameter	1.14	1.14	2.76	1.19
d_{min} (μm)	20	20	120	160
d_{max} (μm)	350	350	720	650
$d_{average}$ (μm)	70	70	475	370
Shape factor	1	1	0.2	0.2
Density (kg/m^3)	1300	1300	700	700
Thermal conductivity (W/m K)	0.0454	0.0454	0.0454	0.0454
Latent heat	0	0	0	0
Vaporization temperature (K)	300	300	300	300
Volatile fraction (%)	50	40	90	95
Binary diffusivity (m/s^2)	0.0005	0.0005	0.0005	0.0005
Particle emissivity	0.8	0.8	0.8	0.8
Particle scattering factor	0.6	0.6	0.6	0.6
Swelling coefficient	1.1	1.1	0.56	0.56
Burnout stoichiometric ratio (%)	1.33	1.33	2.67	2.67
Combustion fraction	50	60	10	5
CPD model				
P_0	0.49	0.62	1	1
C_0	0	0	0.15	0.15
$\sigma + 1$	5.1	4.5	3	3
$M_{w_{c1}}$	36	24	81	81
M_{w_s}	359	294	22.67	22.67
Mass diffusion-limited rate constant	5.00E-12	5.00E-12		
pre-exponential factor	0.917	0.917		
Activation energy (J/kg-mol)	1.08e8	1.08e8		

5.4 Modeling strategy verification

Velocity results from the axisymmetric simulation of Black Thunder combustion are compared to the LDV data in the measurements from the previous project (Tree 2002). The test featured an overall stoichiometric ratio of 1.1 and a swirl number of 1.5.

The predictions of axial velocity reveal the existence of both an internal recirculation zone (IRZ) and an external recirculation zone (ERZ) under these operating conditions, as illustrated in Figure 5.6. The axisymmetric IRZ is roughly twice as long as the quarl and forms within millimeters of the burner outlet. The ERZ resides near the upper corner of the reactor walls.

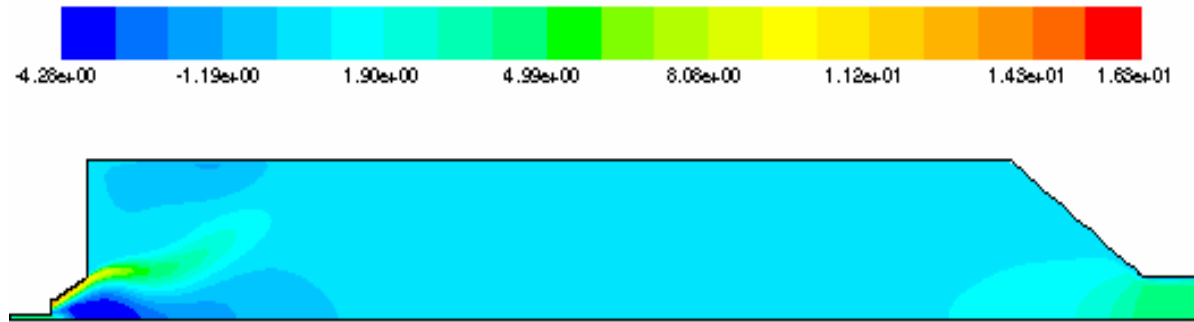


Figure 5.6 Axial velocity contours in the Black Thunder simulations ($\phi = 1.1$, swirl number = 1.5).

Detailed comparisons of axial and tangential velocity components at different axial locations appear in Figure 5.7 and Figure 5.8. Axial velocity predictions near the inlet region reasonably agree with the LDV data. In the radial direction, both axial and tangential velocity components exhibit less satisfactory agreement from the centerline to about half of the reactor radius (about 18 cm), where a large velocity gradient appears. For the data collected on the 15 cm plane, the flame front resides in the centerline-to-half-radius region, resulting in large velocity and temperature gradients.

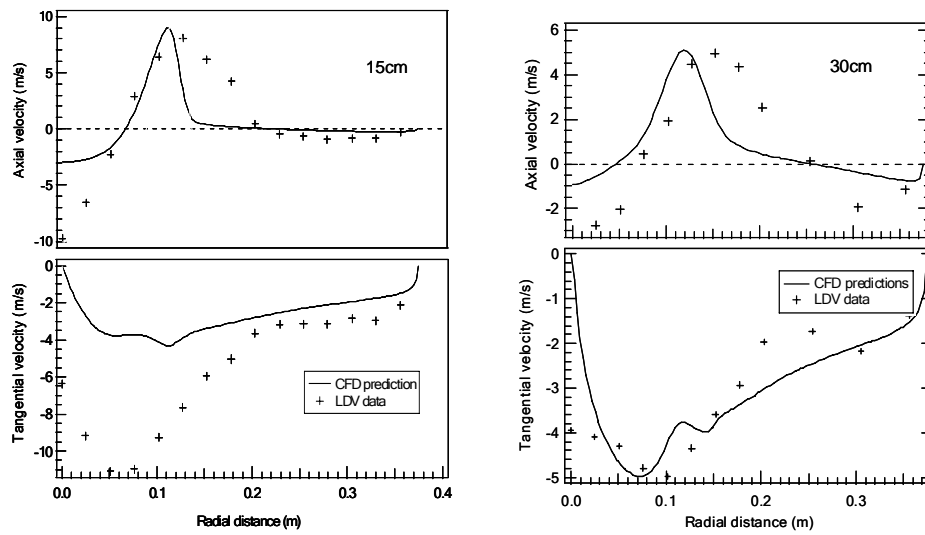


Figure 5.7 Comparison of the hot-flow axial, tangential velocity profiles from the CFD prediction and the LDV data at different axial distances (15 cm and 30 cm) (Tree 2002) during the Black Thunder test ($\phi = 1.1$, swirl number = 1.5).

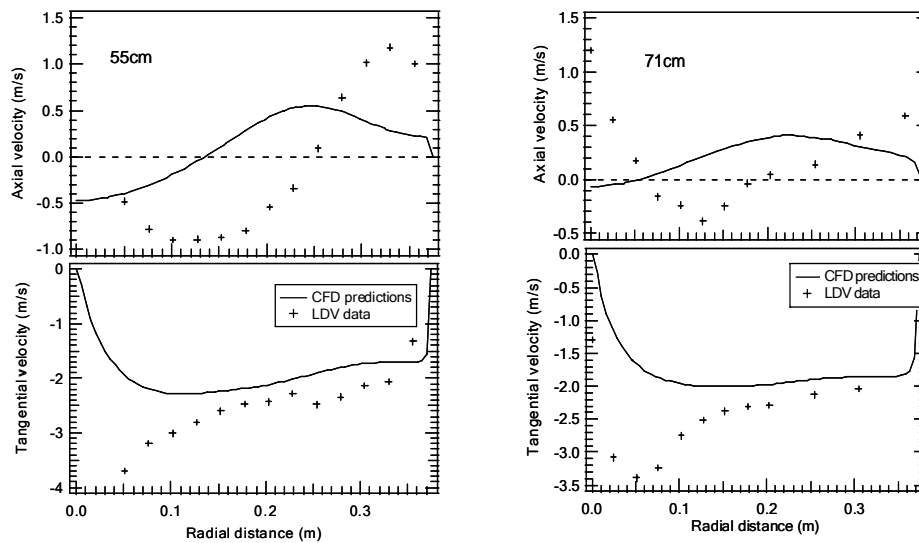


Figure 5.8 Comparison of the hot-flow axial, tangential velocity profiles from the CFD prediction and the LDV data at different axial distances (55 cm and 71 cm) (Tree 2002) during the Black Thunder test ($\phi = 1.1$, swirl number = 1.5).

The data here represent state-of-the-art estimates of velocities. They indicate sometimes significant departures from symmetry, as symmetric flows have zero tangential velocities at the center. There are also some inconsistencies. For example, angular momentum is nearly conserved (except for viscous dissipation) in flows. Relative to predictions, the data show sometimes smaller but generally higher total angular momentum. In general, the agreement between data and predictions is less satisfactory for these reacting flows owing in large measure to model inadequacies but perhaps in some measure to the difficulty of making such measurements in such hostile environments.

A reliable temperature quantification tool is currently not available for the turbulent combustion region in this project. Suction pyrometer data from previous work provide additional code validation. Spatial temperature data obtained during the Black Thunder combustion tests from the BFR appear below.

Hereby a brief description is provided on the suction pyrometer temperature measurement. At the measurement position, gas is aspirated through a pyrometer designed to minimize convective and especially radiative heat losses. The pyrometer consists of annular tubes, with a thermocouple near the center of the innermost tube. Combustion gases pass through the tubes, which quickly come to thermal equilibrium with their surroundings. The local gas temperature commonly exceeds the outermost tube temperature because the latter radiates to the (relatively cool) walls. The outermost tube radiatively shields the next outermost tube, which is therefore nearer the local gas temperature. A series of such tubes allows the thermocouple in the center to approach the local gas temperature, although the tubes and other probe features limit the spatial and

temporal resolution obtainable by this technique. In addition, the particles in the sample may bias the measured data. This technique is not suitable for recirculating regions or regions with steep temperature or velocity gradients because of its large impact on local flow structure and spatial averaging inherent in the technique. The influence of slagging on the sampling temperature could be significant.

Comparisons of the temperature profiles predicted from the CFD modeling and suction pyrometer data from coal combustion cases at different axial positions in the BFR appear in Figure 5.9.

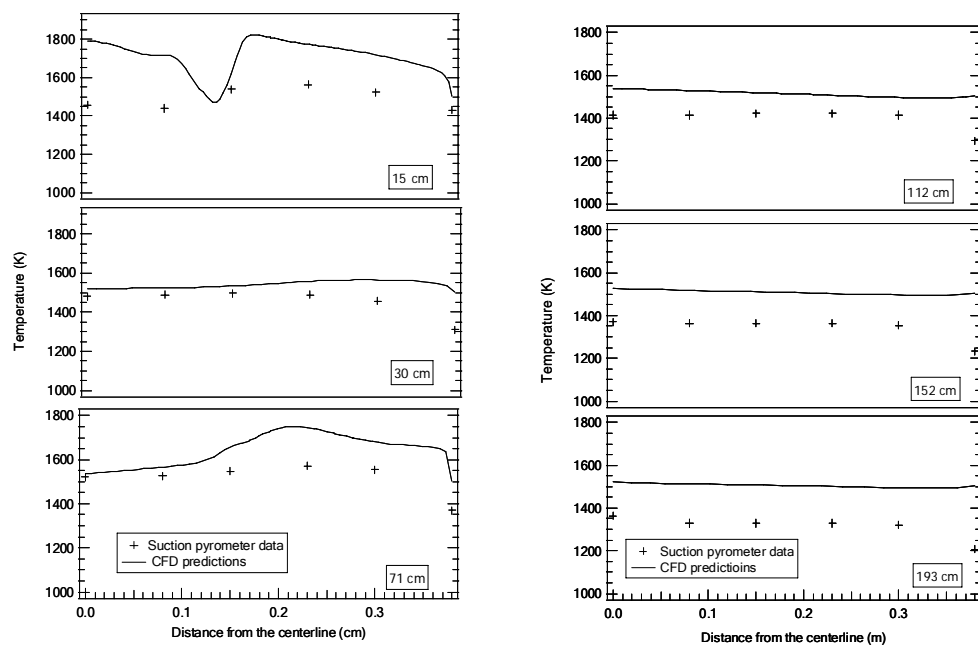


Figure 5.9 Comparison of the gas flow temperature profiles from the CFD prediction and the experimental data at different axial distances (Nazeer 1997) during the Black Thunder test ($\phi = 1.1$, swirl number = 1.5).

The predictions indicate a temperature gradient in the top section, with a large discrepancy, about 400 K, between the predictions and the data in the centerline region.

For reasons just discussed, the data might be several hundred Kelvins in error. The CFD predictions could also be in error by several hundred degrees with the quarl defined as a constant temperature of 300 K. It is difficult to determine which error is larger.

Both the prediction and data show flat profiles of gas temperature at larger axial distances from the burner, and the difference between the two drops to about 50 K. Aside from the near-burner centerline results, the temperature predictions generally agree with measurements within a few percent.

The average velocity and composition data thus far discussed illustrate the complexity of the average spatial velocity and composition gradients but belie the complexity of the instantaneous properties and temporal behavior. The entire reactor, and particularly the turbulent reverse flow region, interacts with the locally ever changing pressure and momentum fluxes, making point-measurement of the gas species challenging. The turbulent combustion region involves rapidly varying flow, temperature and gas species fields, driven by delicate pressure and momentum balances. The remaining discussion focuses exclusively on measured and predicted average flow properties. Temporal resolution of these fluctuations is well beyond the scope of this project. Nevertheless, the fluctuations figure prominently in interpreting the results. In summary, as a cost-effective quantitative analysis tool, the simple CFD models developed in this project generally predict the trend of cold/hot-flow velocity profiles in the turbulent swirling flow region, possibly as accurately as they appear to be measured. Species composition predictions, in particular HCN and NH_3 predictions, are not reliable from this simple code. Possibly, these nitrogen species measurements reported here can provide a benchmark for further refinement and upgrade of current models.

5.5 Summary

A new strategy of CFD modeling with commercial software, FLUENTTM, was used to obtain velocity and temperature information, verified by available experimental data collected from the same reactor used in this project. A three-dimension CFD model was developed and capable of accurately simulating the swirl-generator cold-flow performance. Its velocity predictions at 5mm below the primary air pipe were adopted to define the inlet for the two-dimension axisymmetric combustion model. Though the predictions of both temperature and velocity deviate from the data, especially in the reverse flow region, the general trends of these variables appear adequately predicted by the CFD code.

Chapter 6 Results and Discussions

This section is organized as follows: First, measurement consistency of the two analyzers in the gas sampling systems are described; Second, data repeatability and general characteristics of the results are discussed and illustrated with data from a pure coal test (Test BC), supplemented with the CFD predictions of axial velocity, temperature, and species; Third, results from the pure biomass tests and cofiring tests are compared with Test BC results; Fourth, data consistency and quality are investigated based on the stoichiometric ratio maps and conversion of the nominally axisymmetric data into normalized profiles on each horizontal plane; Fifth, a discussion on the biomass cofiring impact on the flame structure is focuses on three distinguishing characteristics of biomass fuels relative to pulverized coal particles: large particle size, high volatile content, and altered fluid dynamics; Sixth and finally, a discussion of NO_x formation is based on NO_x intermediate profiles, exhaust NO_x emission levels, and related kinetic calculations.

6.1 Consistency between the two analyzers

As mentioned in Section 4.2.3, O_2 can only be measured with the Horiba analyzer, and HCN and NH_3 are solely quantified by the MKS analyzer. Four species, CO, CO_2 , SO_2 , and NO, were measured with both the Horiba and MKS analyzers. Measurement consistency provides indication of data reliability, as discussed below.

Data from four species measured by both analyzers (SO_2 , CO , CO_2 , and NO) from three tests (one test in the case of SO_2) appear below, including one pure coal test (Blind Canyon), one cofiring test (70% sawdust 30% Blind Canyon), and one pure biomass test (sawdust). These data sets illustrate consistency and precision of the measurements. All measurements were calibrated with NIST-certified standard gases prior to each test for the Horiba analyzer, providing some assurance of accuracy and mitigating against systematic analyzer errors. Figure 6.1 and Figure 6.2 compare the results of the two independent analyzers over broad ranges of composition.

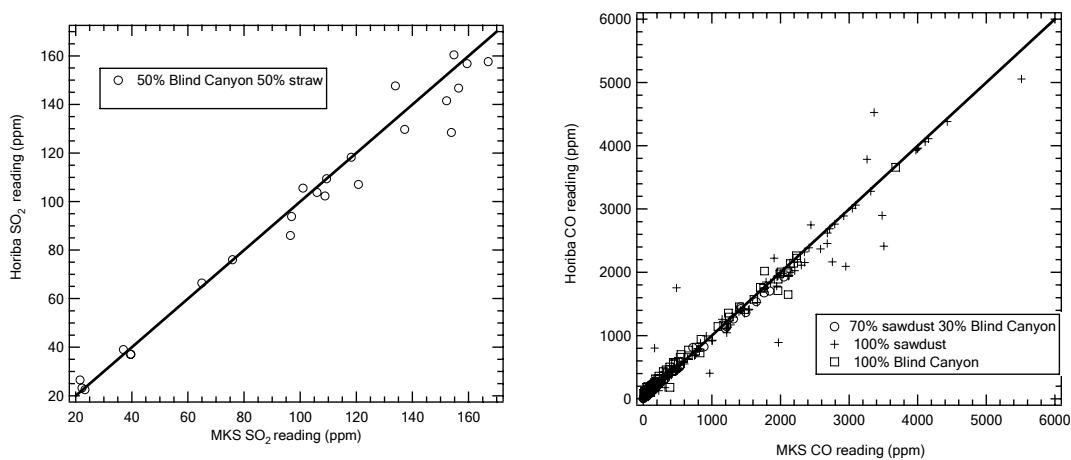


Figure 6.1 Comparison of the real-time reading at the same position by the Horiba and MKS analyzers: SO_2 and CO_2 , during one cofiring case only (50% straw 50% Blind Canyon) and three cases (straw, Blind Canyon, and 70% straw 30% Blind Canyon), respectively.

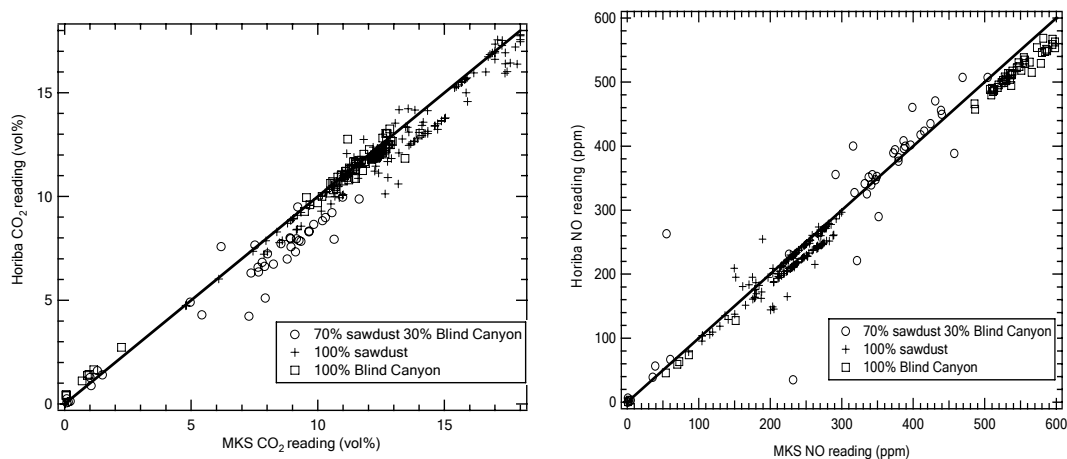


Figure 6.2 Comparison of the real-time reading at the same position by the Horiba and MKS analyzers: CO and NO during three cases (straw, Blind Canyon, and 70% straw 30% Blind Canyon).

Among the four species measured by both analyzers, SO_2 has the longest response time (five minutes). Collecting these data with both instruments strained the limited amount of fuel available to get a full species map. Therefore, only one cofiring case (50% straw 50% Blind Canyon) includes complete datasets from both analyzers for SO_2 . The correlation coefficient for the SO_2 data is 0.988.

CO has shortest response time in both devices among all the gas species. The CO readings from both analyzers match better than the other species, with correlation coefficients in Tests BC, 70SD30BC, and SD of 0.998, 0.995, and 0.981, respectively.

CO_2 and NO require longer response times than CO. In this configuration, the CO_2 data show better agreement (correlation coefficient: 0.986) than those of NO (0.961), which might be due to the differences in quantification techniques. The Horiba analyzer uses NDIR (non-dispersive infrared) spectroscopy to measure CO_2 , while an FTIR spectrometer (a dispersive instrument) provides raw data for the MKS analyzer. The two

methods share some wavelengths for some samples, but the signal collection and analysis methodology differ. As for NO, the technical difference is much larger than for CO₂ between the two analyzers. The Horiba instrument uses chemical conversion followed by chemiluminescence to determine NO: NO is converted to NO₂, and the latter reaches an excited state before releasing electrons, which causes luminescence that is used to quantify the NO. This technique differs radically from the FTIR spectroscopy technique used by the MKS instrument. As shown in Figure 6.2, bias exists and sometimes can be extreme for a few points among the NO results. However, most data demonstrate a reasonable consistency during the tests.

With respect to data from tests from different fuel combinations, the pure coal data compare most closely. As the fraction of biomass increases, the agreement between the two devices decreases, as shown in the figures. This might result from the sampling probe plugging with biomass particles, since the average biomass particle size is about six times larger than coal. Both analyzers have a requirement of constant sampling flow rate, and a partially plugged sample path impacts the flow rate.

Despite these inconsistencies, the data from both devices show satisfactory consistency. Data from both analyzers appear in the remaining analyses and discussion except for O₂, H₂O, HCN, and NH₃, which are only measured by one analyzer (Horiba for O₂ and MKS for the remaining species).

6.2 Description of the gas species profiles

This section discusses the pure Blind Canyon coal test (Test BC) data relative to CFD predictions. These verified species maps are compared with those from pure

biomass tests (Test S and Test SD), and from cofiring tests. The data illustrate differences in the major gas axisymmetric maps associated with larger particle size and higher volatile yield and their impacts on the swirling flow region. Because there was not enough Pittsburgh #8 for entire map, only measurements from two axial distances (40 cm and 160 cm) appear.

The gas species concentrations measurements appear in two-dimensional contours, and this added difficulty in comparing the fate of each species through the reactor between different tests. Therefore, alternative analysis methods that more clearly indicate trends are discussed in Section 6.3. This section focuses on the species two-dimensional profiles.

6.2.1 Benchmark: pure coal test (Test BC)

The Blind Canyon test provides important benchmark information for comparison when biomass is added. Especially, the replication and characteristics of the axisymmetric spatial gas species profiles, including CO, CO₂, O₂, and NO, indicate the repeatability and general structure of swirl-stabilized flames. CFD predictions of axial velocity, gas flow temperature, and species concentrations (CO, O₂, and CO₂) supplement the experimental data. The discussion involving NO and its intermediates (NH₃ and HCN) appears in Section 6.5.

Results from two BC tests under the same operating conditions (Figure 6.3) illustrate data repeatability. The major gas species mole fraction data contour maps appear as a function of radial and axial position. The data represent results from a vertical slice of the reactor passing through its geometric centerline and including both radial

directions from this nominally axisymmetric centerline. In the maps, a high contour density represents regions of steep mole fraction gradient, indicating a reaction-dominant region or combustion zone or, less commonly, a region of rapid mixing. This zone expands vertically from the inlet to about 40 cm (within the top reactor section) and horizontally to nearly one-half of the reactor radius (20 cm). The regions with few contours denote the relatively flat profiles for each species, and this is where product gas species (mainly CO₂, NO, and H₂O) dominate, or the reacted-gas zone. Independently sampled maps of the species appear for each of the two tests, respectively. A general description of each species appears as below, followed by a discussion of the repeatability.

The symmetry of the data around the centerline is one test of data quality. As seen, all data exhibit a reasonably well-defined symmetry axis, but this axis deviates a few centimeters from the geometric center of the reactor. Given the size of the reactor and the complexity of the flow, this slightly offset symmetry axis represents a minor aberration in the results.

Another measure of data quality is consistency: regions of high CO are always accompanied by low CO₂, low NO, and high O₂ concentrations in each test. The reaction region for all species maps indicates consistent flame location and structure. In the reaction region, the shapes of each species contour resemble each other, confirming repeatability. Generally, across the reacted gas region, mole fractions for CO₂, CO and O₂ match within 10% when comparing the replicated tests. NO mole fraction contours show much larger differences ($\pm 30\%$) than those for the other species in the reacted-gas regions: one with a peak value nearly 400 ppm, and the other 600 ppm.

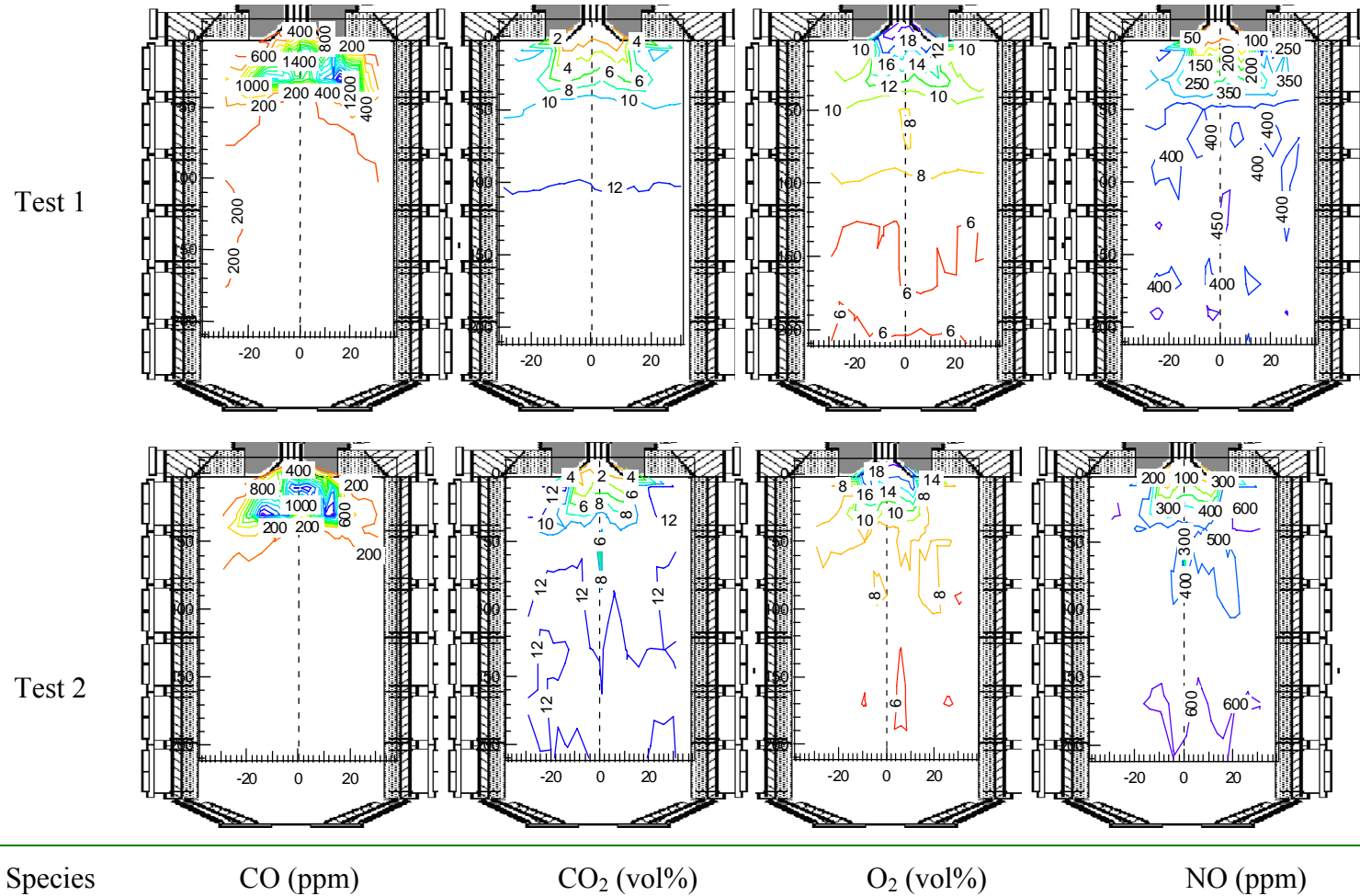


Figure 6.3 Comparison of major species contours from two Blind Canyon tests under same operating conditions. Both fuel and air entries locate at the top of the reactor, and the radial location unit is cm.

Figure 6.4 illustrates predicted contours of streamlines, reverse-flow, temperature and major species (O_2 , CO , and CO_2) simulating Test BC. As shown by the closed streamlines, both the internal recirculating zone (IRZ) and external recirculating zone (ERZ) are predicted by the current model. The IRZ extends within the top 80 cm vertically (within the top two section of the BFR) with a horizontal radius of nearly 15 cm. The colored region represents the axial velocity towards the inlet (top). The strongest backflow region locates near the axis right below the cooling-water quarl. Predictions of temperature and three gas species (O_2 , CO , and CO_2) display a high gradient region in the reactor top section (from 0 to 40 cm).

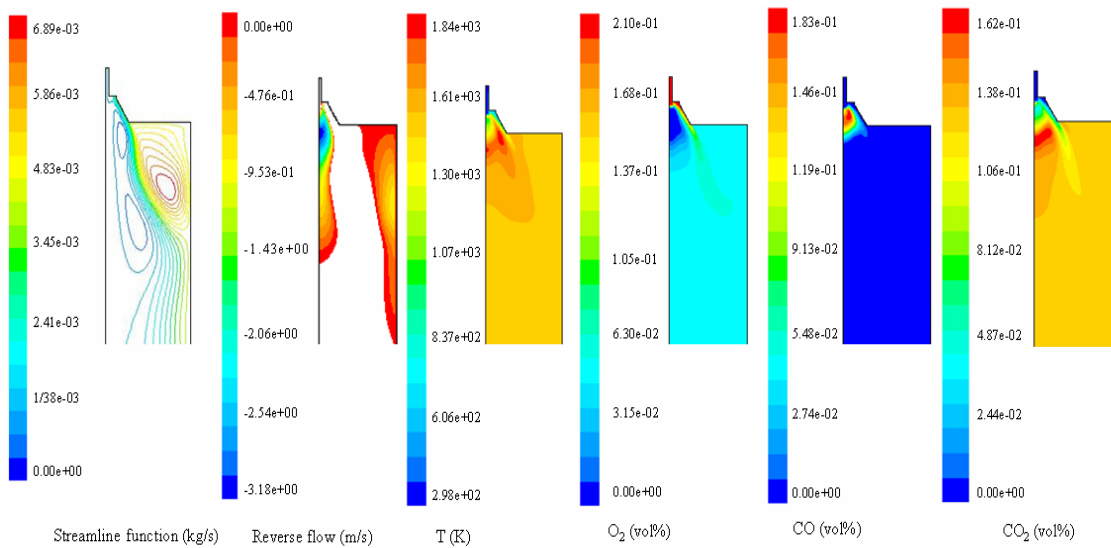


Figure 6.4 CFD prediction contours of streamline functions, axial velocity, reverse flow, gas-phase temperature, and major species (O_2 , CO , and CO_2) volume fractions from simulation of Test BC in the BFR.

When compared with the axisymmetric maps (Figure 6.3), the CFD simulations under-predict the combustion region size. Furthermore, the predicted O_2 -depleted region is not reflected in the data, and the predicted CO_2 peak isn't found in the corresponding

axisymmetric maps. The difference between CFD simulations and experimental data could be attributed to the following factors.

1. The relatively simple combustion model used here solves species profiles with an equilibrium-based mixture fraction approach, which is based on the assumption that the process is mixing-limited. This method has internal limitations in accurately simulating gas species profiles involved in turbulence chemistry under swirling-flow, low-grade fuel combustion conditions. Specifically, such techniques cannot predict kinetically impacted profiles such as CO.
2. The particle injection velocity was assumed to be independent of size. However, larger particles react more slowly to accelerating/decelerating carrying gases, potentially creating size-dependent velocities and changing positions where reactions initiate and continue.
3. The predictions assume a steady-state flame profile. In reality, the flame moves rapidly from place to place, leaving fluctuating fuel-rich and fuel-lean eddies in most regions of the reactor. While the pdf chemistry model used in these predictions incorporates some of this influence, its inability to accurately describe turbulence-chemistry interactions is a well-recognized limitation of CFD.
4. The point-measurement adopted in the current project represents the best method for collecting species data in the BFR. However, it is not without limitations. Specifically, this intrusive sampling method in the swirling flow environment unavoidably influences the aerodynamics of the sampled region in recirculating flows. The boundary of the combustion region, which is rich with incomplete combustion species such as CO and

radicals, represents a delicate fluid dynamic balance between competing momentum and pressure forces that the sampling probe inevitably disrupts.

5. The predicted oxygen-depleted region nearly overlaps with the IRZ core. Counter-intuitively, the O₂ reading in this region is high (from 8% to 18%, mole percent, Test BC, shown in Figure 6.3) rather than being close to zero as would be expected for a fuel-rich environment, and this is consistent with data from the same reactor during the Black Thunder coal combustion with swirl numbers ranging from 0 to 1.5 (Figure 2.9) in the reburning project (Tree 2002) and during straw firing/cofiring tests with a swirl number of 2.3 (Damstedt et al. 2005). This suggests a conceptually different model of near-burner flame structure than commonly appears in the literature. These data suggest that there is no region in this flame that is always under reducing conditions (always has an oxygen content of zero). Rather, a dispersed flame consisting of fuel-rich, presumably particle laden eddies separated by fuel lean eddies permeates the entire near burner region, with any individual location witnessing transient variation between the rich and lean eddies. The turbulent flow near the inlet and in regions of high composition and velocity gradients should lead to wildly fluctuating gas-phase species concentrations at each measurement point. However, the measurement is the time-average of each species within the probe diagnostic volume. Presumably the fuel-rich core would eventually form if the equivalence ratio becomes high enough, but over the broad range of equivalence ratios examined here (0.64-0.93), no case generated a consistently fuel-rich core. It is not clear if this is a feature of this particular burner or if it is a common phenomenon.

6. Isokinetic sampling under such widely fluctuating conditions is not possible. Non-isokinetic sampling of gases, unlike particles, leads only to changes in the size and local

location of the diagnostic volume, not to systematic biasing of the measurements.

Currently there exists no other method with the same accuracy, efficiency, or flexibility as the intrusive measurement techniques used in this project for gas composition in such particle-and soot-laden, larger-scale flows. The probe likely quenches most flames in its vicinity when sampling near the stoichiometric boundary and most active reacting regions, resulting in biases toward high oxygen and low fuel-rich species. All of the factors mentioned above could contribute to the fact that there is no zero or nearly zero O_2 region found in the combustion region.

A close comparison of the two Blind Canyon coal tests is provided by plotting the species profiles along a single horizontal sampling line in the IRZ, including NO , O_2 , CO_2 , and CO (Figure 6.5). The data symmetry is not perfect and the symmetry axis consistently misaligns with the geometric axis by a few centimeters. However, both the symmetry and the symmetry axis location indicate relatively high-quality data for such complex and large-scale systems.

These data illustrate measured profiles in the radial direction, located 12 cm from the reactor inlet. This location in the reactor contains among the steepest and most complex gradients in species concentration profiles (and all other properties) and therefore provides a rigorous test of both symmetry and reproducibility.

Combined with the reverse flow velocity predictions from CFD, it is obvious that large gradients of CO , CO_2 , O_2 , and NO appear around the reverse flow region (from -12 cm to 16 cm radially), and outside the region, there was much less variation in the species profiles. This verifies that the reverse flow region strongly influences combustion processes.

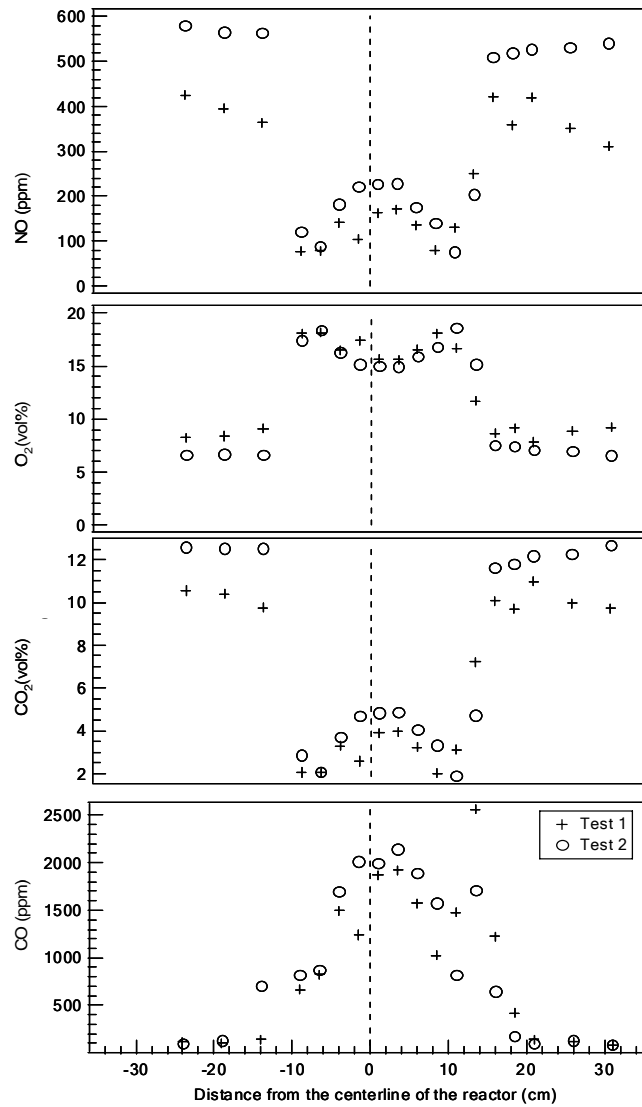


Figure 6.5 Results of replicate NO, O₂, CO₂, and CO measurements during two Blind Canyon tests positioned at an axial distance of 12 cm below the zero line (on a 3% O₂ basis).

The high CO reading (around 2000 ppm) might signal the existence of a locally fuel-rich region. However, CO generated from the decomposition of CO₂ at high temperatures (> 2400 K) could contribute to the high concentration of CO measured. This effect increases with increasing temperature (Lissianski et al. 2000). The measured peak

CO values of 2000 ppm (0.2 mole fraction) could only be generated by CO₂ disassociation at temperatures well above those measured or predicted in this reactor. However, additional evidence suggests these high CO values arise in large part from fuel-rich regions in the current experiments. The existence of HCN, NH₃, or both, accompanying the high CO region strongly indicate that a locally fuel-rich region exists at least transiently in these regions of the reactor. Kinetic and thermodynamic calculations show that neither HCN nor NH₃ survive a fuel-lean environment at 2000 K (Dean and Bozzelli 2000; Glarborg et al. 1998). Both species exist for a significant time (dozens of ms) in an overall fuel-rich environment, but less than 1 ms under fuel-lean conditions, which will be discussed in Section 6.5.4. Therefore, the simultaneous existence of HCN or NH₃ with CO confirms the region as being locally fuel-rich at least a portion of the time.

The top section of the BFR contains a region around the centerline characterized by high CO, and O₂ and low CO₂ molar concentrations. In this region, variations among the replicated data for all major and minor species are O₂, $\pm 10\%$; NO, $\pm 25\%$; CO, $\pm 10\%$; CO₂, $\pm 20\%$. Because of the turbulence impact, the O₂ measurement here is seemingly high.

In the near-wall region, the variation of some species between the two tests exceeds that observed near the centerline region. The disparity often increases as the probe approaches the reactor walls. The disparity in this region could arise from shifts in the local external recirculating region of gas flow. Such recirculating flows represent delicate balances in pressure and momentum forces. The sampling region (around the radial distance of 15 cm from the reaction centerline) corresponds to the approximate end

of the external recirculation zone, which appears to shift slightly from test to test – a subtlety of the flow pattern unable to be exactly reproduced in these experiments from one test to the next. The sampling probe may also influence the structure of such recirculating zones in ways not precisely known and difficult to predict.

6.2.2 Comparison of maps from biomass tests to that of Test BC

This section discusses experimental data from the two pure biomass tests, as appear in Figure 6.6, respectively. In the Test S (straw) maps, the blank region observed close to the left wall of the reactor results from the shortage of measurement points, not a low gradient region.

Generally, the combustion region of both pure biomass tests is similar to that of Test BC, with Test SD (sawdust) exhibiting a wider radial penetration. The high CO_2 reading in the reacted-gas zone in Test SD is caused by the operating equivalence ratio (0.90), as confirmed by the lower reacted-gas region O_2 mole fractions.

Axisymmetric maps of two biomass cofiring tests involving Blind Canyon coal and straw appear in Figure 6.8. The rest of the cofiring maps appear in Appendix H. In all the cofiring tests, the combustion region is larger in both axial and radial directions than in the Blind Canyon test: in Test 70S30BC, it reaches an axial distance around 60 cm, and during the other cofiring tests, it extends beyond the top two sections (over 80 cm). Section 6.4 discusses these differences in detail.

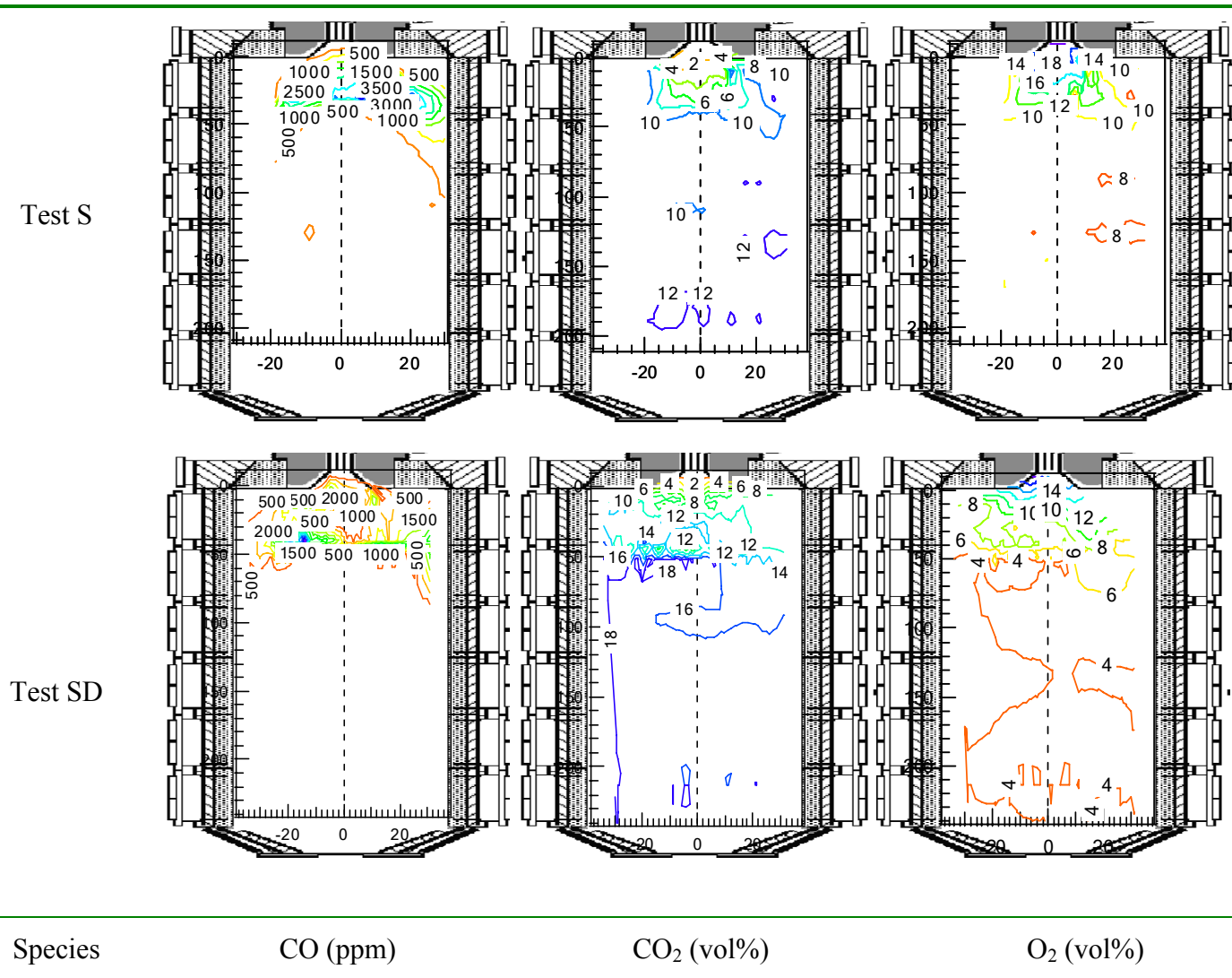


Figure 6.6 Species maps of the two pure biomass: Test S (straw) and Test SD (sawdust)

Below is a brief description of each species map.

Most of the CO detected resides in the top two sections (0-80 cm) in the reactor. The peak CO appears in a toroidal region at about 15 cm from the centerline and 30 cm from the inlet plane, occurring where the predicted axial velocity approaches zero as it changes from reverse flow to positive flow. From 80 cm and downstream, there is little change compared to that observed in the combustion regions. The high CO reading, which acts as a fuel-rich indicator, provides strong and definitive evidence of transient fuel-rich eddies under the overall fuel-lean conditions, as further indicated by the presence of HCN and NH₃, as described in Section 6.5.1.

CO₂ shows a monotonic increase with increasing distance from the inlet. Outside the combustion region, CO₂ reaches levels similar to that measured from the bottom section of the reactor. After the top two sections, the profile becomes nearly flat, indicating that solid fuel combustion is nearly complete within the top two reactor sections (0-80 cm).

In the combustion region, O₂ monotonically decreases with increasing distance from the inlet. Consistent with the CO₂ profile, outside the reverse region little variation in O₂ concentration appears. Comparing the CO and O₂ maps, high mole fractions of O₂ coexist with high mole fractions of CO, an interesting and quantitative feature of this combustor. A detailed discussion of this feature appears earlier (Section 6.2.1).

A description of NO maps appears in Section 6.5.2.

6.3 Experimental data analysis

This section is focused on the regressions of the experimental data for more insightful information on the biomass combustion behavior under swirling flows.

The axisymmetric species maps mentioned so far illustrate mole fraction distributions of major gas species during biomass combustion under swirling flow conditions, and demonstrate differences in the size of the combustion zone/fuel-rich region. These multidimensional data can also be used to reveal the performance of normalized mole fractions of each gas species, and NO_x formation analyses can be done, leading to insight into emission generation during biomass combustion.

Two methods of data analysis appear below. The first is to compute the spatial map of the stoichiometric ratio from the species maps, evaluating the impact of burning biomass on the flame structure. The second is to monitor the trends in gas species mole fractions as a function of axial distance. This can help reveal the effects of biomass high volatile content during firing/cofiring in the swirling flow region, as well as clarify the mixing and devolatilization effect in the near-burner region.

6.3.1 Stoichiometric ratio maps

The stoichiometric ratio is the inverse of equivalence ratio. Qualitatively, it is the air to fuel molar ratio in the existing system normalized by the same ratio under conditions of no excess of either fuel or oxidizer. Stoichiometric ratio is most commonly represented for the entire system, not just the gas phase. Calculations of stoichiometric ratio for complex systems such as these are not entirely straightforward because many of the species have several stable oxidation states, so distinguishing fuels from oxidizers can

be ambiguous. Furthermore, the biomass fuels are highly oxygenated, so a given stoichiometric ratio with biomass represents a significantly different environment than the same value for coal. To resolve these and other issues, an alternative definition of stoichiometric ratio is adopted here. The local stoichiometric ratio (φ) can be treated as the ratio of the oxidizing potential to the reducing potential. This can be mathematical expressed as follows (Baxter 2002a)

$$\varphi = \frac{\sum_j^s x_j \left(\sum_{i=0}^e -v_i n_{i,j} \middle|_{v_i < 0} \right)}{\sum_j^s x_j \left(\sum_{i=0}^e v_i n_{i,j} \middle|_{v_i > 0} \right)} \quad 6.1$$

where the symbols are defined as follows:

v_i : the reference oxidation state/valence of element i ;

$n_{i,j}$: the number of moles of element i in species j ;

x_j : the mole fraction of species j in the stream (which can be either reactants or products);

e and s : total number of elements in one species and the total number of species

respectively. The reference oxidation states are the valences under fully oxidized

conditions – not the actual valence of the element in the flow, i.e., C = +4, H = +1, O = -2,

Al = +3, N = 0, S = +4, etc.

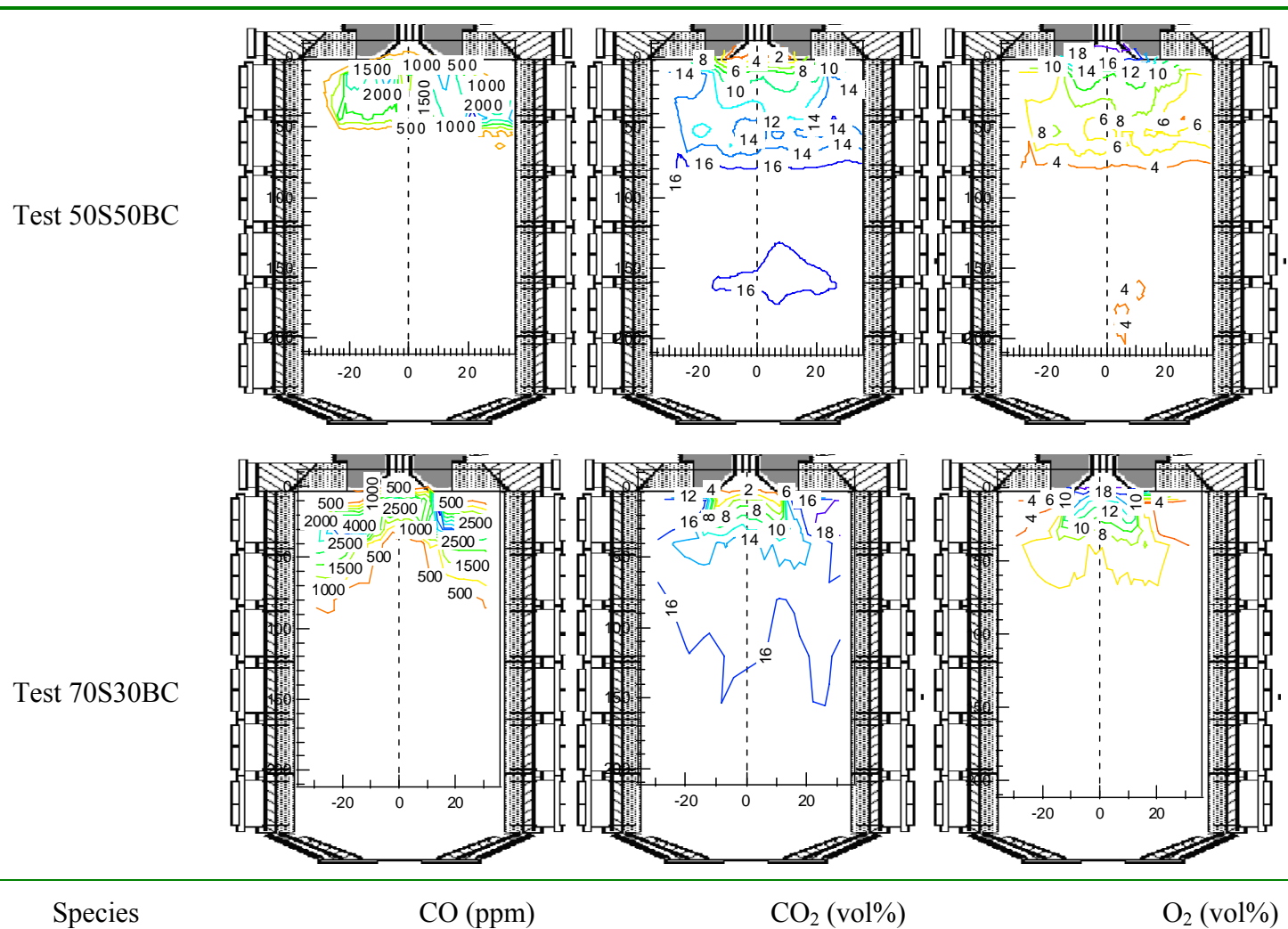


Figure 6.7 Species maps of the two cofiring tests: Test 50S50BC (50% straw and 50% Blind Canyon, wt) and Test 70S30BC (70% straw and 30% Blind Canyon, wt).

Molecular nitrogen and other atoms that exist in zero oxidation state at reference conditions do not impact the value of the equivalence ratio. Therefore, the only species of significance for this calculation include CO (in the fuel-rich region), CO₂, O₂, SO₂, and H₂O, with all others being of too low concentration to be significant in the calculation. Based on the measured species compositions, local gas-phase stoichiometric ratio is determined based on Equation 6.1.

6.3.2 Gas species normalized mole fractions (1-D profile)

The normalized gas species mole fractions along the reactor axis, termed a 1-D profile, are the ratio of the integration of the mole fractions with CFD temperature and axial velocity predictions across each horizontal plane, as described in the following equation.

$$Y_i(z) = \frac{\int_0^R \frac{P}{RT(r,z)} y_i(r,z) v(r,z) 2\pi r dr}{\int_0^R \frac{P}{RT(r,z)} v(r,z) 2\pi r dr} \quad 6.2$$

where the symbols are defined as follows

$Y_i(z)$: the mole fraction of species i on the horizontal plane with an axial distance of z ;

$T(r,z)$, $v(r,z)$, and $y_i(r,z)$: the temperature, axial velocity, and mole fractions of species i as functions of radial and axial position, respectively;

The mole fractions of species, $y_i(r,z)$, were determined from the measured values while the temperature and velocity were obtained from simulations. The reactor pressure P can be assumed as constant at 0.85 atm. R is the ideal gas constant.

In practice, P and R can be eliminated from the equation (assuming P is consistent from day to day) but are retained above to illustrate the derivation of the above equation. The integrand in the numerator represents the local molar flux times the mole fraction and the integrand in the denominator represents the local total molar flux. The function represents the flux-averaged mole fraction at a given axial position.

6.4 Features of biomass combustion under swirling flows

In this section, possible changes in the flow pattern during biomass combustion is discussed first, followed by a discussion on the influence of two features of biomass properties, large particle size and high content of volatiles.

Among the nine tests, as shown in Table 4.4, Test BC and Test S have relatively low equivalence ratios, 0.77 and 0.64, respectively. The ratios of the primary to secondary feed rates range from 0.52 (Test 50S50BC) to 0.134 (Test P). A parametric study was carried out with the modeling to verify the influence of changes in equivalence ratio and air set-up ratios on the reverse flow zone and gas species contours. Three cases were defined based on the operating conditions of a pure coal test, Test BC, and a biomass test, Test S, respectively. For the same fuel, all the cases have the same secondary air feed rate.

Case 1: The equivalence ratio and air set-up are same as those in Table 4.4, i.e. Test BC has an equivalence ratio of 0.77, Test S 0.64, and the air set-up ratios are 0.079 and 0.1, respectively.

Case 2: The equivalence ratio is 0.9, and air set-up ratio is 0.1.

Case 3: The equivalence ratio is 0.9, and air set-up ratio is 0.05.

The major gas species (CO and CO₂) and reverse axial velocity contours of straw and Blind Canyon combustion are shown in are shown in Figure 6.8 and Figure 6.9, respectively. For both groups, the simulation results show the combustion region, where the color gradient is high, resides in the similar location in the reactor, although the peak differs among the cases for the same fuel. The axial reverse flow velocity contours are of similar shape for the same fuel, and this shows there is little difference in the size and scale of the reverse flow region with the equivalence ratios and air set-ups considered for straw and Blind Canyon. Therefore, among the tests, even with smaller equivalence ratios (0.64, and 0.77) than the other tests and different air setups, modeling results indicate few qualitative differences in flows or structure.

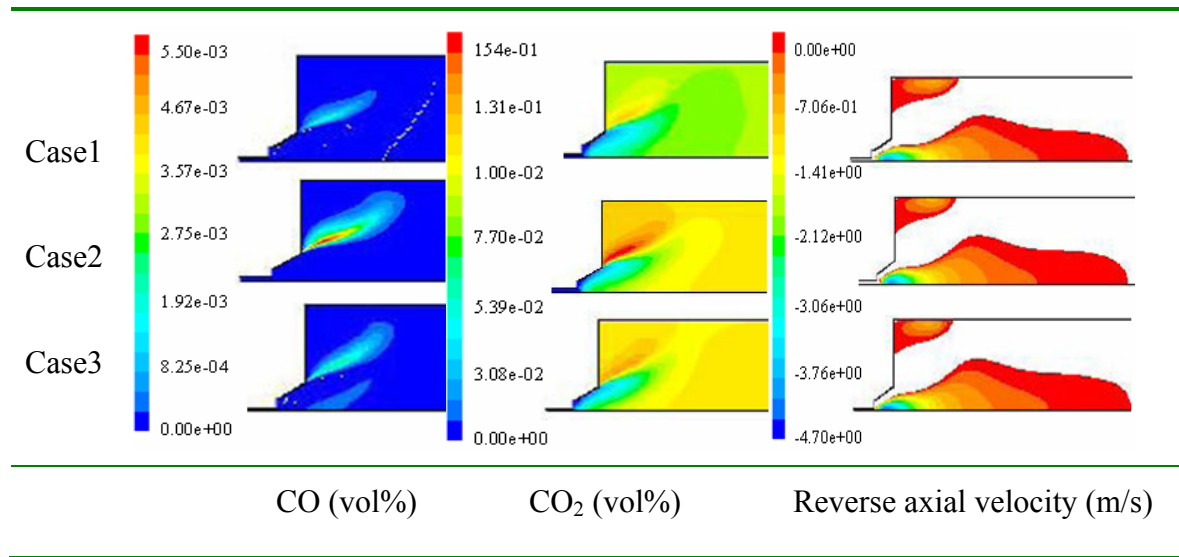


Figure 6.8 Contours of CO, CO₂ and axial reverse flow velocity from simulations of straw combustion.

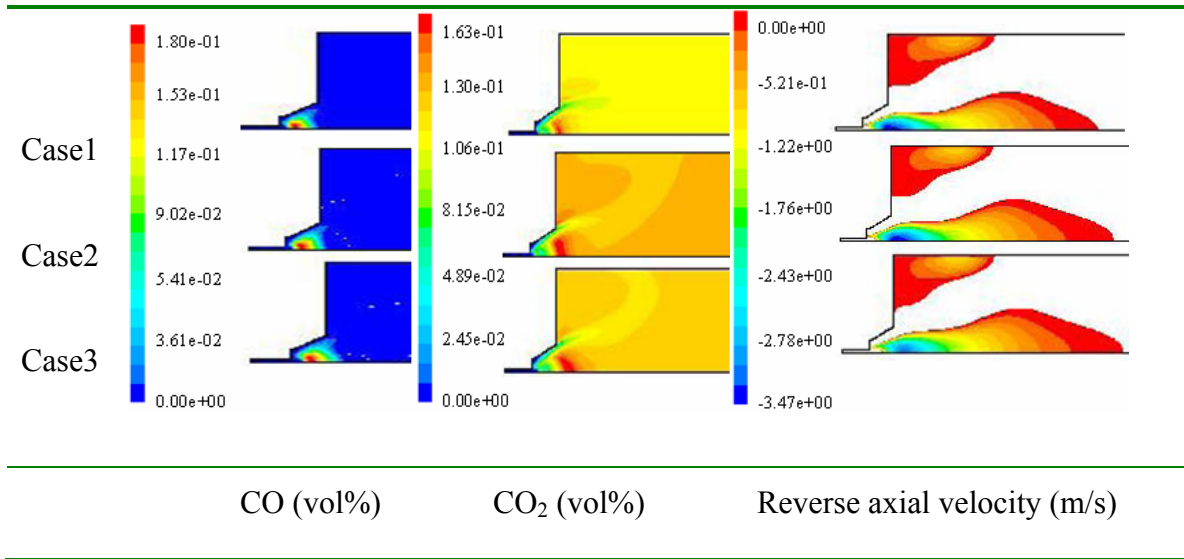


Figure 6.9 Contours of CO, CO₂ and axial reverse flow velocity from simulations of Blind Canyon combustion.

6.4.1 Flow pattern

This discussion compares predictions of reverse flow zones from biomass tests to those of the pure coal case (Test BC).

Figure 6.10 illustrates the predicted reverse flow contours from simulations of the single fuel tests (Test BC, P, S, and SD). For a better description, all the contours were plotted with the same scale (from -4.7 m/s to 0 m/s). Both the IRZ and ERZ are predicted to be axisymmetric. The core of the former resides around the reactor axis right below the quarl exit. Because of the differences in the ratio of primary air to the secondary air feed rates, the predicted peak reverse flow velocity varies among the tests. Test S has the highest secondary feed rate (150 kg/hr) and the strongest predicted peak reverse flow velocity (-4.7 m/s). Test P has the smallest secondary feeding (115 kg/hr) and the weakest

peak reverse velocity (-1.14 m/s, not shown in the figure). Test SD and Test P tests have the same secondary air feed rate, but the larger primary to secondary air flux ratio the latter (0.134) counteracts the scale of reverse flows, resulting in a less negative peak value in Test P than Test SD. The predicted size of IRZ also differs among these simulations, and this is caused by the air feed rate set-up. Modeling of Test BC predicts the smallest IRZ, and Test SD and Test S simulations demonstrate the largest IRZ. With the current relatively simple models, the observed differences in the IRZ size (discussed in the next section) couldn't be explained satisfactorily, but all the single fuel simulations indicate that combustion of biomass doesn't penetrate the IRZ or otherwise qualitatively alter the flow pattern in a swirling flow burner.

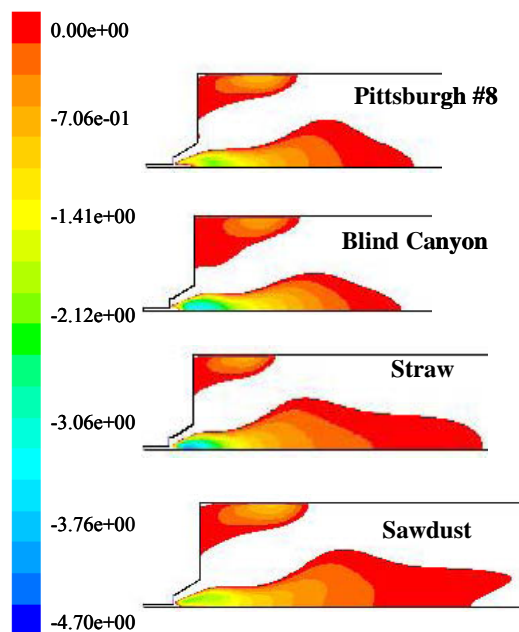


Figure 6.10 The reverse flow contours (m/s) predicted from simulations of the pure fuel tests.

The predictions of the IRZ from cofiring simulations are illustrated with cases involving both straw and Blind Canyon. The reverse flow contours are plotted in Figure

6.11. The flow pattern from cofiring simulations is similar to the pure fuel modeling results. The predictions indicate cofiring minimally impacts the qualitative features of flow dynamics. The swirling flow may be sufficient to sustain the adverse pressure zone (pressure gradient that increases in the direction of the average flow) around the centerline, resulting in a reverse flow region near the burner exit, even in the presence of the large biomass particles.

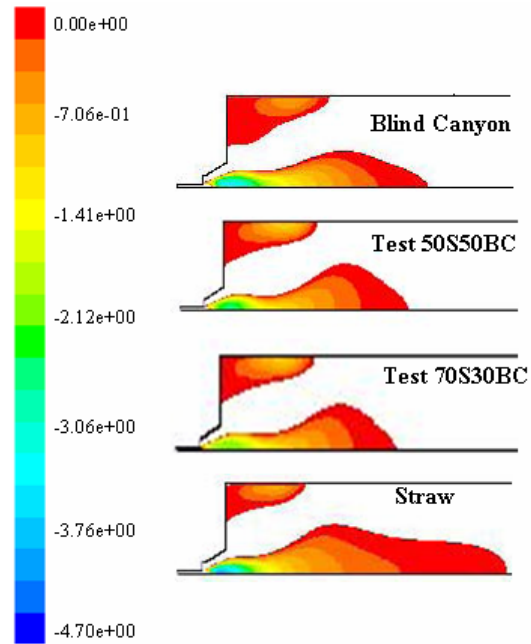


Figure 6.11 Comparison of reverse flow contours from the two cofiring tests and their corresponding pure fuel tests involving straw and Blind Canyon.

In summary, with the current modeling strategy, no qualitative change in the reverse flow pattern between biomass and coal combustion in the swirling flow burners appears. The impact of biomass combustion on the flow pattern might be limited. This indirectly indicates that the expansion of the size of the combustion region during biomass tests is possibly caused by the fuel properties, such as moisture content, volatile content, and particle size, as discussed in the next section.

6.4.2 Influence of biomass properties: particle size and volatile content

The particle size distributions of fuels used in this project appears in Figure 6.12. Straw has the largest average particle size (475 micron), larger than that of sawdust (370 micron). These values are much smaller than commercial fuels, which are on the order of millimeters or even centimeters. Both coals considered have an average particle size of 70 micron. In the CFD modeling, as mentioned previously (Table 5.2), sawdust is assumed to have a volatile content of 95% (mass basis), which is slightly higher than that of straw (90%), Pittsburgh #8 (60%) and Blind Canyon coal (50%). Sawdust generally has a higher volatile content than straw, and both are much higher than coal.

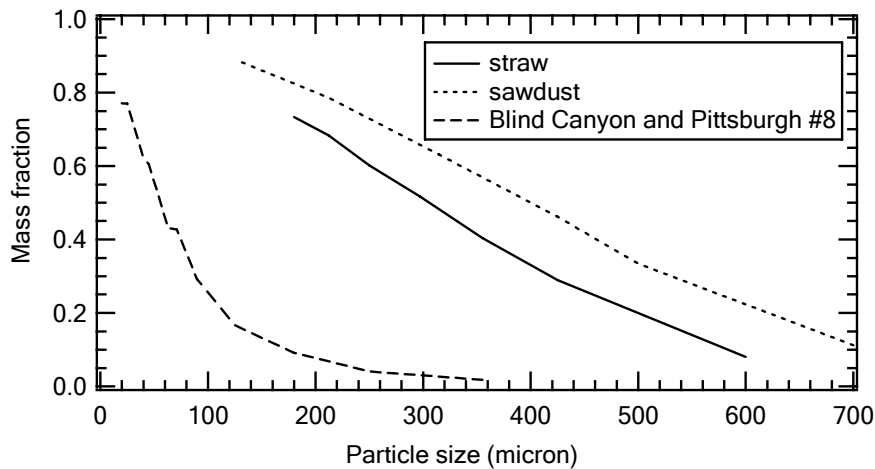


Figure 6.12 Distribution of particle size of biomass and coal used.

During this combustion process, for the same type of fuel, particles with a larger size need more oxygen and a longer time to both initiate (warm-up) and complete reactions. High volatiles contents mean more off-gases during devolatilization, generally CO, CO₂, H₂O, and a small amount of hydrocarbons. This facilitates the initiation of combustion and helps sustain flames by providing combustible gas mixtures.

The impact of the biomass particle size on combustion could be reflected from the comparison of predictions of CO and CO₂ from simulations of Test BC, Test SD, and Test S, in an order of increasing fuel particle size, as illustrated in Figure 6.13. For Test BC simulations, the high gradient region is attached to the inlet. Predictions of Test SD show insignificant expansion of the CO and CO₂ high-gradient region. For Test S, this region moves further downstream still. Combined with the biomass firing and cofiring axisymmetric maps mentioned in Section 6.2.2, these predictions provide qualitative information on the influence of particle size. The expansion of the combustion region can be explained as follows: after fuel is injected into the reactor against the recirculating preheated flow, devolatilization is quickly initiated. The Blind Canyon sample has a relatively low volatile content (50%), and the volatiles are rapidly consumed. Since biomass particles are larger (straw: 475 micron; sawdust: 370 micron) than Blind Canyon (70 micron), they heat more slowly and their devolatilization occurs further inside the reactor and, due to the larger volatile content (straw: 90%, wt; sawdust: 95%, wt; Blind Canyon: 50%, wt), biomass consumes more oxygen, causing the expansion of the high CO region (combustion region). Furthermore, biomass produces larger char particles than coal, despite the higher volatile content. Char particle combustion generally produces dominantly CO (as opposed to CO₂) and biomass will produce larger CO trails as the particle require longer to burn than do coal char particles.

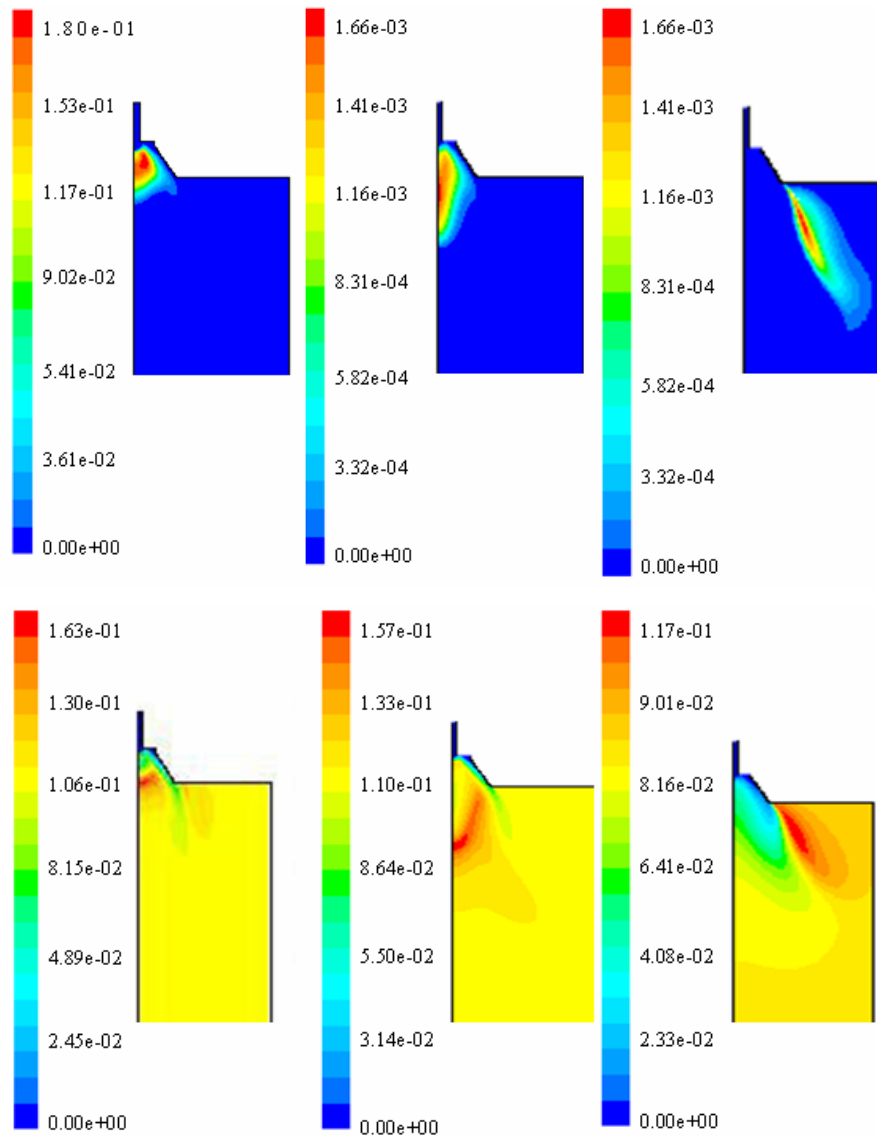


Figure 6.13 Comparisons of CFD predictions top: CO (ppm); bottom: CO₂ (vol %) of Test BC, Test SD, and Test S.

The 1-D gas species profiles from the pure fuel tests are displayed in Figure 6.14. The 1-D profiles for each species indicate that the pure biomass test data follow a similar pattern to that of the Blind Canyon test. At the inlet, represented by the origin in the graph, CO and CO₂ mole fractions are almost zero, while O₂ has a maximum

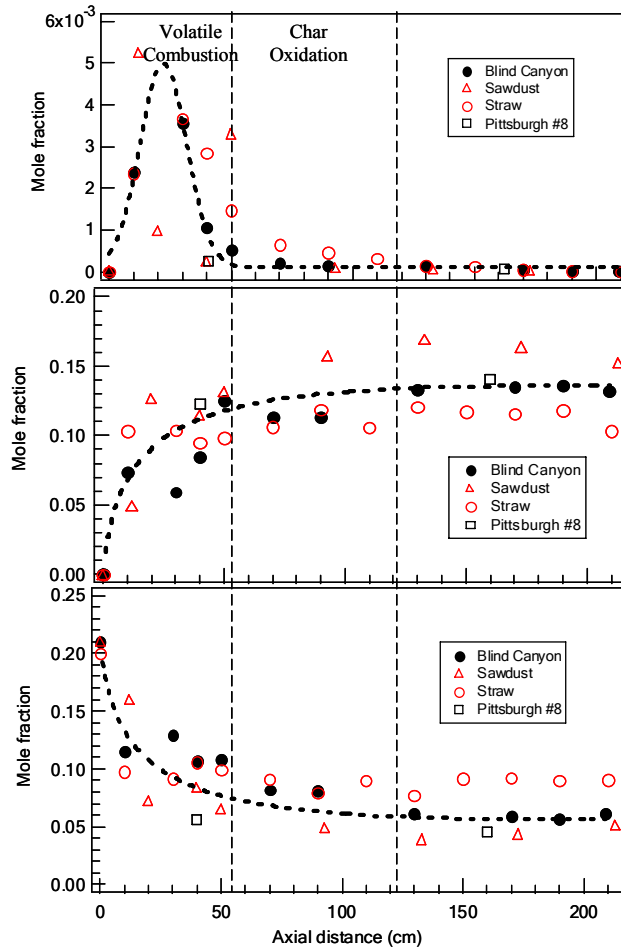


Figure 6.14 1-D profiles of CO (top), CO₂ (middle), and O₂ (bottom) during pure fuel tests (The dot-lines describe the trends of normalized results of Test BC along the reactor axis)

concentration, where the combustion process has not fully begun. With increasing axial distance (about 10 cm), particle devolatilization dominates the process, leading to a sharp increase in CO (from 0 to 2000 ppm for sawdust), accompanied with an increase (from 0 to 0.05, mole fraction) in CO₂ and a decrease (from 0.2 to 0.15, mole fraction) in O₂.

After enough mixing of air and fuel, from 10 cm to about 50 cm, CO reacts with oxygen in the mixing-controlled reactions, and about 80 % of the overall fuel is consumed by about 50 cm. Simultaneously, CO₂ monotonically increases, and O₂ is reduced by about 70% by 50 cm. It is from 0 to 50 cm where the main part of combustion happens and the

IRZ resides. Downstream of this region, CO continues decreasing until fully reacted by about 170 cm. CO₂ increases to a maximum level at about 130 cm. O₂ drops to a relative steady level at about 50 cm.

These 1-D profiles also provide evidence of the high volatile influence. Biomass is an oxygenated fuel, so CO reacts with oxygen released from volatiles in addition to O₂. Therefore, Test S data show much higher CO₂ and CO mole fractions in the top section (from 0 to 40 cm) compared to the coal data, even though its equivalence ratio (0.62) is lower than that of Test BC (0.77). The one presumably spurning CO data point at 50 cm of Test SD seems unlikely, since sawdust has higher volatile content and smaller particle size than straw, in the region where the reacted-gas and combustion regions overlap, there should be plenty oxygen supply to consume CO. It is very unlikely that the CO concentration is about three time of that from Test S. As a rule, the biomass combustion cases exhibit more rapidly increasing CO₂ profiles and CO profiles that penetrate further into the reactor compared to the Blind Canyon coal. Oxygen profiles reflect similar trends, with the coal oxygen consumption in the early section of the reactor (the top 50 cm) less than that of the biomass fuels. Similar trends appear whether comparison is mad with biomass at lower (straw: 0.64) or higher (sawdust: 0.90) equivalence ratios relative to that of the Blind Canyon coal.

Char has a much higher heat density than volatiles. In contrast to the high-volatile, low-char biomass properties, coal lacks volatiles and forms more char. Coal particles should follow gas stream lines more closely and mix more rapidly with gases in the swirling flows than do biomass particles. During the cofiring tests, both biomass and coal are injected simultaneously through the same path. The mixture contains

components with both high and low volatiles and fixed-carbon contents and large and small particle sizes. Stoichiometric ratio maps of the cofiring tests (Figure 6.15) indicate that attached flames with wide radial penetration occur compared to Test BC. The cofiring 1-D profiles of CO, CO₂, and O₂ are plotted in Figure 6.16, in which each species demonstrated a generally similar trend to that of Test BC. The data show high mass fractions (70%) of biomass leading to larger devolatilization regions remains evident. For example, much higher CO mole fractions from the cofiring tests than Test BC at 30 cm and 40cm, where the cofiring tests have higher 1-D CO₂ values and lower O₂ mole fractions than that from Test BC. These data suggest that biomass helps stabilize flames (as indicated by faster increases in CO and CO₂ mole fractions in the reactor), presumably because of its high volatiles content and despite its relatively large particle size. Furthermore, the size and intensity of the fuel-rich core (high CO region), as indicated by the magnitude and axial extent of the non-zero CO normalized mole fractions, increases with biomass cofiring, presumably for the same reason.

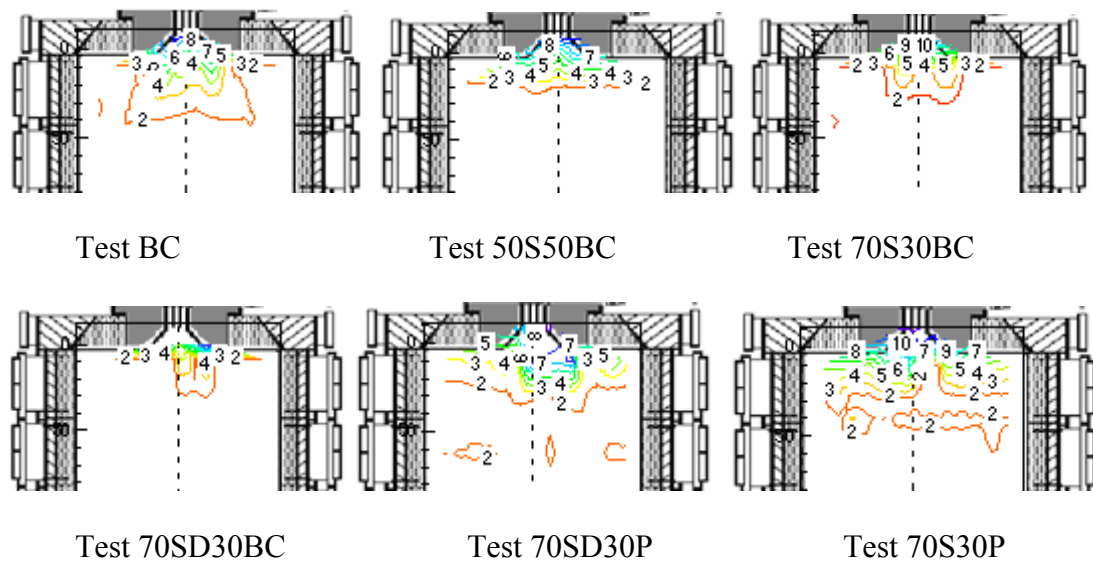


Figure 6.15 Stoichiometric ratio maps of the test of Blind Canyon coal and cofiring tests calculated based on Equation 6.1.

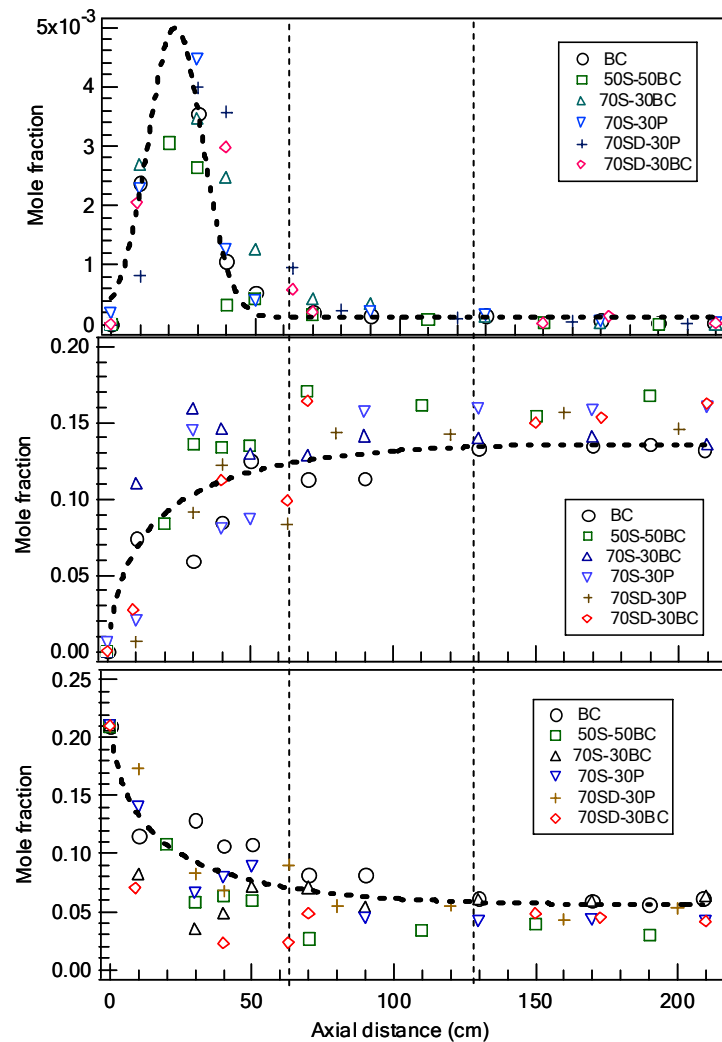


Figure 6.16 1-D profiles of CO (top), CO₂ (middle), and O₂ (bottom) during cofiring tests compared to that of Test BC (The lines show the trend of the normalized results of Test BC along the reactor axis)

6.5 NO_x formation during biomass combustion under swirling flows

This section discusses NO_x formation during biomass-coal combustion in a swirl-stabilized burner. The following aspects are considered: First, maps of important NO_x intermediates, HCN and NH₃, are analyzed. Second, NO data are compared among the biomass and coal tests, and the emission is analyzed on different bases. Third, the relation

between the intermediates and NO formation is discussed through the comparison of the conversion of fuel-N to NO among the tests, supplemented with kinetic calculations.

6.5.1 Measurements of HCN and NH₃

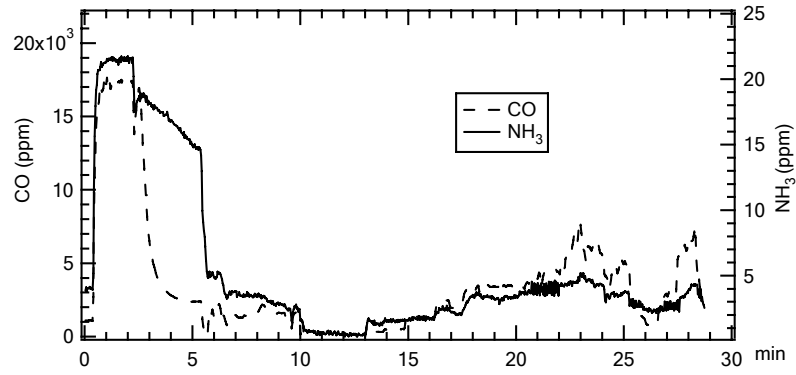
As mentioned in Section 2.2, the fuel-N in coal exists in the form of unsaturated cyclic nitrogen compounds, mostly clusters of pyrrolic and pyridinic forms. Biomass nitrogen resides dominantly in acyclic molecules such as derivatives of amine, amide, and amino acids. Based on the bond analysis between the possible nitrogenous products and the compounds in the parent fuels, HCN should be the dominant NO_x precursors in coal flames, while NH₃ should dominate during biomass combustion.

Indirect evidence of the minimal impact of sample conditioning, specifically water condensation, on the HCN/NH₃ concentrations appears in Figure 6.17, which illustrates the real-time measurement of NH₃ and HCN with their respective CO profiles from a pure straw test and pure coal (Blind Canyon) test. NH₃ probe measurements are calibrated with NIST-traceable calibration gas samples, while the HCN calibration relies on a theoretical spectra data base provided with the analyzer. HCN calibration gases are in principle available for calibration, but they pose unacceptably high safety risks and are not used in these tests. The figures indicate very high correlation between the CO and both the HCN and NH₃ signals. The oscillations in the NH₃, HCN, and CO profiles arises from alternating the probe position between the fuel-rich region and the reacted-gas region of the Blind Canyon and straw flames, with the intent to test the gas measurements at extreme conditions as major gas species concentrations change significantly. Though only very limited amounts (less than 15 ppm) of HCN and NH₃ are detected in the flue gas, the peak amounts appear at the same time as the peak CO content. While the

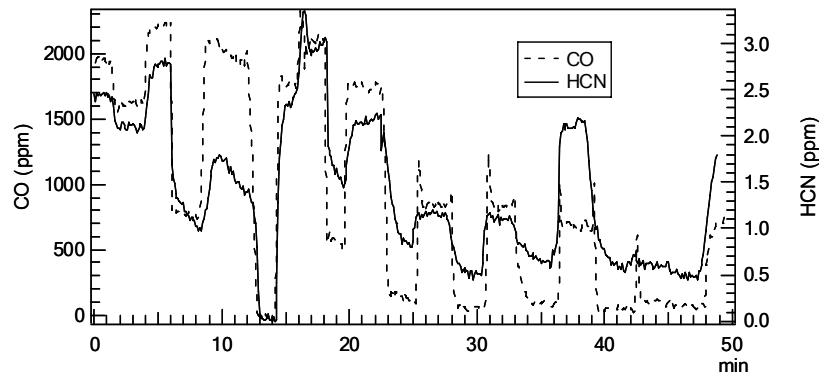
quantitative accuracy of the HCN measurements lacks direct validation by NIST-traceable calibration gases, it quantitatively correlates with other fuel-rich species (CO and NH₃), indicating that its measurement is at least semiquantitative (trends are quantitatively correct even if absolute magnitude may be in error). CO and NH₃ exhibit both of these characteristics and are quantitatively calibrated against standard gases.

Both HCN and NH₃ generally occur only in reducing environments, as indicated by the presence of CO. Water is present in quantities (typically 13-20%, mole percent) that greatly exceed CO, NH₃ or HCN in both (mildly) reducing and oxidizing conditions. Since the measured NH₃ and HCN closely follow fluctuations in CO and during their measurements and no water condensation was detected through the optical access in the cyclone (the lowest-temperature and elevation point in the sample train), the impact of water condensation on the gas sample should be limited.

These tests also give some indication of the time required for the sampling system to adjust to changes in the nitrogen-gas species concentrations. Ammonia, for example, adsorbs on many surfaces and it requires some time for the sampling line to adjust to changes in ammonia concentrations because of this adsorption. CO, however, does not appreciably absorb on probe surfaces so it is used as a reference to determine response times. These data indicate that the response time for ammonia in the probe varies depending on whether ammonia concentration increases or decreases but can be up to three or four minutes. HCN, on the other hand, also shows a variable response time but in all cases appears to respond in less time (within one or two minutes). In these tests, all gas concentrations were only recorded after all readings had stabilized.



(a)



(b)

Figure 6.17 Temporal variations in NH_3 and HCN concentrations compared to CO concentration in the swirling section of the BFR. (a) NH_3 with CO during Test S (b) HCN with CO during Test BC.

Consistent with the high CO mole fraction existing near the reactor inlet, HCN and NH_3 , when detected, were found mainly in the top section, 0-50 cm below the quarl. Though all the tests involved overall fuel-lean conditions, the existence of HCN/ NH_3 provides strong evidence that there is a locally and probably transient fuel-rich region in the top section of the reactor, corresponding to the reverse flow region. This section discusses spatial maps of HCN and NH_3 for different cofiring and pure biomass/coal tests and their implications on the flame behavior, supplemented with spatial profiles of CO and local stoichiometry.

Examples of HCN and NH₃ maps from the Test BC appear in Figure 6.18. The HCN peak values appear in similar regions as those of CO (Figure 6.3). The HCN data comfortably exceed the noise levels of the analyzer. NH₃ concentrations under this condition are too low to be measured with this system (< 1 ppm) and the patterns seen in the figure are not significant.

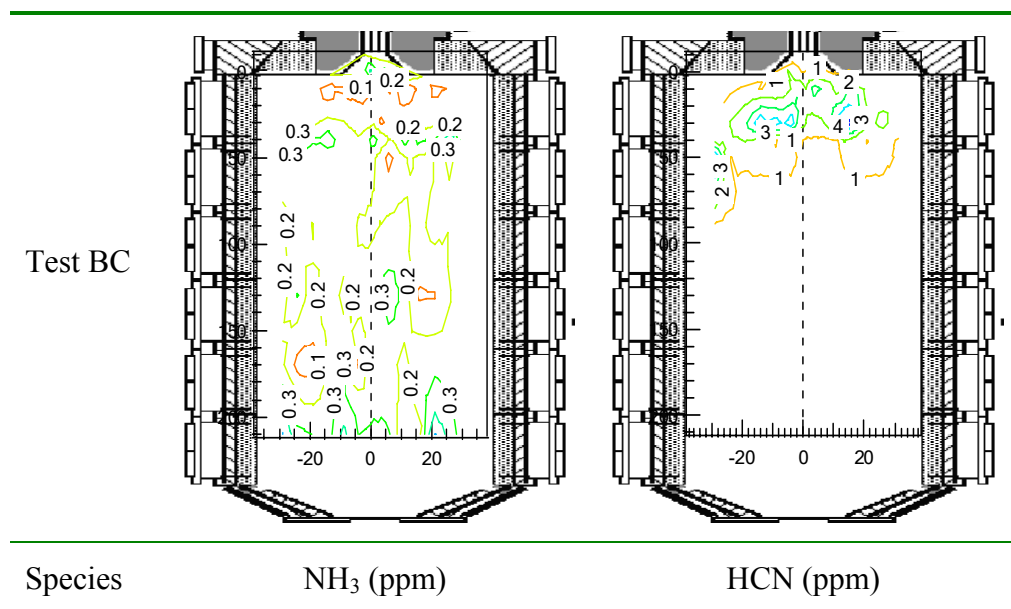


Figure 6.18 Two dimensional maps of HCN and NH₃ from Test BC. NH₃ data are below detection limits and the indicated patterns are not significant.

Figure 6.19 depicts the HCN and NH₃ maps from the three tests involving straw and Blind Canyon coal. In the coal test, HCN dominates NH₃ as the primary fixed-nitrogen species in the gas phase. The same is true in Test 50S50BC, and the test of 70S30BC. In Test S, NH₃ rises above the measurement limit and has higher concentration than HCN in the fuel-rich region. These data clearly show that straw and Blind Canyon release nitrogen in different forms and generate different NO_x intermediates.

The low fuel-N content in sawdust leads to NO_x intermediates during combustion that are too low to quantify under these conditions. The maps of HCN and NH₃ both

exhibit results at or near reliable detection limits (Figure 6.20). Strictly speaking, the NH_3 map sometimes indicates concentrations at or above the detection limit in the measurement region. The peak value in the HCN map coincides with that for NH_3 . This is attributable to the joint influence of unsteady local flame structure, the turbulent flow pattern and low fuel-N content.

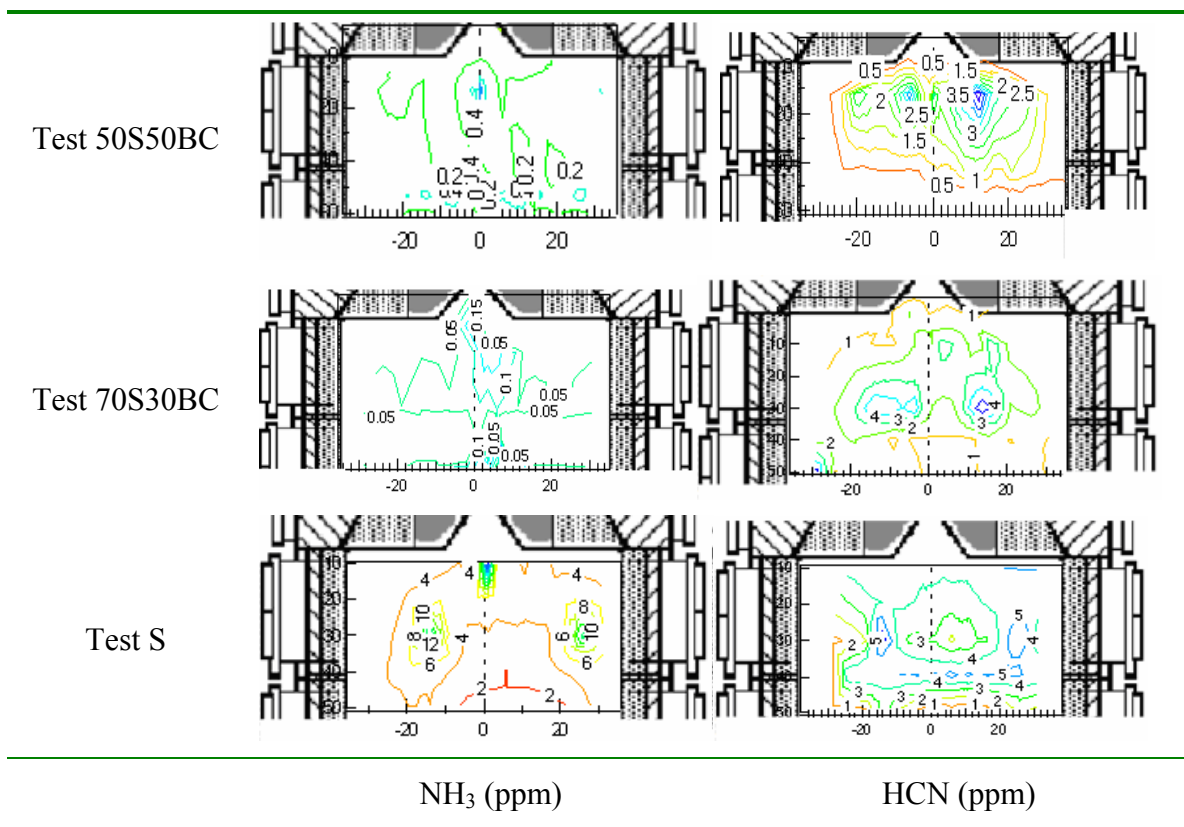


Figure 6.19 NH_3 and HCN maps from Test S, Test 70S30BC, and Test 50S50BC. The unit of radial distance from the centerline is cm.

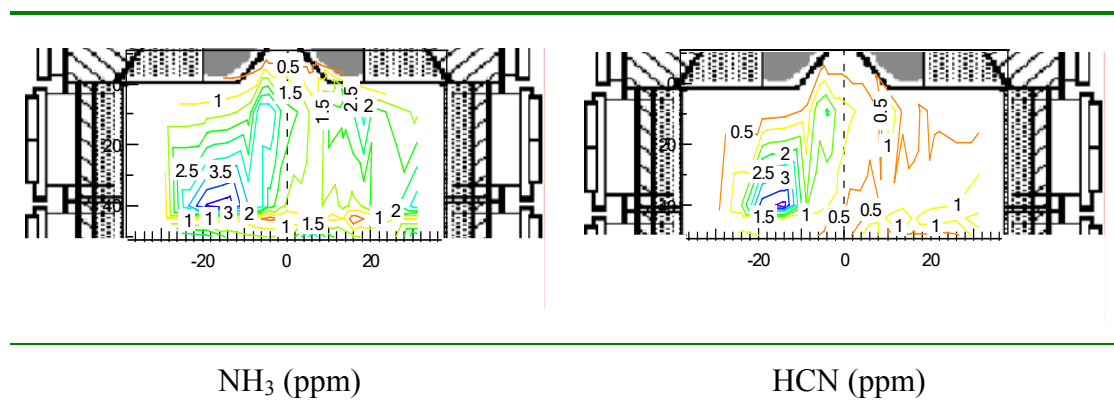


Figure 6.20 NH_3 and HCN maps from Test SD. The unit of radial distance from the centerline is cm.

In the current project, Test P was the last case, and there was not enough fuel left to complete a spatial map, so only measurements along two lines appear (40 cm and 160 cm). Compared to the data from Test SD, neither species in Test P comfortably exceed the detection limits of these instruments during these tests (Figure 6.21).

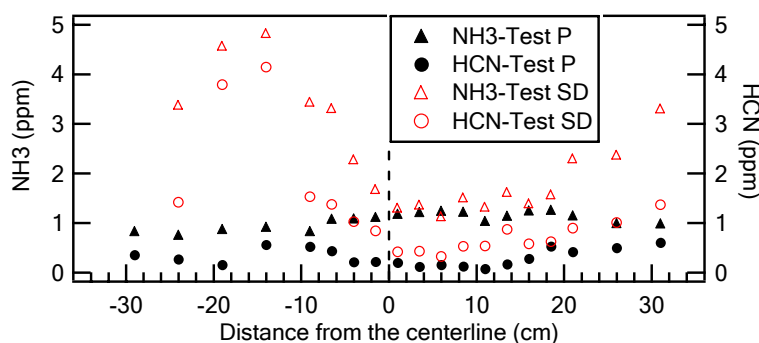


Figure 6.21 Comparison of NH_3 and HCN data at same position from Test SD and Test P.

In the cofiring case involving sawdust and the Pittsburgh #8 coal, Test 70SD30P, illustrated in Figure 6.22, the light nitrogenous species profiles have similar characteristics as that from Test SD. This is possibly caused by the high mass fraction of

sawdust in the fuel mixture, resulting in the amount of NH₃ or HCN released below the measurement limit of the current system.

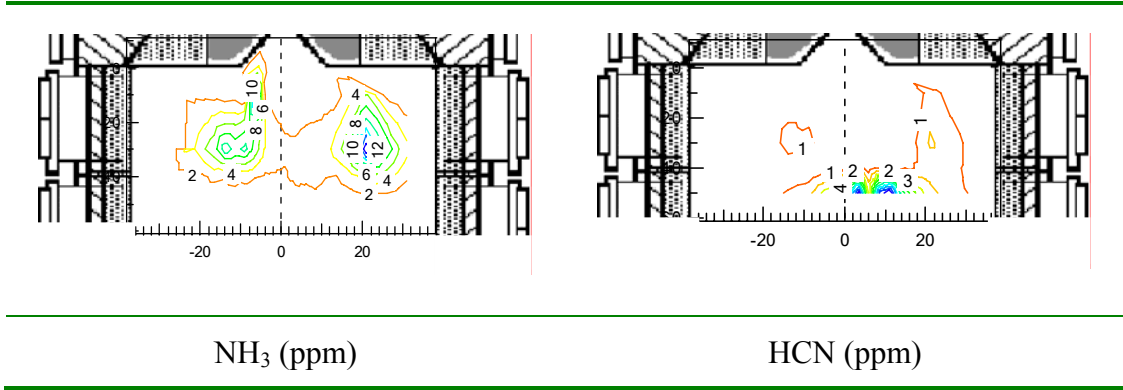


Figure 6.22 NH₃ and HCN maps from Test 70SD30P. The unit of radial distance from the centerline is cm.

As mentioned in Section 6.2.1, flames in the BFR presumably consist dispersed particle laden (fuel-rich) eddies separated by fuel-lean eddies in the near burner region. The averaging effect is inevitable during gas-sampling in this region, especially for the NO_x precursors, HCN and NH₃, which only exist within the fuel-rich eddies. Therefore, results showed from Figure 6.17 to Figure 6.22 are not the actual species concentrations in the local fuel-rich eddies. In general, the amount of NH₃/HCN in fuel-rich eddies (see Appendix I for derivation) can be determined from

$$X_{i, \text{fuel-rich eddy}} = X_{i, \text{measured}} \frac{X_{O_2, \text{fuel-lean eddy}}}{X_{O_2, \text{fuel-lean eddy}} - X_{O_2, \text{measured}}} \quad 6.3$$

where x represents mole fraction and i represents any species that exists only under fuel-rich conditions and here it represents NH₃ or HCN. For example, if the fuel-lean eddies are pure air (numerator and first term in denominator are 0.21) and 18% O₂ is measured (last term in denominator) with 10 ppm NH₃ (first factor on right side), the indicated concentration of NH₃ in the fuel-rich eddy is 70 ppm. The modified HCN and

NH₃ profiles assuming that the fuel-lean eddies are pure air for the Blind Canyon, straw and their cofiring tests are shown in Figure 6.23. However, this is the lowest possible NH₃ concentration in the eddy since, in general, the fuel-lean eddies will contain less than 21% oxygen, which will result in higher indicated estimates of ammonia in the fuel-rich eddies. This indicates that the amounts of HCN and NH₃ in the fuel-rich eddies in the current experiments could be higher than the average data suggest. While this procedure estimates a lower bound for the NH₃ and HCN concentrations in the fuel-rich eddies, there is no finite estimate of an upper bound.

A summary of the NH₃ and HCN maps of all the cases leads to several conclusions as follows:

1. HCN and NH₃ could be measured in the transient fuel-rich eddies under the overall fuel-lean tests with the intrusive data collection system. CO is much more stable than HCN and NH₃ through the flame front. The light nitrogen species exhibit the same general trend as that of CO. This confirms the existence of HCN or NH₃ in most cases, though several cases included one species below detectable levels.
2. NH₃ is dominant fuel-NO_x intermediate detected during straw firing, while HCN is detected in coal flames and blended flames cofiring with coal mass fractions of at least 50%.

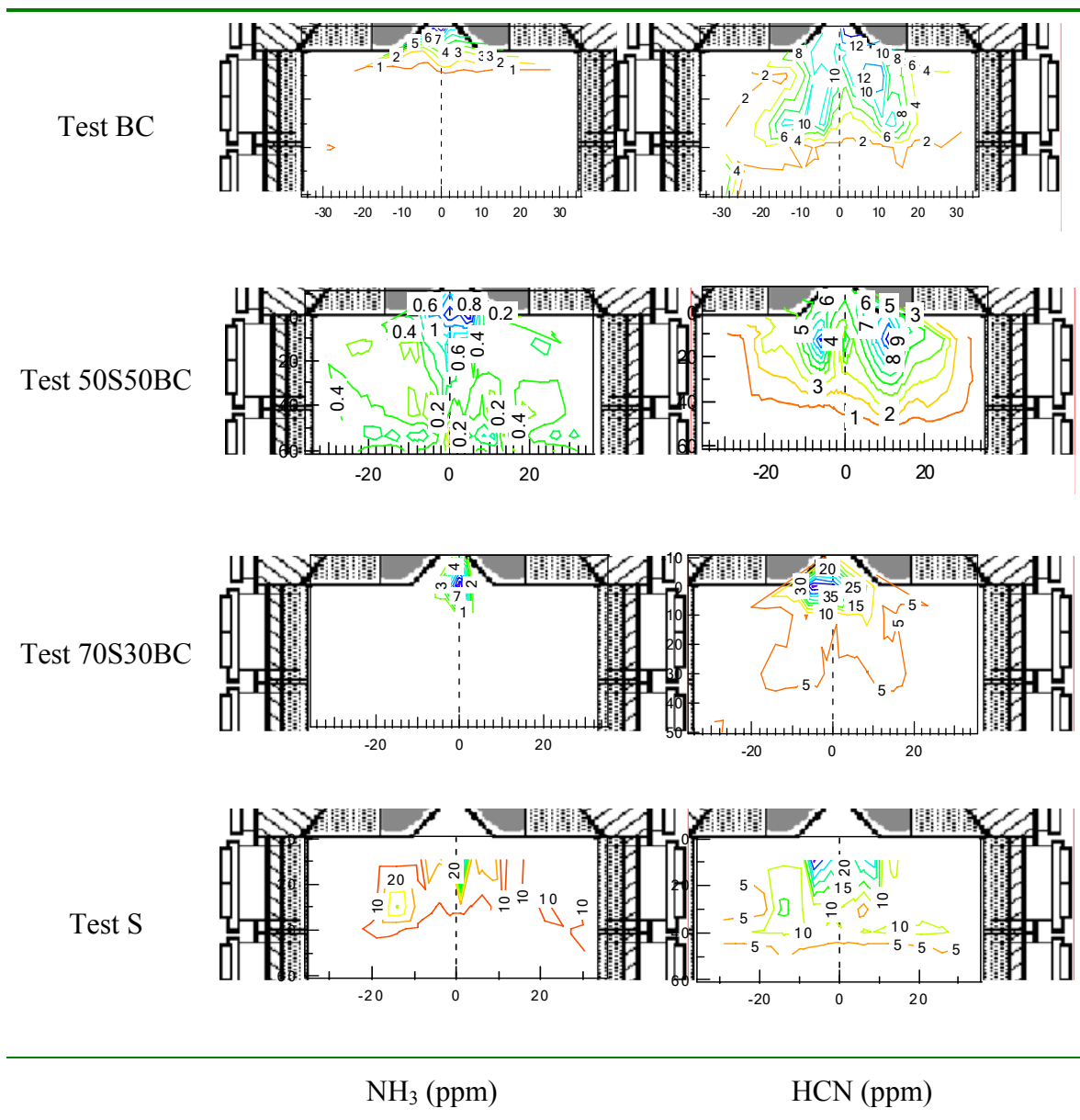


Figure 6.23 The modified HCN and NH₃ spatial profiles from the tests of Blind canyon, straw and their cofiring mixtures based on Equation 6.4, with the assumption that the fuel-lean eddies are pure air

6.5.2 Analysis of NO emission data

This section discusses the NO emission data from each combustion test and the impact of cofiring biomass on total NO generation.

NO maps from all the tests appear in Figure 6.24. They all have similar pattern: the high NO concentrations occur in the combustion region, and in the reacted-gas region NO demonstrates a relatively flat profile.

Test S data exhibit greater NO reduction variation (a NO reduction of nearly 200 ppm) than any other fuel or blend in the reacted gas region. A careful review of the CO profiles for the straw case (Figure 6.14, for example) indicates that finite CO concentrations persist much further for straw in the axial direction than for any other fuel. Unlike sawdust, straw contains highly heterogeneous components. Specially, straw knees, which are the joints in the stalk of the plant, are far denser than the bulk of the fuel. Straw knees produce large and relatively dense char particles that require much longer to burnout than does most other parts of similar particle size. Such residual char particles could be the origin of both the CO and the extended NO chemistry observed in the data. These data are not sufficiently definitive to establish this point, and doing so requires solid sampling, but this is a plausible explanation. This issue will be investigated in some detail in a continuation of this work being conducted by another investigator (Damstedt et al. 2005).

Since the operating stoichiometries are not the same among all the tests. NO emissions from Test BC and other tests are compared on a 3% excess O₂ basis. The normalized NO emission, $Y_{NO,3\%O_2}$, is calculated from

$$Y_{NO,3\%O_2} (ppm) = \bar{Y}_{NO} \frac{21 - 3}{21 - \bar{Y}_{O_2}} \quad 6.4$$

where \bar{Y}_{NO} and \bar{Y}_{O_2} are the respective average of NO and O₂ mole fractions across the reacted-gas region.

Changes in stoichiometry represent different degrees of dilution of flue gas components in addition to changes in combustion parameters such as flame temperature and radical concentrations. Normalizing the data to a 3% oxygen basis removes the dilution effects in the data, allowing the combustion impacts to be more clearly evident.

For the examination of the impact on NO emission of cofiring biomass, NO emissions on an energy basis can be determined through

$$Y'_{NO} = \frac{N_{NO} MW_{NO}}{\sum M_i H_i} \quad 6.5$$

where N_{NO} is the molar flux of NO (mol/hr) at the exhaust, as calculated from

$$N_{NO} = [(\sum M_i + M_{air}) / MW_{mixture}] y_{NO,exhaust} \quad 6.6$$

where the symbols are defined as follows.

M_i and M_{air} : the feed rates (kg/hr) of fuel i and air, respectively;

H_i : the lower heating value (as received; MJ/kg) of fuel i ;

$MW_{mixture}$ and MW_{NO} : the molecular weight of exhaust gas mixture (assumed to be 29 g/mol) and NO, respectively.

$y_{NO,exhaust}$: the measured exhaust NO volume fractions;

Y'_{NO} : the amount of NO produced per unit energy of fuel, a more meaningful number from an environmental performance standpoint than the amount of NO produced per unit of flue gas produced, especially when fuel heating values vary as widely as is the case between coal and biomass.

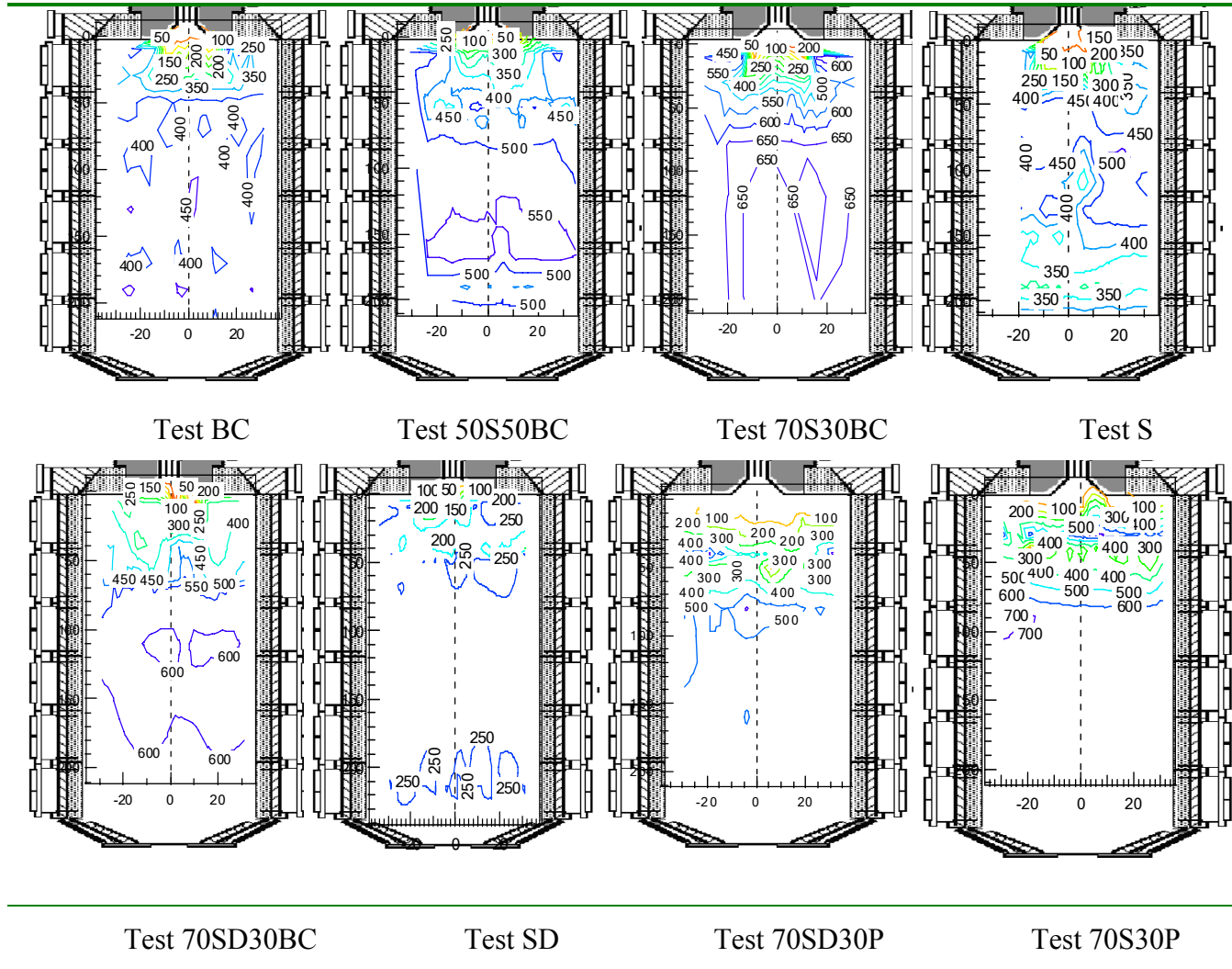


Figure 6.24 Comparison of axisymmetric NO maps (unit: ppm).

Another term introduced during analysis of NO emissions based on a fuel-N input basis is the fuel-N yield, defined as

$$Y''_{NO} = \frac{Y'_{NO}}{\sum M_i x_{N,i}} \quad 6.7$$

where $x_{N,i}$ is the nitrogen mass fraction of fuel i . This parameter represents the amount of NO produced per unit nitrogen in the fuel. Assuming all NO is generated from fuel nitrogen, which is approximately correct for essentially all nitrogen-containing solid fuels, larger values of this parameter indicate greater fuel nitrogen conversion normalized by the heating value of the fuel.

The normalized emissions of all the tests are tabulated in Table 6.1. The table shows that Pittsburgh #8 has the highest value of $Y_{NO,3\%O_2}$ (668 ppm), higher than straw (561 ppm), which is higher than that of Blind Canyon (504 ppm). Sawdust has the lowest fuel-N content (0.35%, wt, daf) and shows the lowest NO emissions (257 ppm). Cofiring biomass with coal does not necessarily reduce NO emissions on the 3% excess O_2 basis (the basis sometimes used by EPA, among others, for regulations). Two straw cofiring cases, Test 70S30BC and Test 70S30P, show a high $Y_{NO,3\%O_2}$ (665 and 661 ppm, respectively) close to that of pure Pittsburgh #8. Cofiring sawdust with Blind Canyon also increases NO emission compared to that from the pure coal test. Only Test 50S50BC and Test 70SD30P demonstrate a reduction in NO emission compared to the respective pure coal tests.

Table 6.1 NO emissions in the reacted-gas region during current project

Test ID	$Y_{NO,3\%O_2}$ (ppm)	Y'_{NO} (10^{-2} kg/MJ)	Y''_{NO} (10^{-2} kgNO/MJ/kgN)
S	561	4.07	2.47
70S30BC	664	3.89	1.91
70S30P	661	4.16	1.97
50S50BC	530	2.79	1.32
SD	257	1.47	2.26
70SD70P	461	2.51	1.72
70SD30BC	593	3.13	2.27
P	668	4.44	2.52
BC	504	3.32	2.04

Resulting NO emissions on an energy basis, as included in Table 6.1, indicate that sawdust is once again the lowest NO emitter (1.47×10^{-2} kg/MJ), with its Y'_{NO} less than one half that of other fuels, and its cofiring cases with Pittsburgh #8 drops the emission level by nearly 50%, and a decrease of 18% was achieved when cofiring with Blind Canyon. Because of the relatively high fuel-N content, straw shows a high NO emission close to Pittsburgh #8 and higher than Blind Canyon, and its cofiring cases studied can only achieve a reduction of around 25% (Test 50S50BC) at most. In the higher mass fraction cofiring test with Blind Canyon, NO emission (3.89×10^{-2} kg/MJ, Test 70S30BC) is even higher than the pure coal test (3.32×10^{-2} kg/MJ).

With respect to yield (Y''_{NO}), the pure biomass tests have the highest NO yields, followed by the pure coal tests, and cofiring can effectively reduce NO emissions. For example, Test 50S50BC has a nearly 40% reduction of NO yields compared to that of Test S on this basis. All cofiring tests were found have lower Y''_{NO} values than their

respective pure fuels tests, and this reveals that cofiring can be a potentially feasible method to reduce NO yields on bases of both energy and fuel-N input.

These data show the complexity associated with NO emissions. For example, sawdust produced about half as much NO as the next lowest pure-fuel NO emitter as measured by concentration in the flue gas normalized for dilution. If normalized by fuel heating value, sawdust is still the lowest emitter. When NO per unit energy per unit fuel nitrogen content is considered, sawdust is among the highest emitters of NO. The biomass used have higher nitrogen conversion efficiencies to NO than for HCN intermediates (coal) regardless whether the actual NO concentrations are relatively high (straw) or low (sawdust). However, fuel properties alone don't account for all of the variation, as indicated by the high NO and conversion efficiency of Pittsburgh #8 coal, presumably because of high temperatures associated with higher heating value and equivalence ratio compared to most other tests.

More insight into NO formation arises by comparing measured NO concentrations during cofiring to the interpolated value based on measured results from pure coal and biomass that comprise the cofired fuel. Results are plotted on a parity diagram, that is, a plot of the interpolated value vs. the measured value. This technique requires three experimental tests, one each for the pure fuels and one of a blend, to establish a single data point. Departures from the diagonal line, where interpolated and measured values are equal, indicate some form of non-linear interaction of the fuels in the combustion environment.

The interpolated NO emissions from cofiring tests could be determined through the summation of mass-weighted data from the respective pure fuels

$$(Y_{NO,3\%O_2})_{cofiring} = \sum \frac{(Y_{NO,3\%O_2})_{i,pure}}{M_{i,pure}} M_{i,cofiring} \quad 6.8$$

where $M_{i,pure}$ and $M_{i,cofiring}$ are the feed rates of same fuel during its single firing and cofiring tests, respectively. The relation between the interpolated and measured NO emission on a 3% excess O_2 basis is plotted in Figure 6.25. Among the cofiring cases, Test 70S30BC has the best interpolation, with the resultant point on the diagonal. Other cofiring tests show deviations of different levels: Test 50S50BC has the highest positive difference of about 28%, with Test 70SD30P 20%, Test 70S30P 14.5%, and Test 70SD3BC a negative deviation of -22%. This is opposed to the previous results from a non-swirling burner (Baxter 2002), as shown in Figure 6.26, which suggests that the total NO emission from the cofiring case can be interpolated from the NO emission data from the respective pure fuel tests. The complexities of aerodynamics, stoichiometric variations, and temperature variations inherent in the swirl-stabilized results combine to produce results that differ from interpolations of pure fuel behavior. If these complexities are eliminated, as in the previous data, and only parallel flow reactions are considered, NO chemistry is seen to be primarily a function of the pure fuel behavior. However, these latter tests are much better representations of commercial boiler behavior than are the former tests with idealized flow, stoichiometry, and temperature trends.

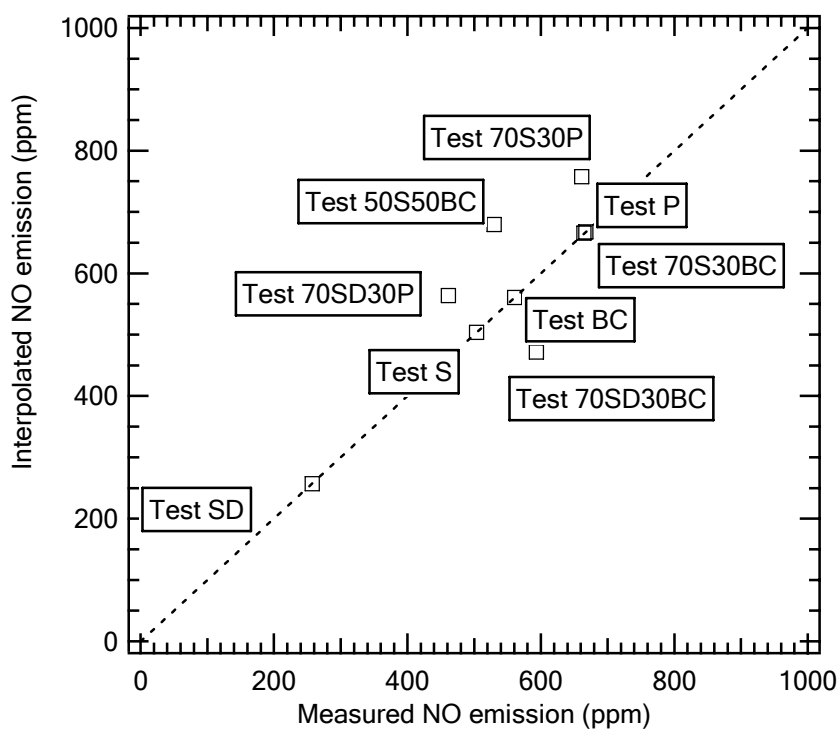


Figure 6.25 The relation between the measured and the interpolated NO emissions (mole fraction on a 3% excess O₂ basis) in the present project.

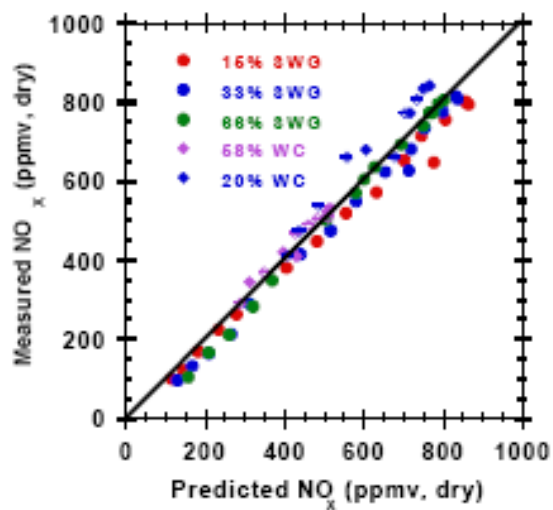


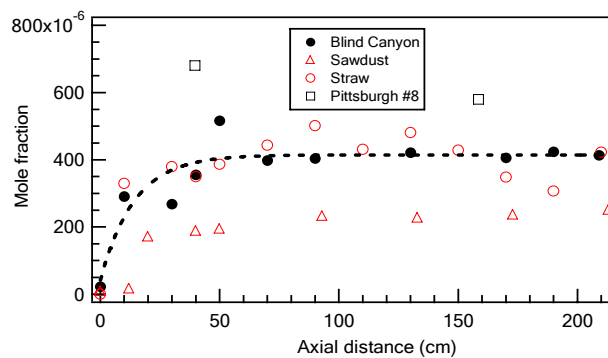
Figure 6.26 The relation between the measured and the interpolated NO emissions in a non-swirling flow burner. (Baxter 2002a)

During pulverized fuel, swirling flow combustion in the BFR, NO formation is dominated by gas-phase reactions. After the release from the condensed phase, the gas species and their reactions are independent of the parent fuels. Therefore, the deviation of the cofiring data from the diagonal in Figure 6.25 maybe caused by the complex temperature field and highly turbulent flows. The reverse flow predicted with modeling shows all the tests are of similar flow patterns, but the difference in the IRZ size is obvious among the tests. Other details such as changes in local instantaneous velocity can have a tremendous impact on the combustion stoichiometry and instantaneous temperature, resulting in the complexity of gas-phase reactions. Thus, the deviation is attributed to the turbulent, complex flow and temperature fields in the swirling region, but not necessarily the solid fuel interactions. A further analysis of the 1-D profiles is necessary to clarify NO formation in the combustion region, as discussed in the next section.

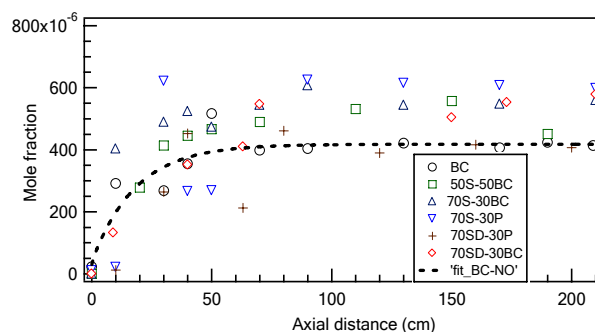
6.5.3 1-D profiles of NO

NO normalized mole fractions from each test demonstrate a generally monotonic increase with increasing axial position within the first 50 cm, as seen in Figure 6.27. From 10 to 20 cm, NO from both biomass tests increases following the sharp increase of CO₂ (Figure 6.14 as the pure fuel tests data, and Figure 6.16 as the cofiring data), which is caused by the larger amount of volatile off-gas combustion, as discussed earlier. Results from pure fuel tests show a relatively flat pattern in the reacted-gas region.

Sawdust has much lower nitrogen content (0.35%, wt, daf) than straw (0.91%, wt, daf), and their carbon contents are similar. Therefore, Test SD has a much lower NO generation but similar CO₂ formation.



(a)



(b)

Figure 6.27 NO 1-D profiles from pure fuel tests (a) and cofiring tests (b) (The lines show the trends of normalized results of Test BC along the reactor axis)

The nitrogen species data collected, together with CO, CO₂, and O₂ spatial profiles, consistently reveal the characteristics (as summarized in Section 6.5.5) in biomass swirl-stabilized flames. These data provide valuable validation criteria for future comprehensive low-grade fuel combustion models.

6.5.4 Kinetic evidence on the fate of NO_x intermediates

Based on currently available theory and computing capability, it is not feasible to develop a comprehensive swirling flow solid-fuel combustion model containing both detailed fluid mechanics and elementary reaction mechanisms. The primary complicating factor is chemical kinetics and the limitations in expressing such kinetics are both

theoretical and computational. Non-premixed models reasonably approximate rapidly reacting systems, but they are not applicable for reactions with time constants that approximate or are slower than the turbulence time scales. Several important species are involved in such reactions, including NO_x , CO, and SO_2 , and soot. CFD models usually do not include full chemical kinetics as is the case in FLUENTTM. As described in Appendix G, the fuel- NO_x model built in FLUENTTM is not able to reveal the difference in the fate of the important intermediates, NH_3 and HCN.

In this section, detailed kinetics calculations with simplified flow dynamics illustrate the potential impact of different intermediates (HCN and NH_3) on NO formation. The intention of the detailed modeling work is to develop quantitative descriptions of relative reactivities that are useful in interpreting the measured data. Specifically, the relative thermal stabilities and chemical reaction rates of HCN and NH_3 in combustion environments similar to those in the current investigation was investigated using detailed chemical kinetics and, despite the absence of turbulent fluctuations in the calculations, qualitatively indicate which species are most stable.

CHEMKIN is a collection of data bases, programs and subroutine libraries written in text files and in Fortran code that is widely used in such investigations. It incorporates complex chemical kinetics into simulations of reacting flows. As a powerful set of software tools, CHEMKIN facilitates the formation, solution, and interpretation of problems involving gas-phase and heterogeneous (gas-surface) chemical kinetics, equilibrium, and transport properties.

In this project, CHEMKIN was used to analyze the fate of the NO_x intermediates, HCN and NH_3 , at different temperatures representing both the fuel-rich region and the

flame front in the BFR. Two detailed mechanisms are considered in the calculations: Kilpinen 97 (Kilpinen 1997) and GRI-Mech 3.0 (Smith et al. 2000). The Kilpinen 97 mechanism has been largely validated by the biomass gasification data mentioned earlier (Coda Zabetta and Kilpinen 2001a; Coda Zabetta et al. 2000; Coda Zabetta 2002a; Coda Zabetta and Kilpinen 2001b; Kilpinen et al. 1999). The GRI-Mech 3.0 is the most recent and most comprehensive version of the mechanisms developed at the Gas Research Institute.

The detailed kinetic mechanisms do not include the effects of turbulence on the reaction, which is expected to be significant in this mixing-limited combustion application. We do not anticipate quantitatively accurate predictions from CHEMKIN when applied to the complex flows in the BFR. However, results from CHEMKIN calculations are able to explain qualitative observations in the data based on best-available mechanisms for gas-phase NO_x formation. Specifically, we anticipate that the CHEMKIN results will help establish whether the form of nitrogen evolved from the fuel substantially impacts either nitrogen intermediates or ultimate NO_x concentrations.

In the BFR, HCN and NH_3 are resident in transient fuel-rich eddies and oxidized within the flame front. In the former case, HCN and NH_3 exist with carbon monoxide, steam, and other relatively stable species, and are only slightly oxidized because of the scarcity of O_2 . Reactions involving HCN and NH_3 include their thermal decomposition. The flame front is rich in radicals and produces the highest temperature. Therefore, oxidation reactions are more significant for the intermediates in this region. One of the purposes of kinetic calculations is to compare the stability of HCN and NH_3 under conditions simulating both the fuel-rich region and the flame front. The other intention is

to analyze the difference in their conversion to NO in the flame front. The latter can be achieved through analysis of total fixed nitrogen (TFN), which is the summation of all nitrogenous species except N₂.

The assumed detailed initial gas mixture compositions based on elemental composition of straw appear in Table 6.2. For a comparison of the thermal stability, the gas species mixture is assumed to include equal amounts (mole fractions) of HCN and NH₃, C₂H₂, and CO, and similar CO₂ and H₂O contents, with the balance of the mass as N₂, (Case 1). With respect to the stability of HCN and NH₃ in the flame front, OH radicals are introduced to represent radicals penetrating the flame, and CO and C₂H₂ represent the devolatilization off-gases, with a supply of O₂. As for the comparison of conversion of HCN and NH₃ to TFN (total fixed nitrogen), either HCN or NH₃ is defined as the only NO_x intermediate in the gas mixture under flame front conditions (Case 2 and Case 3). The calculation was carried out with temperatures ranging from 1600 K to 2400 K.

Table 6.2 Compositions of the initial gas mixtures used in the kinetic simulations

	Case 1	Case 2	Case 3
	Fuel-rich core	Flame front	Flame front
HCN	8.35e-4	8.35e-4	0
NH ₃	8.35e-4	0	8.35e-4
H ₂ O	0.15	0.15	0.15
OH	0	0.01	0.01
CO ₂	0.15	0.15	0.15
C ₂ H ₂	1.00e-3	0.10	0.10
CO	1.00e-3	1.84e-3	1.84e-3
O ₂	0	1.08e-3	1.08e-3
N ₂		Balance	

The calculation results with the Kilpinen 97 and GRI-Mech mechanism are almost the same for each case considered. Therefore, results from the simulations with the Kilpinen 97 mechanism are discussed here. The GRI-Mech 3.0 calculation results are listed in Appendix J.

The comparison of the thermal stability of HCN and NH_3 in the fuel-rich region is illustrated in Figure 6.28. Results from the detailed mechanism show that the decomposition rate of both species increases with increasing temperature, as indicated by time needed to consume the NO intermediates. At 1600 K, there was almost no change in the NH_3 and HCN concentrations during the first 0.05 s. With the process continuing, the amount of HCN begins dropping and NH_3 remains essentially unreacted through the remaining time examined (up to one second). At 1800 K, both species concentrations display a decrease after a reaction time of 0.01 seconds, and reach 1 ppm within 0.5 s. At 2400K, the time required to achieve same reduction of species concentration is about 2 ms. The logarithmic scales somewhat underemphasizes the significant difference in thermal stability at the lower temperatures. These calculations show that NH_3 has greater thermal stability than HCN in the temperature range 1600-2000K, with the difference increasing as T decreases.

Under temperatures studied, HCN shows lower chemical reactivity (reacts more slowly) than NH_3 throughout the flame front region, with the results from Case 2 and Case 3 shown in Figure 6.29. Both species react much faster compared to reducing conditions at the same temperatures. The consumption rates of both species increase with increasing operating temperatures.

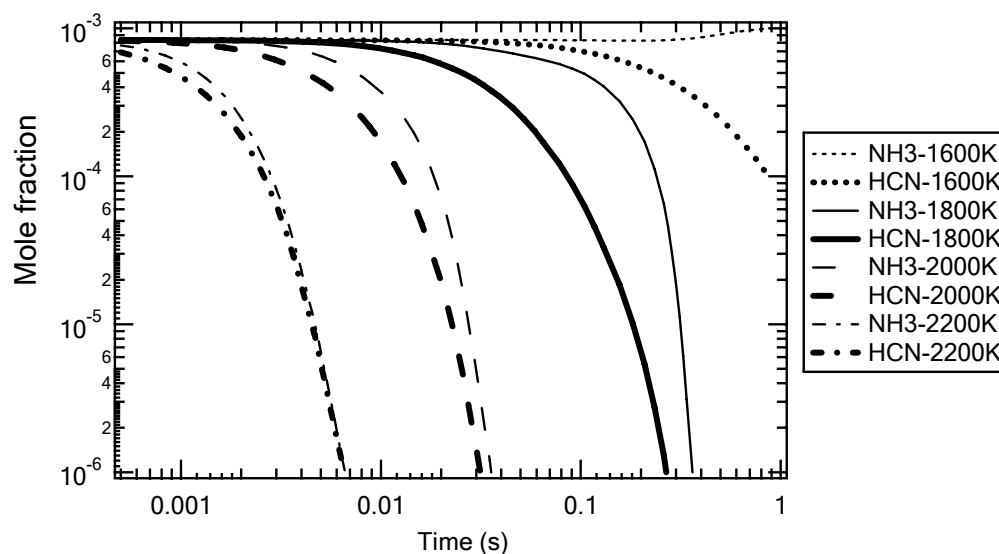


Figure 6.28 Comparison the thermal stability of HCN and NH₃ in the fuel-rich region with the Kilpinen 97 mechanism.

The NO_x intermediate maps discussed earlier (Section 6.5.1) are consistent with the calculation results in Case 1. Because most biomass fuel-nitrogen resides in the form of acyclic compounds like amine or amide derivatives, NH₃ is the dominant intermediate found in the combustion region during pure biomass tests and most cofiring cases with a biomass mass fraction of 70%. During these tests, more NH₃ than HCN is released during devolatilization in the fuel-rich region, and because of the scarcity of oxygen, the thermal decomposition of the intermediates should prevail. NH₃ is more thermally stable than HCN at temperatures between 1600 K and 2000 K (which is typical for low-grade fuel flames), thus it should be found as the dominant NO_x intermediate in the fuel-rich core. Furthermore, thermal decomposition of NH₃ is less effective than HCN, leading to higher NH₃ concentrations than HCN concentrations as the combustion gases enter the flame front.

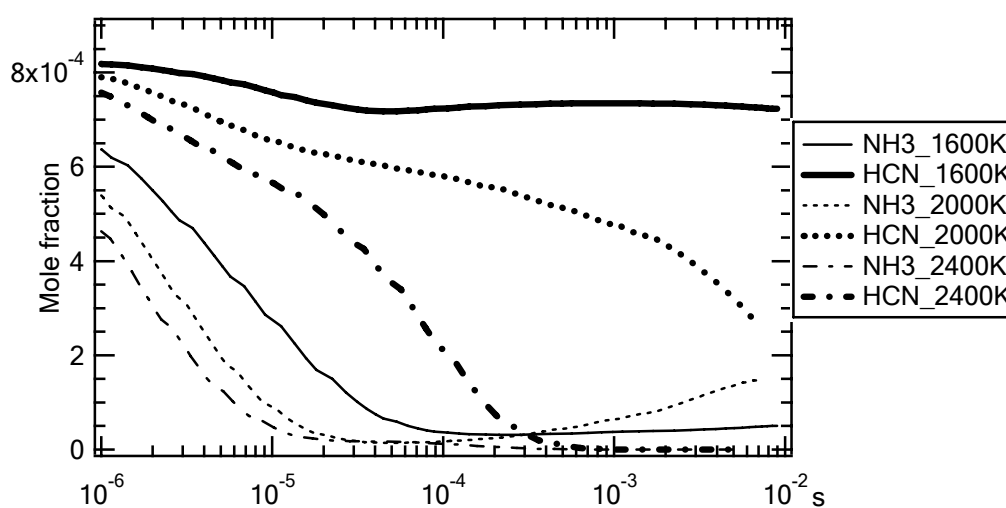


Figure 6.29 Comparison the chemical stability of HCN (Case 2) and NH_3 (Case 3) in the flame front with the Kilpinen 97 mechanism.

At the flame front, both intermediates are consumed quickly through oxidation. NH_3 reacts faster to form NO than does HCN at short reaction times (up to 0.1 ms). At long times, both species approach their equilibrium NO concentrations, which are independent of initial composition. This indicates that NO formation in thin flames is more significant for NH_3 than HCN, though both react to form NO.

The NO formation potential in the flame fronts of HCN and NH_3 can be compared through monitoring respective TFN (the sum of all the nitrogen species but not N_2) and NO profiles from Case 2 and Case 3. The calculation results appear in Figure 6.30. HCN and NH_3 have the same conversion to TFN under temperatures studied, and the conversion increases with temperature. Since NH_3 is more reactive than HCN, more NO is generated from NH_3 during the initial stage. Below 2400K, the profiles of TFN generally show a flat pattern, indicating that all the intermediates were converted into NO.

Mole fractions of both TFN and NO show a slightly decrease with longer reaction time, and this is because more TFN is converted into N_2 .

From these kinetics calculations, NH_3 is found more thermally stable and chemically reactive than HCN, and NH_3 more rapidly forms NO in the early stages of reaction. These theoretical results are consistent with the observations in Table 6.1, where NH_3 -forming fuels exhibit relatively high fuel nitrogen conversion efficiencies to NO relative to most other fuels.

6.5.5 Summary

The chapter is summarized as follows:

1. Low-grade fuel combustion in the swirl-stabilized burner

The BFR capably operates during both dedicated biomass firing and cofiring biomass with coal in addition to pure coal tests for which it was previously used. Under the conditions studied, all low-grade fuel combustion in the swirling flow burner develops a stabilized combustion zone near the inlet followed by a relatively flat reacted-gas zone. Under overall fuel-lean conditions, intrusive measurements reveal the existence of transient fuel-rich eddies. The existence of an instantaneous fuel-rich region is evident by the detection of HCN/ NH_3 and high amounts of CO in the swirling flow region even though the average O_2 concentration is greater than zero. Notably, no region exists in any test in which average O_2 concentrations are zero. The data sets collected are generally repeatable and consistent, and provide valuable validation criteria for future development of comprehensive combustion models.

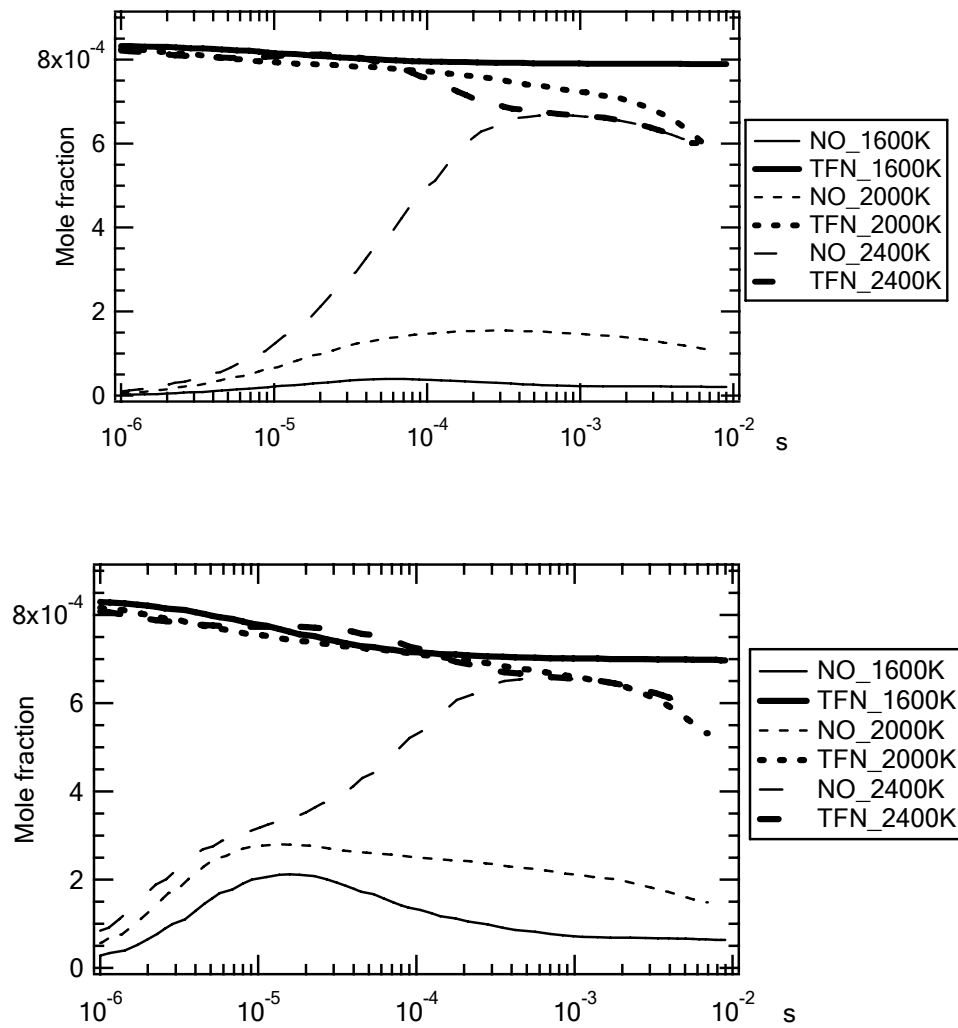


Figure 6.30 Calculated profiles of TFN and NO from cases where only one type of NO_x intermediate exists in the initial mixture, with lines representing results from HCN mixtures (Case 2) and markers denoting NH_3 blends (Case 3) with the Kilpinen 97 mechanism.

2. Biomass firing and cofiring compared to coal combustion in swirling flows

CFD Predictions show that there are no dramatic qualitative changes in flow patterns in the swirling flow during biomass tests compared to coal test, though details differ. All flows show centerline and corner recirculation zones that stabilize the flame

near the burner outlet. However, biomass combustion in swirling flows has an expanded combustion region resulting from more particle penetration and high volatile yield. The small and dry biomass particles (compared to commercial fuels) penetrate the flame further into the reactor to complete devolatilization and oxidation. High-volatile yields contribute to the larger and more intense fuel-rich (CO-laden) regions.

3. NO formation from the cofiring cases

In the gas species 1-D and axisymmetric profiles, NO follows a similar pattern to that of CO₂, indicating that NO formation is more mixing limited than kinetically controlled under the conditions studied. Combustion of sawdust shows significant lower NO production on an energy basis primarily because of its low nitrogen content.

Biomass and coal have different stable NO_x precursors. HCN is the prevailing fuel-NO_x intermediate in coal flames, and NH₃ is predominant in the straw and possibly sawdust flames. The form of nitrogen impacts NO formation mechanisms and emission concentration. Biomass generates more NH₃ and less HCN than coal, and the dominance of NH₃ in biomass combustion increases the amount of fuel-N converted to NO under swirling flow conditions. Kinetic calculations based on CHEMKIN show that NH₃ is more thermally stable than HCN in the combustion region and more reactive within the flame fronts. Both HCN and NH₃ show similar conversion efficiency to NO in the reacted-gas region.

Chapter 7 Summary and Conclusion

Brigham Young University's Burner Flow Reactor (BFR) capably produces swirl-stabilized flames when cofired with biomass and coal that include the complexity of commercial systems. This capability required rebuilding the ceramic liner and replacing the fuel handling and computer-control gas analysis systems. This pilot-scale facility provides an aerodynamic and thermal environment representative of the near-burner region of a commercial combustor.

This project enhances the understanding of biomass combustion performance in the near-burner region, especially flame structure, major species profiles and NO formation. Spatial concentration profiles of seven gas species, CO, CO₂, O₂, NO, HCN, and NH₃, were collected with intrusive sampling methods using two commercial state-of-the-art analyzers and a specially designed gas sampling probe. Combustion tests included nine separate fuels or fuel blends. Spatial profiles of major species from biomass cofiring provide detailed indications of flame structure and dynamics. All the tests were conducted in overall fuel-lean conditions.

The experiments provide a database that defines flame structure, chemistry, and aerodynamics for a wide variety of coal and biomass fuels and blends. High- and moderate-sulfur coals (Pittsburg #8 and Blind Canyon) and herbaceous and woody

biomass (straw and sawdust) and blends of these fuels form the suite of fuels and blends tested. Advanced instrumentation and other engineering improvements increase experimental efficiency, reducing the time necessary for the completion of one case from several months to less than three weeks.

CFD modeling with commercial software, FLUENTTM, predicts velocity and temperature information. Flow patterns were predicted and analyzed under both cold-flow and hot-flow conditions in the BFR. A 3-D CFD model simulates the swirl-generator cold-flow exit velocities. Experimental velocity data under non-reacting conditions collected in the project generally follow the trends from CFD predictions. The predictions immediately following the swirl-generator were adopted to define the inlet for the axisymmetric combustion model. Reacting flow data collected previously in the same reactor compare less favorably with predictions with possible inconsistencies in both.

In addition to the axisymmetric species spatial profiles (maps) and CFD predictions, two data analysis methods, stoichiometric ratio maps and 1-D normalized mole fractions, quantify flame structure, major species profiles, and flow dynamics.

Analysis of NO formation is provided through comparison of CO, NO, NH₃, and HCN profiles, supplemented with CHEMKIN calculations.

The major conclusions drawn from this project include:

1. Low-grade fuel combustion in the swirl-stabilized burner

The BFR capably operates during both dedicated biomass firing and cofiring biomass with coal in addition to pure coal tests for which it was previously used. Under the conditions studied, all low-grade fuel combustion in the swirling flow burner

develops a stabilized combustion zone near the inlet followed by a relatively flat reacted-gas zone. Under overall fuel-lean conditions, intrusive measurements reveal the existence of transient fuel-rich eddies. The existence of an instantaneous fuel-rich region is evident by the detection of HCN/NH₃ and high amounts of CO in the swirling flow region even though the average O₂ concentration is greater than zero. Notably, no region exists in any test in which average O₂ concentrations are zero. The data sets collected are generally repeatable and consistent, and provide excellent validation criteria for future development of comprehensive combustion models.

2. CFD simulation of low-grade-fuel combustion

Grid-independent, high-order modeling approaches provide reasonable predictions of gas-phase velocity and temperature and have limitations in predicting species. With a proper modeling strategy, the results verify the existence of the reverse flow region close to the inlet under both cold-flow and hot-flow operating conditions. In the wall-confinement region (in the water-cooled quarl), the flow can be predicted with little error. In the swirling-flow, fully developed region, the small shift of the flow axis from the reactor geometric axis can't be predicted with an axisymmetric code or, in the absence of any asymmetric boundary or inlet conditions, by a fully 3-D code. CFD simulation of low-grade fuel combustion

3. Biomass firing and cofiring compared to coal combustion in swirling flows

Predictions show that there are no dramatic qualitative changes in flow patterns in the swirling flow during biomass tests compared to coal test, though details differ. All flows show centerline and corner recirculation zones that stabilize the flame near the burner outlet. However, biomass combustion in swirling flows has an expanded

combustion region resulting from more particle penetration and high volatile yield. The small and dry biomass particles (compared to commercial fuels) penetrate the flame further into reactor to complete devolatilization and oxidation. High-volatile yields contribute to the larger and more intense fuel-rich (CO-laden) regions.

4. NO formation from the cofiring cases

In the gas species 1-D and axisymmetric profiles, NO follows a similar pattern to that of CO₂, indicating that NO formation is more mixing limited than kinetically controlled under the conditions studied. Combustion of sawdust shows significant lower NO production on an energy basis primarily because of its low nitrogen content.

Biomass and coal have different stable NO_x precursors. HCN is the prevailing fuel-NO_x intermediate in coal flames, and NH₃ is predominant in the straw and possibly sawdust flames. The form of nitrogen impacts NO formation mechanisms and emission concentration. Biomass generates more NH₃ and less HCN than coal, and the dominance of NH₃ in biomass combustion increases the amount of fuel-N converted to NO under swirling flow conditions. Kinetic calculations show that NH₃ is more thermally stable than HCN in the combustion region and more reactive within the flame fronts. Both HCN and NH₃ show similar conversion efficiency to NO in the reacted-gas region.

Chapter 8 Research Limitation and Recommendations

There are several limitations and recommendations to the scope of this project, as summarized below.

1. Combustion tests were conducted only under overall fuel-lean (oxidizing) conditions, mainly because of safety considerations associated with CO generation under reducing conditions. Even under overall oxidizing conditions, there are locally reducing regions in the flow important to this investigation. In the future refurbishment of the reactor, better insulation techniques are necessary to seal the connection between the sections. A better monitoring of the operational fuel feed rates is helpful to describe the reactor operating conditions and minimize the inconsistency during the data collection.
2. While significant theoretical analysis of the experimental measurements was completed, including comprehensive simulations of the reacting flow environment, the scope of this project does not include the formulation of an alternate NO_x model suitable for incorporation into a turbulent reacting flow code. In addition, the turbulence/chemistry was modeled with only one mixture fraction variable, which assumes the fuel-off-gas volatiles have the same composition as the parent fuel. Because this method neglects the fact the volatiles are rich in hydrogen and oxygen, the predicted gas species concentrations will have some error. Furthermore, the fuel- NO_x model built into the modeling tool is too simplified to characterize the complicated nature of NO_x

chemistry in the near-burner region. Detailed or general mechanisms need to be included in the comprehensive modeling, though computational expense will increase significantly.

3. The experimental techniques all involve intrusive probes. Such probes alter the flow fields in which they were used and potentially bias the measurements. This potential could be especially high in elliptical (recirculating) flows, examples of which were included in this investigation. Alternative, mostly laser-based techniques exist that could be used to make some of these measurements and avoid the intrusive nature of probes, but many of these alternate techniques produce arguably less accurate/precise results than the intrusive measurements and all of them require equipment, time, and funding beyond the scope of this project. Development of accurate diagnostics for large particle laden flames represents a major research challenge.

4. Commercial biomass cofiring systems nearly all involve multiple burners in much larger scale facilities than used here. The facilities used here represent a good compromise between industrial relevance and careful/affordable operation and control. However, potentially important effects in commercial systems were recognized not to be simulated in these experiments, including burner-burner interactions, t-fired burner firing modes, radiative length scales, flame orientation relative to quality, and overall geometry.

5. Complete combustion information during cofiring tests should include gas-phase, solid-phase, temperature and velocity profiles. However, particle collection and measurement of the hot-flow velocity was beyond the scope of this project. The temperature profiles are extremely challenging to quantify because the point-measurement methods suitable to the pilot-scale reactor flame temperature are not established. However, velocity and temperature measurements with existing technologies

and instruments such as LDV and pyrometer should be applied to supplement the gas-phase species mole fraction under the same conditions, so as to provide comprehensive data for future modeling.

References

- Abbas, T., Costa, M., Costen, P., Godoy, S., Lockwood, F. C., Ou, J. J., Romomillares, C., and Zhou, J. (1994a). "NO_x Formation and Reduction-Mechanisms in Pulverized Coal Flames." *Fuel*, 73(9), 1423-1436.
- Abbas, T., Costen, P., Kandamby, N. H., Lockwood, F. C., and Ou, J. J. (1994b). "The Influence of Burner Injection Mode on Pulverized Coal and Biomass Cofired Flames." *Combustion and Flame*, 99(3-4), 617-625.
- Aho, M. J., Hamalainen, J. P., and Tummavuori, J. L. (1993). "Importance of Solid Fuel Properties to Nitrogen Oxide Formation through HCN and NH₃ in Small Particle combustion." *Combustion and Flame*, 95L, 22-30.
- Albrecht, H.-E., Rostock; , Damaschke, N., Borys, M., and Tropea, C. (2003). *Laser Doppler and Phase Doppler Measurement Techniques*.
- Alzueta, M. U., Bilbao, R., Millera, A., Glarborg, P., Ostberg, M., and Dam-Johansen, K. (1998). "Modeling Low-temperature Gas Reburning. NO_x Reduction Potential and Effects of Mixing." *Energy & Fuels*, 12(2), 329-338.
- Apte, S. V., Mahesh, K., Moin, P., and Oefelein, J. C. (2003). "Large-eddy Simulation of Swirling Particle-laden Flows in a Coaxial-jet Combustor." *International Journal of Multiphase Flow*, 29(8), 1311-1331.
- Arai, M. "Flue Gas Recirculation for Low-NO_x Combustion System." *2000 International Joint Power Generation Conference*, Miami Beach, Florida.
- Ballester, J., Barroso, J., Cerecedo, L. M., and Ichaso, R. (2005). "Comparative Study of Semi-industrial-scale Flames of Pulverized Coals and Biomass." *Combustion and Flame*, 141(3), 204-215.
- Bassilakis, R., Zhao, Y., Solomon, P. R., and Serio, M. A. (1993). "Sulfur and Nitrogen Evolution in the Argonne Coals: Experiment and Modeling." *Energy and Fuels*(7), 710-720.
- Baumann, H., and Moller, P. (1991). "Pyrolysis of Hard Coals under Fluidised Bed Combustor Conditions." *Erdol Kohle-Erdgas Petrochem*(44), 29-33.

Baxter, L. (2005). "Biomass-coal Co-combustion: Opportunity for Affordable Renewable Energy." *Fuel*, 84(10), 1295-1302.

Baxter, L. (2002). "Personal Communications."

Baxter, L. L., Mitchell, R. E., Fletcher, T. H., and Hurt, R. H. (1996). "Nitrogen Release during Coal Combustion." *Energy and Fuels*, 10(1), 188-196.

Beer, J. M., and Chigier, N. A. (1972). *Combustion Aerodynamics*, Applied Science Publishers Ltd.

Brink, A., Kilpinen, P., and Hupa, M. (2001). "A Simplified Kinetic Rate Expression for Describing the Oxidation of Volatile Fuel-N in Biomass Combustion." *Energy & Fuels*, 15(5), 1094-1099.

Caraeni, D., Bergström, C., and Fuchs, L. (2000). "Modeling of Liquid Fuel Injection, Evaporation and Mixing in a Gas Turbine Burner Using Large Eddy Simulations." *Flow, Turbulence and Combustion*, 65(2), 223-244.

Chen, J., Haynes, B. S., and Fletcher, D. F. "A Numerical And Experimental Study of Tangentially Injected Swirling Pipe Flows." *Second International Conference on CFD in the Minerals and Process Industries*, Melbourne, Australia.

Chen, J. C., Castagnoli, C., and Niksa, S. (1992). "Coal Devolatilization During Rapid Transient Heating .2. Secondary Pyrolysis." *Energy & Fuels*, 6(3), 264-271.

Chen, J. C., and Niksa, S. (1992). "Coal Devolatilization During Rapid Transient Heating .1. Primary Devolatilization." *Energy & Fuels*, 6(3), 254-264.

Chen, W. Y., and Ma, L. (1996). "Effect of Heterogeneous Mechanisms during Reburning of Nitrogen Oxide." *AIChE Journal*, 42(7), 1968-1976.

Chum, H. L., and Overend, R. P. (2001). "Biomass and Renewable Fuels." *Fuel Processing Technology*, 71(1-3), 187-195.

Coda Zabetta, E., and Kilpinen, P. (2001a). "Improved NO_x Submodel for In-cylinder CFD Simulation of Low- and Medium-speed Compression Ignition Engines." *Energy & Fuels*, 15(6), 1425-1433.

Coda Zabetta, E., Kilpinen, P., Hupa, M., Stahl, K., Leppalahti, J., Cannon, M., and Nieminen, J. (2000). "Kinetic Modeling Study on the Potential of Staged Combustion in Gas Turbines for the Reduction of Nitrogen Oxide Emissions from Biomass IGCC Plants." *Energy & Fuels*, 14(6), 751.

Coda Zabetta, E. G. (2002). "Modeling of Nitrogen Oxides in Combustion at Elevated Pressures: Application to Biomass- and Oil-Derived Gaseous Fuels," Akademi University, Turku, Finland.

- Coda Zabetta, E. G., and Kilpinen, P. T. (2001b). "Gas-Phase Conversion of NH_3 to N_2 in Gasification, PART II: Testing the Kinetic Model." *IFRF Combustion Journal*(ISSN 1562-479X).
- Coelho, L. M. R., Azevedo, J. L. T., Faravelli, T., and Hesselmann, G. (2001). "Integrated Study of Reburn Technology by Means of Detailed Chemical Kinetics, CFD Modeling And Pilot Scale Testing." *IFRF Combustion Journal*(Article Number 200108).
- Correa, S. M. (1998). "Power Generation and Aeropropulsion Gas Turbines: From Combustion Science to Combustion Technology."
- Dagaut, P., Luche, J., and Cathonnet, M. (2000). "Experimental and Kinetic Modeling of the Reduction of NO by Propene at 1 Atm." *Combustion and Flame*, 121(4), 651-661.
- Damstedt, B., Tree, D., Baxter, L., Hansen, D., Knighton, T., Jones, J., and Christensen, C. (2005). "NO_x Formation in an Independently Fed, Cofired, 140kWth, Swirl Stabilized Burner." Proceedings to the Combustion Institute.
- Dayton, D. (2002a). "A Summary of NO_x Emissions Reduction from Biomass Cofiring." NREL/TP-510-32260, National Renewable Energy Laboratory.
- Dayton, D. (2002b). "A Summary of NO_x Emissions Reduction from Biomass Cofiring." National Renewable Energy Laboratory.
- De Soete, G. G. (1975). "Overall Reaction Rate of NO and N_2 Formation from Fuel Nitrogen." *15th Symposium (International) of Combustion, Combustion Institute, Pittsburgh*, 1093-1102.
- Dean, A. M., and Bozzelli, J. W. (2000). "Combustion Chemistry of Nitrogen." Gas Phase Combustion Chemistry, W. C. Gardiner, ed., Springer, New York.
- Diebold, J. P., and Bridgwater, A. V. (1997). "Overview of Fast Pyrolysis of Biomass for the Production of Liquid Fuels. Developments in Thermochemical Biomass Conversion." 5.
- DOE, E. o. (2003). "Executive Summary:
<http://www.eia.doe.gov/cneaf/electricity/epm/chap1.pdf>."
- Eaton, A. M., Smoot, L. D., Hill, S. C., and Eatough, C. N. (1999). "Components, Formulations, Solutions, Evaluation, and Application of Comprehensive Combustion Models." *Progress in Energy and Combustion Science*, 25(4), 387-436.
- Eatough, C. N. (1991). "Controlled Profile Reactor Design and Combustion Measurements," Dissertation, Brigham Young University, Provo.
- Eatough, C. N., and Smoot, L. D. (1996). "Devolatilization of Large Coal Particles at High Pressure." *Fuel*, 75(13), 1601-1605.

- Ebbing, D. D., and Wrighton, M. S. (1987). *General Chemistry*, Houghton Mifflin, Boston.
- Ekmann, J. M., Winslow, J. C., Smouse, S. M., and Ramezan, M. (1998). "International Survey of Cofiring Coal with Biomass and Other Wastes." *Fuel Processing Technology*, 54, 171-188.
- Energie. (2000). "Addressing the Constraints for Successful Replication of Demonstrated Technologies for Co-combustion of Biomass/waste."
- EPA, U. S. E. P. A. (2000). "Emission Scorecard 2000."
- Epple, B., Schneider, R., Schnell, U., and Hein, K. (1995). "Computerized Analysis of Low-NO_x Coal-fired Utility Boilers." *Combustion Science and Technology*, 108(4-6), 383-401.
- Faravelli, T., Bua, L., Frassoldati, A., Antifora, A., Tognotti, L., and Ranzi, E. (2001). "A New Procedure for Predicting NO_x Emissions from Furnaces." *Computers and Chemical Engineering*, 25, 613-618.
- Fenimore, C. P. (1971). "Formation of Nitric Oxide in Premixed Hydrogen Flames." 373-380.
- Fletcher, T. H., Kerstein, A. R., Pugmire, R. J., Solum, M. S., and Grant, D. M. (1992). "A Chemical Model of Coal Devolatilization: 3. Direct Use of ¹³C NMR Data to Predict Effects of Coal Type." *Energy and Fuels*, 6(4), 414-431.
- FlowserveCorp. (2002).
- Frassoldati, A., Frigerio, S., Colombo, E., Inzoli, F., and Faravelli, T. (2005). "Determination of NO_x Emissions from Strong Swirling Confined Flames with an Integrated CFD-based Procedure." *Chemical Engineering Science*, 60(11), 2851-2869.
- Gera, D., Mathur, M., Freeman, M., and O'Dowd, W. (2001). "Moisture and Char Reactivity Modeling in Pulverized Coal Combustors." *Combustion Science and Technology*, 172, 35-+.
- German, A. E., and Mahmud, T. (2005). "Modelling of Non-premixed Swirl Burner Flows Using a Reynolds-stress Turbulence Closure." *Fuel*, 84(5), 583-594.
- Glarborg, P., Alzueta, M. U., Dam-Johansen, K., and Miller, J. A. (1998). "Kinetic Modeling of Hydrocarbon Nitric Oxide Interactions in a Flow Reactor." *Combustion and Flame*, 115(1-2), 1-27.
- Glarborg, P., Jensen, A. D., and Johnsson, J. E. (2003). "Fuel Nitrogen Conversion in Solid Fuel Fired Systems." *Progress in Energy and Combustion Science*, 29(2), 89-113.

- Glarborg, P., Kristensen, P. G., Dam-Johansen, K., Alzueta, M. U., Millera, A., and Bilbao, R. (2000). "Nitric oxide reduction by non-hydrocarbon fuels. Implications for reburning with gasification gases." *Energy & Fuels*, 14(4), 828-838.
- Glarborg, P., and Miller, J. A. (1994). "Mechanism and Modeling of Hydrogen Cyanide Oxidation in a Flow Reactor." *Combustion and Flame*, 99, 475-83.
- Grammelis, P., and Kakaras, E. (2005). "Biomass Combustion Modeling in Fluidized Beds." *Energy & Fuels*, 19(1), 292-297.
- Hamalainen, J. P., Aho, M. J., and Tummavuori, J. L. (1994). "Formation of Nitrogen Oxides from Fuel-N through HCN and NH₃: a Model Compound Study." *Fuel*, 73, 1894-1898.
- Hampartsoumian, E., Folayan, O. O., Nimmo, W., and Gibbs, B. M. (2003). "Optimisation of NO_x Reduction in Advanced Coal Reburning Systems and the Effect of Coal Type." *Fuel*, 82(4), 373-384.
- Hein, K. R. G., and Bemtgen, J. M. (1998). "EU Clean Coal Technology: Co-combustion of Coal and Biomass." *Fuel Processing Technology*, 54, 159-69.
- Higashihara, T., Saito, K., and Murakami, I. (1983). "Oxidation of Hydrogen Cyanide in Shock Waves: Formation of Nitrogen Monoxide." *Journal of Physical Chemistry*, 87, 2707-13.
- HoribaInc. (2000). *Instruction Manual for PG-250 Potable Gas Analyzer*.
- Houser, T. J., McCarville, M. E., and Zhuo-Ying, G. (1988). "Nitric Oxide Formation from Fuel-nitrogen Model Compound Oxidation." *Fuel*, 67, 642-50.
- Hughes, E. E. "Utility Coal-Biomass Cofiring Tests." *Proceedings to the Department of Energy*.
- Jenkins, B. M., Baxter, L. L., Miles, T. R. J., and Miles, T. R. (1998). "Combustion Properties of Biomass." *Fuel Processing Technology*, 54, 17-46.
- Kelemen, S. R., Gorbaty, M. L., and Kwiatek, P. J. (1995). "Quantification of Nitrogen Forms in Coals." *Center for Applied Energy Research Journal*, 6(5).
- Kelemen, S. R., Gorbaty, M. L., Kwiatek, P. J., Fletcher, T. H., Watt, M., Solum, M. S., and Pugmire, R. J. (1998). "Chemical Structure of Coal Tar during Devolatilization Using Solid-State ¹³C NMR." *Energy and Fuels*, 12, 159-173.
- Kilpinen, P. (1997). "Detailed Kinetic Scheme "Kilpinen 97". "
<http://www.abo.fi/fak/ktf/cmc>, ed., Åbo Akademi University - PCG.

- Kilpinen, P., and Hupa, M. (1991). "Homogeneous N₂O Chemistry at Fluidized-Bed Combustion Conditions - a Kinetic Modeling Study." *Combustion and Flame*, 85(1-2), 94-104.
- Kilpinen, P. T., Leppälahti, J. K., Coda Zabetta, E. G., and Hupa, M. M. (1999). "Gas-Phase Conversion of NH₃ to N₂ in Gasification Part I: A Kinetic Modeling Study on the Potential of the Method." *IFRF Combustion Journal*, September (ISSN 1562-479X).
- Kitto, J. B., Jr., Bernstein, G. S., Bryk, S. A., Sarv, H., Telesz, R. W., and Tonn, D. P. (1998). "Lowest Cost Integrated NO_x Solutions for Title I and Ozone Transport Rule Compliance." *Fact-Vol 22, IJPGC-1998, 1*, 115-124.
- Kucukgokoglan, S., Aroussi, A., and Pickering, S. J. "Prediction of Interactions between Burners in Multiburner Systems." *MFTP-2000 ICHMT Symposium on Multiphase Flow and Transport Phenomena*, Antalya, Turkey.
- Leppälahti, J., and Koljonen, T. (1995a). "Nitrogen Evolution from Coal, Peat, and Wood during Gasification: Literature Review." *Fuel Processing Technology*, 43, 1-45.
- Leppälahti, J. L. (1995). "Formation of NH₃ and HCN in Slow-heating-rate Inert Pyrolysis of Peat, Coal and Bark." *Fuel*(74), 1363-1368.
- Leppälahti, J. L., and Koljonen, T. (1995b). "Nitrogen Evolution from Coal, Peat, and Wood during Gasification: Literature Review." *Fuel Processing Technology*, 43, 1-45.
- Leppälahti, J. L., Stahl, C., O., K., Cannon, M. F., and Nieminen, J. J. (1999). "Nitrogen Oxide Reduction by Staged Combustion of Biomass Gas in Gas Turbine-a Modeling Study of the Effect of Mixing." *ASME, the International Gas Turbine & Aeroengine Congress & Exhibition*.
- Li, C.-Z., and Nelson, P. F. (1996). "Fate of Aromatic Ring Systems during Thermal Cracking of Tars in a Fluidized-bed Reactor." *Energy and Fuels*(10), 1083-90.
- Liang, X. H., and Kozinski, J. A. (2000). "Numerical Modeling of Combustion and Pyrolysis of Cellulosic Biomass in Thermogravimetric Systems." *Fuel*, 79(12), 1477-1486.
- Lissianski, V. V., Zamansky, V. M., Maly, P. M., and Sheldon, M. S. (2000). "Optimization of Advanced Reburning via Modeling." *Proceedings of the Combustion Institute*, 2475-2481.
- Lu, H., Werrett, L., Vickers, M., Gunderson, T., and Baxter, L. "Effects of Particle Shape and Size on Biomass Reactivity." *2005 ACERC Conference*, Provo, UT.
- Marschner, H. (1990). *Mineral Nutrition of Higher Plants*.

- Nazeer, W. A. (1997). "Species and Temperature Measurements in a Pulverized Coal Controlled Profile Reactor with Natural Gas Reburning," Master Thesis, Brigham Young University, Provo.
- Nazeer, W. A., Pickett, L. M., and Tree, D. R. (1999). "In-situ Species, Temperature and Velocity Measurements in a Pulverized Coal Flame." *Combustion Science and Technology*, 143(1-6), 63-77.
- Nelson, P. F., Buchley, A. N., and Kelly, M. D. (1992a). "Functional Forms of Nitrogen in Coals and the Release of Coal Nitrogen as NO_x Precursors (HCN and NH₃)."
Proceedings of the Combustion Institute, 24, 1259-1267.
- Nelson, P. F., Buchley, A. N., and Kelly, M. D. (1992b). "Functional Forms of Nitrogen in Coals and the Release of Coal Nitrogen as NO_x Precursors (HCN and NH₃)."
1259-1267.
- NETL. (2005). "Advanced NO_x Emissions Control."
<http://www.netl.doe.gov/coal/E&WR/nox/>.
- Pedersen, L. S., Glarborg, P., and Dam-Johansen, K. (1998). "A Reduced Reaction Scheme for Volatile Nitrogen Conversion in Coal Combustion." *Combustion Science and Technology*, 131(1-6), 193-223.
- Pels, J. R., Kapteijn, F., Moulijn, J. A., Zhu, Q., and Thomas, K. M. (1995). "Evolution of Nitrogen Functionalities in Carbonaceous Materials During Pyrolysis." *Carbon*, 33(11), 1641-1653.
- Perry, S., Hambly, E. M., Fletcher, T. H., Solum, M. S., and Pugmire, R. J. "Solid-State ¹³C NMR Characterization of Matched Tars and Chars from Rapid Coal Devolatilization." *Combustion Institute*, 2313-2319.
- Pershing, D. W., and Wendt, J. O. L. (1977). "Pulverized Coal Combustion: The Influence of Flame Temperature and Coal Composition on Thermal and Fuel NO_x." *Proceedings of the Combustion Institute*, 16, 389-399.
- Peters, A. A. F., and Weber, R. (1997). "Mathematical Modeling of a 2.4 MW Swirling Pulverized Coal Flame." *Combustion Science and Technology*, 122(1-6), 131-182.
- Pickett, T. M., Jackson, R. E., and Tree, D. R. (1999). "LDA Measurements in a Pulverized Coal Flame at Three Swirl Ratios." *Combustion Science and Technology*, 143(1-6), 79-107.
- Poinsot, T., and Veynante, D. (2001). *Theoretical and Numerical Combustion*, R. T. Edwards Inc.
- Pollard, A., Ozem, H. L. M., and Grandmaison, E. W. (2005). "Turbulent, Swirling Flow over an Axisymmetric, Constant Radius Surface." *Experimental Thermal and Fluid Science*, 29(4), 493-509.

PowerScorecard. (2000). "Electricity and the Environment."

http://www.powerscorecard.org/elec_env.cfm.

Quaak, P. (1999). "Energy from Biomass." (ISBN: 0821343351), 1-6.

Rigby, J., Ma, J., Webb, B. W., and Fletcher, T. H. (2001). "Transformations of Coal-derived Soot at Elevated Temperature." *Energy and Fuels*(15), 52-59.

Robinson, A., Baxter, L., Junker, H., Shaddix, C., Freeman, M., James, R., and Dayton, D. (1998). "Fireside Issues Associated with Coal-Biomass Cofiring." *December 1998 \$ NREL/TP-570-25767*.

Schnell, U., Kaess, M., and Brodbek, H. (1993). "Experimental and Numerical Investigation of NO_x Formation and Its Basic Interdependencies on Pulverized Coal Flame Characteristics." *Combustion Science and Technology*, 93(1-6), 91-109.

Skreiberg, O., Kilpinen, P., and Glarborg, P. (2004). "Ammonia Chemistry below 1400 K under Fuel-rich Conditions in a Flow Reactor." *Combustion and Flame*, 136, 501-518.

Sloss, L. L., Hjalmarsson, A-K, sound, H. N., Campbell, L. M., Stone, D. K., Shareed, G. S., Emmel, T., Maibodi, M., Livengood, C. D., markussen, J. (1992). *Nitrogen Oxides Control technology Fact Book*, Noyes data Corporation.

Smirnov, A. (1995). "Evaluation of Different Turbulence Models Used in Simulation of Confined Swirl Flows." www.tfd.chalmers.se/~ansm/Public/report95.ps.

Smith, G. P., Golden, D. M., Frenklach, M., Nigel W. Moriarty, Eiteneer, B., Goldenberg, M., Bowman, C. T., Hanson, R. K., Song, S., Jr., W. C. G., Lissianski, V. V., and Qin, Z. (2000). "http://www.me.berkeley.edu/gri_mech/."

Smoot, L. D. (1993). "Fundamentals of Coal Combustion for Clean and Efficient Use." 196.

Smoot, L. D. (1997). "A Decade of Combustion Research." *Progress in Energy and Combustion Science*, 23(3), 203-232.

Smoot, L. D., Hill, S. C., and Xu, H. (1998). "NO_x Control through Reburning." *Progress in Energy and Combustion Science*, 24(5), 385-408.

Solero, G., Terragni, C., and Coghe, A. "Experimental Analysis on Turbulent Mixing in a Swirl Burner." *Open meeting on Combustion, Ischia*.

Solomon, P. R., Serio, M. A., and Suuberg, E. M. (1992). "Coal Pyrolysis: Experiments Kinetic Rates and Mechanisms." *Progress in Energy and Combustion Science*, 18, 133-220.

Spliethoff, H., and Hein, K. R. G. (1998). "Effect of Co-combustion of Biomass on Emissions in Pulverized Fuel Furnaces." *Fuel Processing Technology*, 54(1-3), 189-205.

Stubington, J. F., Ng, K. W. K., Moss, B., and Peeler, P. K. (1997). "Comparison of Experimental Methods for Determining Coal Particle Devolatilization Times under Fluidized Bed Combustor Conditions." *Fuel*, 76(3), 233-240.

Terentis, A., Doughty, A., and Mackie, J. C. (1992). "Kinetics of Pyrolysis of a Coal Model Compound 2-picoline, the Nitrogen Heteroaromatic Analogue of Toluene. 1. Product Distributions." *Journal of Physical Chemistry*, 96(10334-9).

Tree, D. R. (2002). "Personal Communications."

Tree, D. R., Black, D. L., Rigby, J. R., McQuay, M. Q., and Webb, B. W. (1998). "Experimental Measurements in the BYU Controlled Profile Reactor." *Progress in Energy and Combustion Science*, 24(5), 355-383.

Tree, D. R., and Clark, A. W. (2000). "Advanced Reburning Measurements of Temperature and Species in a Pulverized Coal Flame." *Fuel*, 79(13), 1687-1695.

Veras, C. A. G., Saastamoinen, J., Carvalho, J. A., and Aho, N. (1999). "Overlapping of the Devolatilization and Char Combustion Stages in the Burning of Coal Particles." *Combustion and Flame*, 116(4), 567-579.

Wargadalam, V., Loffler, J. G., Winter, F., and Hofbauer, H. (2000). "Homogeneous Formation of NO and N₂O from the Oxidation of HCN and NH₃ at 600-1000C." *COMBUSTION AND FLAME*, 120, 465-478.

Watt, M., Fletcher, T. H., Bai, S., Solum, M. S., and Pugmire, R. J. "Chemical Structure of Coal Tar During Devolatilization." *Twenty-Sixth Symposium (International) on Combustion*, Pittsburgh, PA, 3153-3160.

Wendt, J. O. L. (1995). "Mechanisms Governing the Formation and Destruction of NO_x and Other Nitrogenous Species in Low-NO_x Coal Combustion Systems." *Combustion Science and Technology*, 108(4-6), 323-344.

Widmann, J. F., Charagundla, S. R., and Presser, C. (1999). "Benchmark Experimental Database for Multiphase Combustion Model Input and Validation: Characterization of the Inlet Combustion Air." *NISTIR 6370*, National Institute of Standards and Technology.

Williams, A., Pourkashanian, M., and Jones, J. M. (2001). "Combustion of Pulverised Coal and Biomass." *Progress in Energy and Combustion Science*, 27(6), 587-610.

Winter, F., Loffler, G., Wartha, C., Hofbauer, H., Preto, F., and Anthony, E. J. (1999a). "The NO and N₂O Formation Mechanism under Circulating Fluidized Bed Combustor Conditions: from the Single Particle to the Pilot-scale." *Canadian Journal of Chemical Engineering*, 77(2), 275-283.

Winter, F., Wartha, C., and Hofbauer, H. (1997). "A NO/N₂O - Classification System of Single Fuel Particles: Developments in Thermochemical Biomass Conversion." *Blacie Academic and Professional*, 1306.

Winter, F., Wartha, C., and Hofbauer, H. (1999b). "NO and N₂O Formation during the Combustion of Wood, Straw, Malt Waste and Peat." *Bioresource Technology*, 70(1), 39-49.

Wojtowicz, M. A., Miknis, F. P., Grimes, R. W., Smith, W. W., and Serio, M. A. (2000). "Control of Nitric Oxide, Nitrous Oxide, and Ammonia Emissions Using Microwave Plasmas." *Journal of Hazardous Materials*, 74(1-2), 81-89.

Xu, H. J., Smoot, L. D., Tree, D. R., and Hill, S. C. (2001). "Prediction of Nitric Oxide Destruction by Advanced Reburning." *Energy & Fuels*, 15(3), 541-551.

Yin, C. G., Rosendahl, L., Kaer, S. K., and Condra, T. J. (2004). "Use of Numerical Modeling in Design for Co-firing Biomass in Wall-fired Burners." *Chemical Engineering Science*, 59(16), 3281-3292.

Zel'dovich, Y. B., Sadvnikov, P. Y., and Frank_Kamentskii, D. A. (1947). "Oxidation of Nitrogen in Combustion."

Zhang, H. (2000). "Nitrogen Evolution and Soot Formation during Secondary Coal Pyrolysis," PhD Dissertation, Brigham Young University, Provo, UT.

Zhang, J., and Nieh, S. (2000). "Swirling, Reacting, Turbulent Gas-particle Flow in a Vortex Combustor." *Powder Technology*, 112(1-2), 70-78.

Zhou, L. X., Wang, F., and Zhang, J. (2003). "Simulation of Swirling Combustion and NO Formation Using a USM Turbulence-chemistry Model." *Fuel*, 82(13), 1579-1586.

Appendices

Appendix A. Literature Review on NO_x From Low-grade Fuel Combustion

Generation classification of NO_x formation from combustion

NO_x mainly refers to NO and NO₂ (Smoot et al. 1998), and causes a variety of environmental and health problems. In the atmosphere, NO can be rapidly oxidized to NO₂, which is an important source of acid rain and urban smog. The largest source of NO_x is petroleum, in particular mobile sources, such as automobiles and airplanes. Mobile sources alone account for at least 50% of the NO_x emissions arising from human activities. Power stations account for an additional 25% of NO_x emissions (Sloss 1992). Beginning in the 1980s, increasingly stringent regulations on NO_x emissions have been implemented throughout the world. The NO_x emission limit created by the Clear Air Act Amendments (CAAA) on power plants has continuously decreased, effectively decreasing the NO_x emissions even though the total energy produced has increased.

During combustion, NO_x formation mechanisms fall into three categories:

- (a) Thermal-NO_x: Zeldovich defined the thermal-NO_x in 1947. (Zel'dovich et al. 1947) When temperatures are greater than 1650 K, molecular nitrogen is oxidized by O₂. Thermal-NO_x formation is primary a function of flame temperature. In the power generation industry, thermal-NO_x accounts for 5% to 25% of total NO_x emissions. (b)

Prompt-NO_x: Fenimore (Fenimore 1971) introduced this process of NO_x formation in 1971. Prompt NO_x is produced by high-speed reactions at relatively low

temperature in fuel rich flames. Highly reactive fuel radicals are responsible for the initiation of reaction with N_2 . A number of species resulting from fuel fragmentation have been suggested as the source of prompt NO_x in hydrocarbon flames, but the major contribution is from CH and CH_2 radicals. Prompt NO_x formation is proportional to the number of carbon atoms present per unit volume and is independent of the parent hydrocarbon identity. As the equivalence ratio increases, prompt NO_x production increases at first, then passes a peak, and finally decreases due to a deficiency in oxygen. At present the prompt NO_x contribution to total NO_x from stationary combustors is so small that it is considered being negligible.

(c) Fuel- NO_x : Fuel- NO_x investigations began in the 1970s. Fuel- NO_x is generated from the oxidation of fuel-bound nitrogen. Currently, fuel- NO_x contributes to more than 75% of NO_x emissions in the power generation industry and more than 90% of NO_x from nitrogen-containing fuels such as coal and biomass. The formation of fuel- NO_x from biomass cofiring is the topic of the current research.

By decreasing the flame temperature, one can minimize thermal- and prompt- NO_x in industrial facilities. Nevertheless, fuel- NO_x remains a problem for essentially all combustion systems. Therefore, the fate of fuel-N in combustion is of great interest. In particular, the prediction of fuel- NO_x emissions from low-grade fuels and their blends is a major objective for minimizing the environmental impact of combustion. .

Fuel- NO_x conversion differs greatly among different categories of fuels. Figure 2.2 shows the conversion of fuel-N to NO , N_2O and HCN versus the nitrogen content of the fuels measured in the laboratory-scale multimode fluidized bed combustor at $800^\circ C$ bed temperature and 10-kPa oxygen (Diebold and Bridgwater 1997). The fuels adopted in

the analyses were classified into three types according to their behavior and nitrogen content: Low N-content with high N-conversion (I); Medium N-content with medium N-conversion (II); High-nitrogen content with low N-conversion (III). The conversion of fuel-N to NO is much higher than that to N₂O. For low nitrogen content and fuel-lean flames, high conversion of fuel-N to NO was observed. A similar trend of fractional conversion of fuel-N in flames with nitrogen content of the fuel was found for a range of fossil and synthetic fuels in practical combustors. Fuel with high nitrogen content generally shows low NO and NH₃ conversions. However, the concentrations of nitrogenous species are higher in the combustion zones for higher N-content fuels.

Currently, fuel-NO_x contributes more than 90% of NO_x from low-grade fuel (biomass and coal, etc.) combustion systems. Fuel-NO_x formation depends strongly on oxygen concentration and only moderately on flame temperature, in contrast to thermal-NO_x. HCN and NH_x are the NO_x precursors during pyrolysis and oxidation of most low-grade fuels. Most authors postulate fuel-NO_x mechanisms centered on HCN production from fuel-bound nitrogen, with possible subsequent formation of NH_x. Highly detailed gas-phase mechanisms for nitrogen chemistry involving HCN and NH_x as major intermediates in NO_x formation exist and will be discussed later.

Modeling in fuel-NO_x research

In contrast to expensive, time-consuming test-runs, modeling is more rapid and economical and can be more descriptive. The complexity involved in NO_x modeling is caused by the need to simultaneously solve fluid dynamic and chemical kinetic equations, both of which are highly computationally intensive.

Although the principles of kinetics and fluid dynamics are well established, the details in simulation of combustion systems, especially turbulent systems, need to be refined to improve accuracy and extend applicability. Furthermore, the inter-related nature of the fluid dynamics and kinetics (termed ‘turbulence chemistry’) results in the fact that it usually takes much more iterations than solving respective kinetic or fluid dynamics equations sets describing combustion processes. Recently, the increased capabilities of computers has allowed comprehensive modeling, accounting simultaneously for both detailed fluid dynamics and detailed chemical kinetics at the expense of very long calculation time, but testing is still necessary before comprehensive kinetics and dynamics modeling can be reliably and extensively used in engineering (Grammelis and Kakaras 2005) . There are two options to avoid large computation time: one is to simplify the detailed chemistry scheme, while keeping the detailed fluid dynamics and the other is to maintain the detailed chemistry and idealize the fluid dynamics with appropriate mixing models if needed. Some often used detailed and reduced gas phase N-reaction mechanism will be discussed later in this paper.

Many detailed chemistry schemes accounting for the fate of nitrogen under combustion environments have been developed which are described briefly below.

Detailed gas-phase kinetic schemes involving fuel-N chemistry

The detailed mechanisms focus on light gases and combustion chemistry under conditions similar to that of natural gas combustion. These mechanisms do not involve more than three carbon atoms in the radicals or stable species, and they are modestly successful in predicting major species under a variety of conditions (Baxter 2002).

The well-known Miller-Bowman mechanism (Hampartsoumian et al. 2003) is one of the earliest comprehensive mechanisms capable of modeling thermal-, prompt-, and fuel- NO_x formation. Glarborg and coworkers updated Miller-Bowman mechanism against new experimental data and modeling results for application with reburning resulting in an (Glarborg et al. 2000) improved mechanism is called the Miller & Glarborg mechanism (M&G), which contains 184 elementary reactions, among which 144 account for nitrogen chemistry. The M&G detailed mechanism is one of the best tools in describing the reactions of NO with C_1 and C_2 hydrocarbons under reducing conditions, and at comparatively lower temperatures, i.e., 800–1500 K. It includes the reburning fuels CH_4 , C_2H_2 , C_2H_4 , C_2H_6 , and natural gas (Alzueta et al. 1998; Glarborg et al. 1998). It has demonstrated that $\text{HCCO} + \text{NO}$ and $\text{CH}_3 + \text{NO}$ are the main reactions in reducing NO during reburning with these fuels. In particular, the latter plays a dominant role in reducing NO when natural gas or methane is used as a reburning fuel.

The Kilpinen 92 mechanism (Kilpinen and Hupa 1991) is based on the mechanisms of Miller and Bowman. It involves 49 species in 253 elementary gas-phase reactions, including submechanisms for oxidation of C_1 - C_2 hydrocarbons, HCN, and NH_3 , as well as for interactions between hydrocarbons (CH_i , HCCO) and nitrogen species (NO , NH_i , and N_2 , etc). The mechanism was originally developed to predict the conversion of NO_x via thermal, prompt, N_2O -intermediate, and fuel mechanisms in atmospheric processes at high temperatures, (Coda Zabetta and Kilpinen 2001b). A number of changes were introduced to upgrade the mechanism for pressurized applications, especially NO_x formation from the combustion of biomass gasification gas in gas turbines and ignition engines. The Kilpinen 97 mechanism (Kilpinen 1997) is an upgraded version

of the Kilpinen 92 and it includes 353 reactions between 57 species. The upgrade uses more accurate kinetic constants, as well as the introduction of new reactions involving N-containing species including N_2H_3 , N_2H_4 , HONO , NO_3 , H_2NO , NCN , C_2N_2 , and HNNO . The two mechanisms have been validated against a body of experimental data, and have been found to be satisfactory in describing nitrogen reactions under a variety of experimental conditions.

The GRI-Mech 3.0 (Smith et al. 2000) is the most recent and most comprehensive version of the mechanisms developed at the Gas Research Institute. This mechanism is a compilation of 325 reactions between 53 species, conceived for natural gas ignition and flame propagation, including NO formation and reduction. This mechanism proposes new paths for the formation of formaldehyde, NO, and reburning targets compared to its former versions. However, it is only reliable for the modeling of the combustion of methane and natural gas, including the by-products originating from combustion of natural gas. GRI-Mech 3.0 is optimized for premixed systems with temperatures ranging from 1000 to 2500 K, pressures 103 to 106 kPa, and equivalence ratios from 0.1 to 5.

The Dagaut 00 is the comprehensive mechanism developed by Dagaut et al. (Dagaut et al. 2000) for the reduction of NO by natural gas blends in reburning conditions. The mechanism involves 871 reactions with 112 species, including the reactions accounting for the selective oxidation of ammonia. The mechanism has been validated against atmospheric experiments, especially for gas mixtures containing about 0.3% propane and 750-1000 ppm of NO, oxidized at fuel/air equivalence ratios 0.5-2 and at temperatures ranging from 1100 to 1450 K.

Comparison of these detailed mechanisms in predicting the gas-phase NH_3 chemistry in gasification by Coda Zabetta and Kilpinen (Coda Zabetta and Kilpinen 2001b) demonstrated the Kilpinen 97 is more reliable than the Kilpinen 92, which is more accurate than the Dagaut 00 and much more reliable than the GRI-Mech 3.0 in the cases studied. The Kilpinen 97 detailed kinetics predicted homogeneous N-reactions under a variety of conditions reasonably well. No comparison with the M&G mechanism was discussed.

Reduced fuel-N kinetic models

It has been found that usually only a minor group of reactions are responsible for most of NO_x generated in kinetic schemes (Pedersen et al. 1998). These reactions are called a skeletal kinetic set, which can be further simplified to a reduced mechanism.

Reduced nitrogen chemistry models describing fuel- NO_x generation have shown their flexibility and high efficiency in the prediction of NO_x emissions in lab- and pilot-scale burners. Generally, there are two types of reduced mechanisms: the first comes from empirical models; the second from detailed kinetic mechanisms. A major disadvantage of the first method is that it is only reliable under very specific conditions, and their extrapolation is highly hazardous because of the invalidity of the empirical models outside of empirically validated conditions. Some examples include the NO_x formation models by Fenimore (Fenimore 1971), by De Soete (De Soete 1975) and by Mitchell and Tarbell (Gera et al. 2001). Examples of models from detailed chemistry are Wendt (Wendt 1995) and Pedersen et al. (Pedersen et al. 1998). Comparison of all the reduced models mentioned above in the prediction of HCN under pulverized coal flames

conditions with a variety of stoichiometries by Pedersen et al.(1998) demonstrated that models by Fenimore and Wendt can only be applied at fuel-rich conditions. Only the De Soete model shows that the presence of NO has a significant influence on the HCN oxidation rate. The model by Mitchell and Tarbell was able to predict the trend for total fixed nitrogen correctly, with slight over-prediction. The model by Pedersen et al. is the best among the models compared under the conditions simulating pulverized coal flame (Pedersen et al. 1998). The model was developed with an HCN submodel for HCN/NH₃/NO conversions based on the systematic reduction of the M&G mechanism. The oxidation of HCN in the flame zone is controlled mainly by radicals generated by the combustion of main species of CO and H₂. Models of different complexity have been tested with the detailed mechanism under conditions similar to pulverized coal combustion. Comparisons were made for ideal chemical reactors (plugged flow reactors and continuously stirred reactors). The results showed the reduced model worked well compared to the detailed one over a wide range of reaction stoichiometries and a temperature range from 1200 K to 2000 K.

Fuel-nitrogen chemistry in biomass gasification and reburning

Because of the scarcity of the experiment data of NH₃ from biomass fuel-N in coal LNBs, it is necessary to relate the process environment with that of biomass gasification and that of advanced reburning because their principal fuel-N kinetic conditions are similar. All of these processes are under fuel-rich, gas-phase dominant reactions with similar operating temperature windows, and in the fuel-rich region, the gas components are likely to be composed of mainly N₂, CO, some hydrocarbons, and CO₂, with nitrogen species dominated by NH₃. Theoretically, the primary zone should be

highly oxygen starved. However, because the reactions in a LNB primary zone are mixing-control, some unreacted O₂ should be taken into consideration as well. .

Biomass gasification is the reaction of solid fuels with only a portion of the oxygen required for complete combustion. During gasification HCN is converted by steam to NH₃ resulting in concentrations in the products that can be several thousand ppms. Results from the modeling of biomass gasification with the Kilpinen 97 showed that both O₂ and NO are attractive oxidizers, but there are no synergistic effects. Hydrocarbons present in the gases were reported to inhibit the oxidation of ammonia, and correspondingly enhance the selectivity to N₂ through generation of HCN. But the amount of HCN was so small that the effect of hydrocarbons on fuel-N evolution is not treated as a primary factor and is considered negligible. The CO/H₂ chemistry has been proved to have great influence on the fate of HCN in the pulverized coal flame region.

Advanced reburning used to reduce NO_x can introduce high fuel-N content fuels in addition to hydrocarbons. The key reactions involved in advanced reburning can be categorized into the following five types (Xu et al. 2001):

The reduction of NO_x by ammonia to molecular nitrogen



The oxidation of NH₃ to NO_x



The reduction of NO_x by hydrocarbon radicals





The reactions when CO is present in the system



The conversion of HCN to NH₃



Temperature plays an important role in advanced reburning. There is a competition between reactions type 1 and type 2. At lower temperatures (<1000K), type 1 does not proceed, since the concentration of O, H, and OH are too low. When temperature increases, oxidation of NH₃ type 2 to an increasing degree leads to formation of NO, and the net effect is that the overall fractional NO conversion to N₂ is reduced. (Xu et al. 2001). In advanced reburning, the role of hydrocarbon radicals is limited, but it can be treated as radical pools for type 5, the conversion of HCN to NH₃, which is enhanced under low oxygen concentration. Type 4 produces OH radicals at the same time competes with type 1 by consuming OH radicals, and the former effect is dominant unless temperature is too low (< 300 K). At high temperatures, too much CO will promote oxidation of NH₃ to NO because it consumes too much OH.

Present status of biomass cofiring

Most biomass power plants are based on stand-alone biomass fired boilers and steam turbine technology, and they usually have a much smaller capacity than fossil fuel

power plants (Hein and Bemtgen 1998). Because biomass has a much lower heating value than fossil fuels, the biomass power plants are very sensitive to the fluctuation of the fuel-supply to maintain a constant power supply. Cofiring biomass with coal in coal-fired power plants is a promising option to reduce the high cost and efficiency disadvantages of stand-alone biomass boilers. Large coal fired plants are more efficient (around 35%) than the smaller dedicated biomass plants (typically 20%) (Baxter 2005). Cofiring can be implemented in a manner that maintains capacity and can be deployed appropriately to achieve both economic and environmental benefits. Furthermore, cofiring can increase boiler capacity if it is injected separately into the unit and if pulverizer capacity is the limiting factor in overall unit capacity.

Different levels of cofiring tests have been practiced with thermal input of up to 10% on an energy basis in units designed to burn pulverized or crushed coal in both Europe and the United States (Hein and Bemtgen 1998; Hughes 1998). Considerable experience exists on cofiring coal and a number of biomass materials. Cofiring biomass including wood wastes and agricultural residues with coal has been evaluated, tested and practiced for a variety of biomass types and co-firing shares in combination with different combustion technologies and processes, including grate firing, cyclone boilers, wall-fired and tangentially-fired pulverized coal boilers, fluidized-bed boilers, and stoker-fired boilers (Ekman et al. 1998). Cofiring biomass with coal is considered as an effective option for increasing the share of renewable energy in fuel consumption and reducing the anthropogenic CO₂ emissions, because of the lower capital and operating cost, higher electrical efficiencies and increased fuel flexibility. This technique not only acts as a viable way to manage the increasing emissions of greenhouse gases, but also as a

practical approach for the reduction of other pollutants from power generating facilities, although some uncertainties exist at present. For example, cofiring wood at moderate and high percentages in cyclone boilers (up to 20% on a mass basis), has significant environmental benefits and site-specific boiler efficiency and economic impacts. Because of the negligible sulfur content of hardwood fuels, SO_x emissions almost uniformly decrease by the displacement of sulfur in the fuel blend when cofiring. Similar reductions are also observed for NO_x emissions because the nitrogen content of the cofired biomass fuels is generally much lower than the nitrogen content of the coal. An additional incremental SO_x reduction beyond the amount anticipated on the basis of fuel sulfur content is sometimes observed and is based on sulfur retention by alkali and alkaline earth metals in the fuels.

Cofiring can increase fuel flexibility with the possibility of additional generation capacity. If biomass were cofired at low percentages in these plants, the use of biomass for power production could dramatically increase. Fuel diversity reduces the need for a constant supply of biomass required in a biomass power plant. Besides, the savings from cofiring biomass are not only from displacement of coal, but also from not using materials for landfill, which ultimately decomposes and forms both CO_2 and CH_4 , a more powerful greenhouse gas species.

Cofiring indirect benefits to the forestry and secondary wood products industry by providing new markets for wastes and residues as well as dedicated feedstock, thereby promoting economic stability in the utilities service area; and the potential to develop feedstock infrastructure and jobs for long term biomass development and use.

Currently, coal-fired power plants are used to produce most of the electricity in the United States. The generation capacity for cofiring biomass and wastes in existing coal-fired plants could theoretically reach 2 GW by 2005 and 5 GW by the year 2010, 15% of the energy from coal annually (Baxter 2005). The current experience with biomass cofiring in the USA is almost limited to non-commercial tests. By 2005, there have been over one hundred commercial boilers and about one hundred stand-alone biomass plants in the US. For the near term, co-firing is considered the most cost-effective method for biomass power generation. However, there are still several technical barriers slowing down the widespread usage of biomass cofiring, which are discussed in the following section based on the proceedings of a cofiring seminar at Nottingham, UK in 2002.

Technical barriers of cofiring

Biomass has a much higher volatile content (up to 95%) than that of coal (up to 60%), meaning the homogeneous mechanisms may dominate in combustion. The ash content of biomass varies greatly with the type of plant: hardwood has less than 0.5% (wt, dry basis), while some agricultural crops can range from 5 to 25% ash (wt, dry basis). Rice husk has an ash fraction of 40% (wt, dry basis). The oxygen content is usually about 40-45 % (moisture and ash free basis), giving biomass only a modest energy content, e.g. the LHV for dry biomass is 19-20 MJ/kg (Quaak 1999), leaving the volume energy density 1/5 to 1/10 of high rank coal. This means feeding and transportation of biomass can be a potential problem in its industrial use as an energy source.

Prudent choices of fuels, boiler design, and boiler operation should lead to little or no fireside problems during cofiring. Pilot-scale data indicate that biomass ash deposition rates can either exceed or be less than those of coal, depending on the type of biomass used. For example, hardwood fuels generally contain very little ash (1% or less), and consequently, increasing the ratio of wood in biomass/coal blends can reduce the amount of ash that needs to be disposed (Ekman et al. 1998). The potential for chlorine-based corrosion is seen to be less significant for cofiring than for pure biomass fuels in most cases, but may not always be negligible.

The major technical constraints related to biomass cofiring can be classified into following categories: fuel supply and storage, feeding and preprocessing, and impacts on the facilities.

Fuel supply and storage

The potential for successful application of cofiring is extremely site-specific. The cofiring feasibility is conditioned by the characteristics of the power plant being considered and the secure supply of the low cost biomass in the vicinity of the plant. Because of the much lower energy density of biomass than coal, enormous amounts of extra space needs to be provided for the biomass storage. The fuel storage processes are always accompanied with emissions including dust, fungi spores, methane, and odors, leading to an increased risk of decomposition, dust explosions, self ignition and fires.

Feeding and preprocessing

The feeding of biomass into coal boilers can be distinguished as direct and indirect co-combustion. Direct co-combustion is defined as all components of the

secondary fuel enter the boiler together with the primary fuel. For indirect feeding, the thermal conversion is partially done in a separate installation. For example, biomass can be gasified, followed by the gas being cooled down and cleaned before entering the main coal furnace. Indirect combustion is an effective way to manage ash and solve burnout problems. However, indirect combustion requires higher capital cost than direct co-combustion, which requires minimum adjustments at the plant design and equipment.

As the most commonly applied configuration, direct combustion is characterized by high efficiency and low investment, minimizing operation risk by limited interfaces between the biomass firing systems and the rest of the plants. However, although many combustion beds are flexible to fuel specifications, it is not always possible to use the existing feeding installation to premix biomass with coal. Biomass cofiring can have a negative impact on boiler capacity if it is introduced through the coal transport pathway of crushers and pulverizers. When the feeding characteristics of the biomass vary too much from coal, a separate feeder needs to be installed. Most successful direct feeding tests have been limited by clean wood waste, and very little experience has been gained with other biomass.

For current commercial coal-fired boilers, most fuels require size reduction. Size reduction of biomass is always more energy intensive than for coal, because wood is usually much more difficult to grind in a coal grinder. It is impractical to reduce most biomass fuels to the size of pulverized coal (less than 100 microns). Fuel conditioning, e.g. with shredders, mills, conveying and feeding the process can be interrupted or stopped as a result of bridging, plugging, stickiness, tightness and blockages, resulting wearing and damages to the relevant facilities

Cofiring a blend of wood and coal through the traditional coal transport and delivery system can significantly impact the pulverizer performance and feeding speeds depending upon the condition and the percentage of wood fired. At low level cofiring tests (up to 8% mass basis), wood can be combined with coal prior to pulverizers with acceptable pulverizer power consumption and performance. For medium levels, with a biomass weight fraction of 8-15%, a separate wood preparation, delivery and feeding system should be considered during boiler operation based on coal characteristics. When the mass fraction is over 50%, a boiler designed specifically for biomass operation should be used.

Impacts on the facilities during biomass cofiring

Carbon burnout

Some of the problems with co-firing are related to the variation in combustion characteristics of biomass and coal. When co-firing biomass in an existing coal installation, the amount of flue gases per unit of energy increases, which may cause flow patterns of combustion gases and temperature profiles through the boiler to be dramatically modified.

Burnout depends on the residence time at high temperatures, the size of the particle and the moisture content of the fuel. If the residence time is not sufficient, the biomass particles are too large, or the moisture content is too high, the burnout can deteriorate. Experience shows that even with sufficiently fine biomass particles, CO emissions increased by 50% when pure biomass combustion was compared to coal in a commercial boiler (Spliethoff and Hein 1998).

Pulverized coal particles are much smaller than the practically achievable sizes for biomass fuels, resulting in lower burnout and increased amounts of unburned carbon in cofiring fly-ashes (Robinson et al. 1998). Test results from Spliethoff et al. (Spliethoff and Hein 1998) demonstrated that the maximum particle size achieving complete burnout was about 6 mm for straw and about 4 mm for Miscanthus, a type of wood. For certain biomass fuels with a moisture content of 35-40%, a good rule of the thumb is that an average size should be around 3mm for a satisfactory burnout (Baxter 2005; Baxter). With increasing content of moisture in the fuel, the particle size should be less, and vice versa.

Ash management

Herbaceous biomass, such as grasses, straw, and agricultural residues have much higher alkali and chloride contents than coal. During combustion of these fuels, the significantly lower melting point of biomass ash adds risk of slagging, fouling, and sintering on walls and tubes in pulverized coal boilers. Chloride may cause severe corrosion on boiler tubes, however it was found that this problem is less for biomass with high alkali contents, such as straw, because a protective layer of slag may be formed that actually protects the metal for Cl-corrosion (Jenkins et al. 1998).

Significant amounts of submicron level alkaline material can also be found in biomass ash, and this caused accelerated aging and deactivation of the SCR catalysts. Co-firing fractions of biomass can be limited due to changes in the efficiency and maintenance of the flue gas clean-up systems. (Energie 2000)

Another major barrier to biomass cofiring is the marketability of the ash.

Although the quality of fly-ash from cofiring is not necessarily worse than that of pure coal-firing, the existing standards for the use of fly ash in cement and concrete exclusively allow the usage of coal fly ash. Further research is needed on the influence of ash composition on the concrete strength.

NO_x emissions

Biomass co-firing is typically observed to produce an increase in NO_x on an energy basis. Most of the reasons for this observation and co-firing practices which can mitigate this problems have been partially or completely solved(Baxter 2005; Baxter). Experience shows that an appropriate combination of biomass, facilities, and operating conditions can be used to maintain or reduce NO_x emissions. This research is focused on the gas phase formation of NO_x during cofiring biomass, and a detailed review of NO_x is given in the following section.

NO_x from cofiring

It has been reported that NO_x emissions from biomass can either exceed or be less than that for coal. In comparison with coal at equivalent fuel-N content, NO_x emissions on an energy basis are higher due to the lower energy content of biomass fuels. Initially, any change in NO_x emissions during cofiring can be attributed to the change of nitrogen density on an energy basis in the fuel mixture, depending on the joint effect of the lower energy density and lower nitrogen content than coal.

Besides fuel-N content, many other engineering factors contribute to NO_x formation in full-scale cofiring applications. The mechanism for NO_x formation is also

associated with stoichiometry, fuel volatility, moisture content, and temperature in a fairly complex manner (Dayton 2002b). The high volatiles content of biomass can effectively establish a fuel-rich zone early in the flame that can reduce NO_x emissions. Adding biomass can also reduce flame temperatures, leading to lower levels of thermal NO_x . The high moisture content of some biomass may also be effective for NO_x reduction at full-scale. Results from direct feeding cofiring tests, with straw and wood as the supplementary fuels, respectively, showed that little impact of the fuel nitrogen content was found in the combustion processes. This might be caused by the delayed combustion of the biomass particles because of coarser milling and its high moisture content, resulting only little of its volatile nitrogen components are converted into NO .

Though the large difference in fuel oxygen contents between biomass and coal suggests that blends of coal and biomass could produce quite different results based on the behavior of the individual fuels, results from cofiring tests indicate that NO_x emissions from blends of coal and biomass interpolate quite accurately between the measured behaviors of the neat coal and biomass fuels if no LNBS, fuel staging, or boiler technology is used. And this suggests that there can be no significant chemical interaction between the off-gases (Robinson et al. 1998).

Appendix B. Recasting the Refractory Liner in the BFR

Overview

To model the BFR as accurately as possible, it is necessary that the CFD model and the reactor geometries must match. The need for recasting the BFR came about as a result of heavy slag formation and pieces of the old refractory falling off, causing unaccountable deviations in the geometry. Some changes were made to the original design.

Safety Issues

1. Caution must be observed during the operation of the cement mixer to avoid electric shock and physical hurt due to the mechanical nature of the mixer.
2. Inhalation of the cement dust can cause lung and throat irritation.
3. Wash hands after handling the wet cement. Wet cement is slightly alkaline and will cause burning if directly exposed to skin for extended periods of time.

Equipment

Cement

The cement we chose to use came from Refractories West Inc. Kast-o-lite 30LI was used because of its low thermal conductivity, as well as its ability to offer some structural support.

The cement appears dry when the proper amount of water has been added. The final decision was to use about 25-50% more water than the recommended amount. This made the cement easier to mix, and to place into the molds.

Molds

The following molds are needed and can be found in the storage garage:

- A) 1 – Bottom ring plate
- B) 4 – $\frac{1}{4}$ sections
- C) 2 – $\frac{1}{2}$ sections (use the smaller of the two types)
- D) 4 – Wooden window plugs

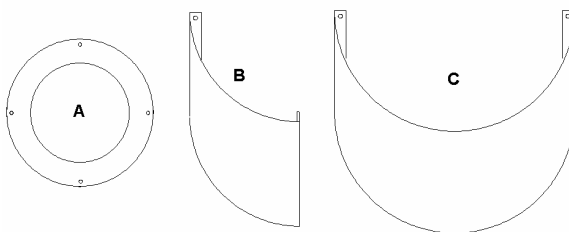


Figure A. 1 Parts for the recasting: A bottom ring plate; B $\frac{1}{4}$ section; C $\frac{1}{2}$ section.

Mold Release

Mold release or grease is needed to prevent the cement from bonding with the molds. Automotive grease was used from Checker Auto Parts.

Execution

Preparation:

Reactor Sections

- 1) Remove all old refractory from sections. Pay particular attention to removing all the cement that is bonded to the tabs near the reactor windows. Note: It is okay to throw the refractory in the dumpsters. It does not qualify as hazardous waste.

- 2) Using the winch, elevate the section and bolt the bottom ring plate to the bottom of the section.

Molds:

$\frac{1}{4}$ Sections

- 1) Apply the mold release to the mold.
- 2) Place the mold in between the windows, centered between the tabs.
- 3) Fix the position by taping the mold down with duct tape.

$\frac{1}{2}$ Sections

- 1) Apply mold release.
- 2) Bolt the flanges together to make a full, smooth circle.
- 3) Fit the molds into the inside of the bottom ring plate.
- 4) Use a board (2x4 or whatever is convenient) as a crossbar to ensure the mold is pressed up securely against the ring plate and is the same shape at the top of the mold as at the bottom.

Window Plugs

- 1) Apply mold release to the wooden window plugs.
- 2) Place plugs in the reactor windows, inserting until the plug touches the inner mold.

Pouring the Cement

In general, it was easier to mix the cement if the water was placed in the mixer before the cement. Also, it was easier to alternate adding water and cement than trying to mix 250 pounds at once.

- 1) Prepare about 275 pounds of cement in the mixer.
- 2) Place into the mold by handfuls

Make sure to compact into space between $\frac{1}{4}$ section and the window plug to make a good bond with the tabs.

- 3) Fill the cement to the tops of the molds.
- 4) Tap the sides of the molds to remove air pockets in the cement.

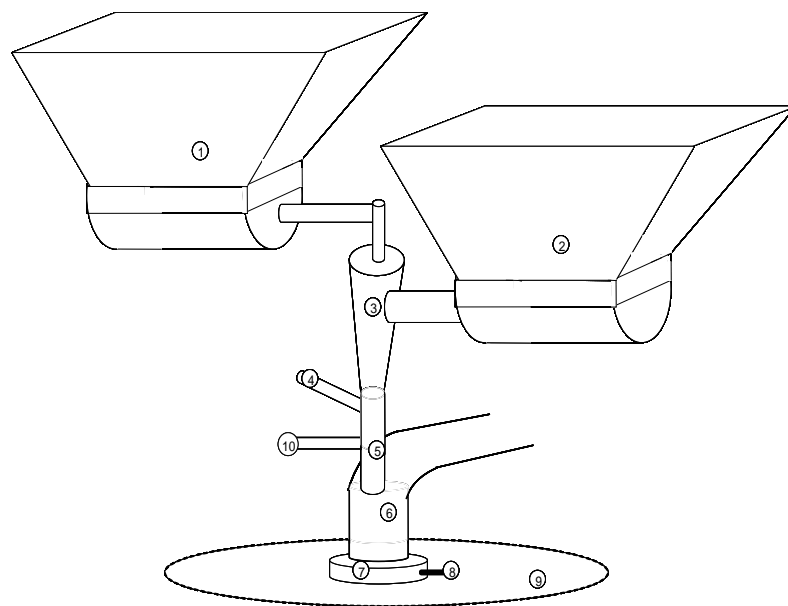
Drying

- 1) Let the entire set-up dry for 2-3 hours. This drying time depends on the wetness of the cement. When the cement on the top is dry, it is ready.
 - a. Remove the $\frac{1}{4}$ sections using the winch.
- 2) Let dry for 1-2 more hours
 - a. Remove the $\frac{1}{2}$ sections from the middle, again using the winch
- 3) Let dry for 1-2 more hours
 - a. Remove the window plugs.

Finishing Up

Repeat the above process for each section. Reassemble the reactor. The curing of the cement requires that the reactor be warmed up at 200 degF per hour to about 1200 deg.

Appendix C. Calibration of Coal and Biomass Feeders



1. Coal hopper; 2. Biomass hopper; 3. Eductor; 4. primary air inlet; 5. Primary air and fuel stream path; 6. Secondary air pipe; 7. swirl-generator; 8. Swirl-generator control; 9. Top of the reactor; 10. Natural gas inlet

Figure A. 2 The feeding system set-up of the cofiring system

Appendix D. Calibration of Air and Natural Feed Rates

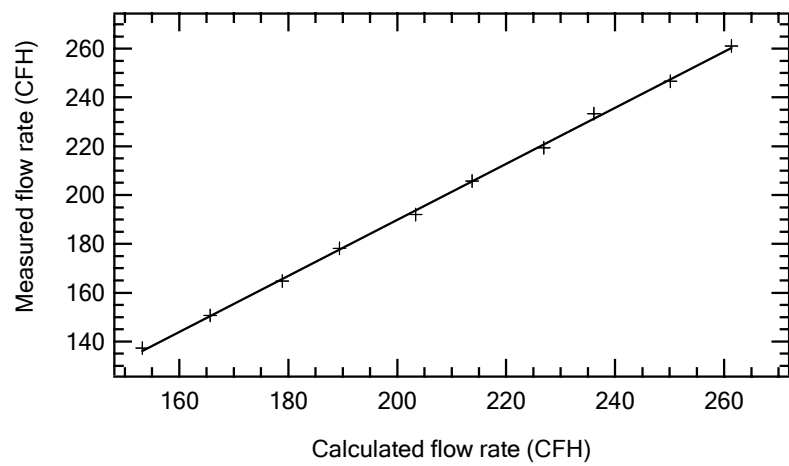


Figure A. 3 Calibration of primary air feeding

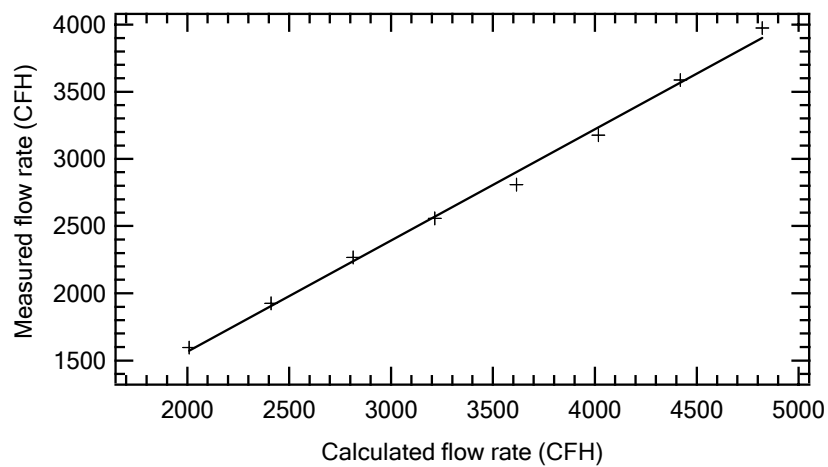


Figure A. 4 Secondary air feeding calibration

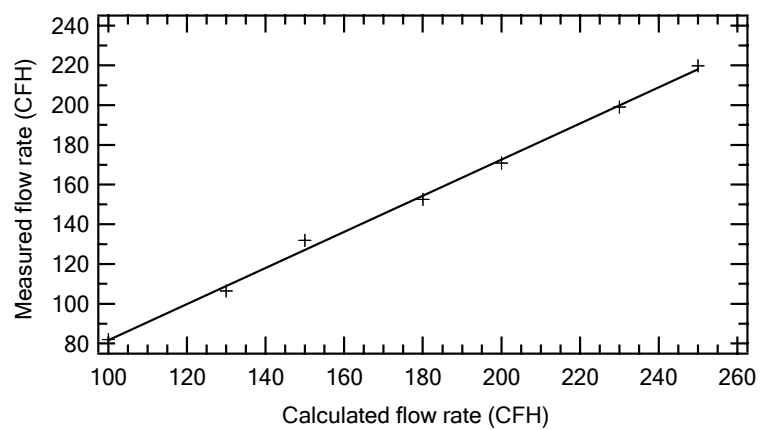


Figure A. 5 Natural gas Rotometer calibration

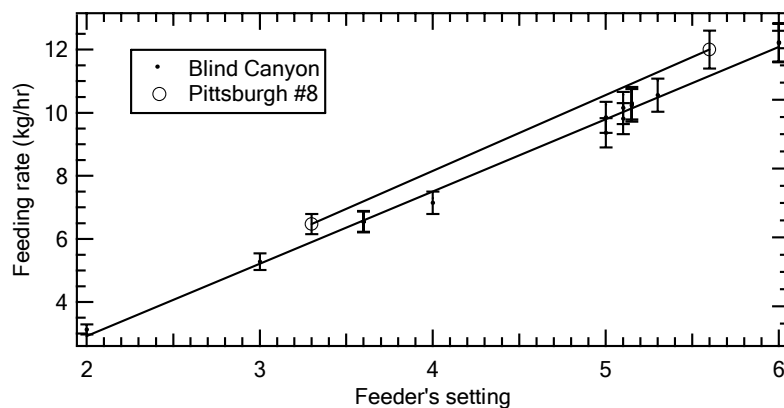


Figure A. 6 Calibration of the coal feeder

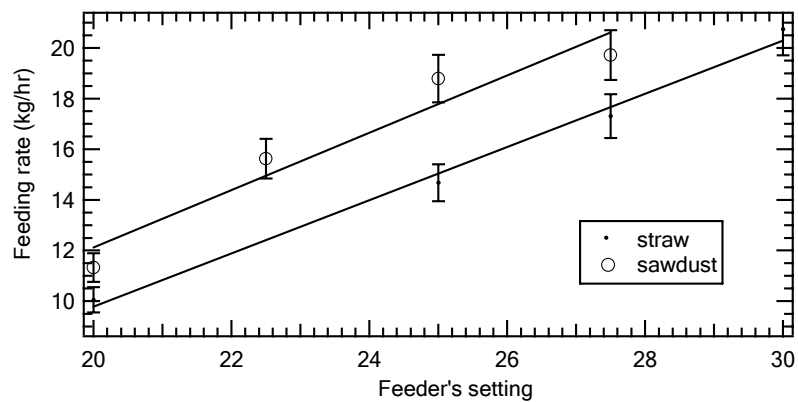


Figure A. 7 Calibration of the biomass feeder

Appendix E. Description of the Sampling Probe

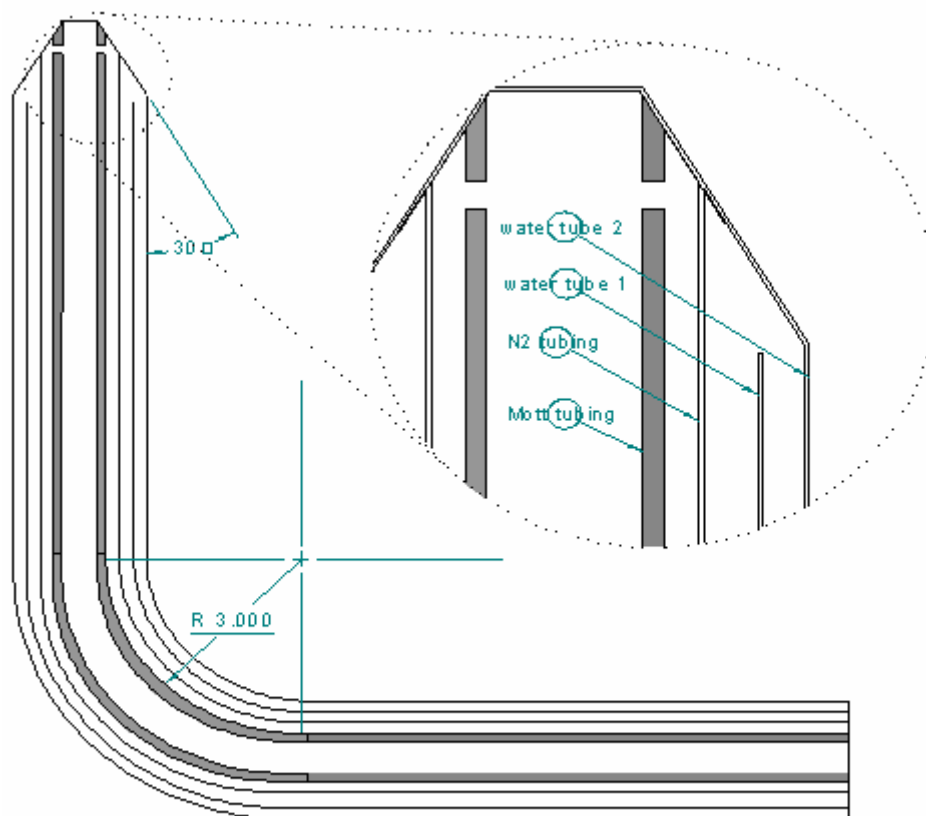


Figure A. 8 Schematic of gas sampling probe: bending (Length listed is in inch)

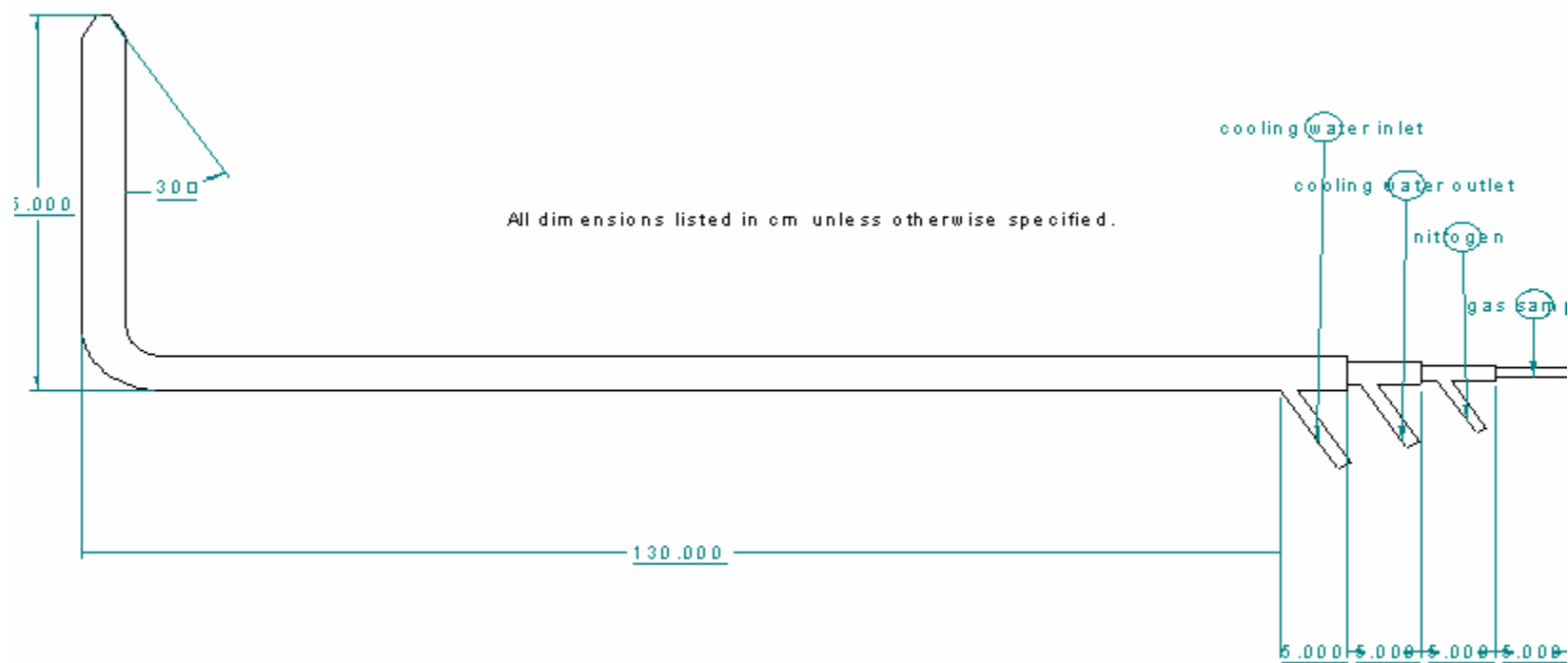
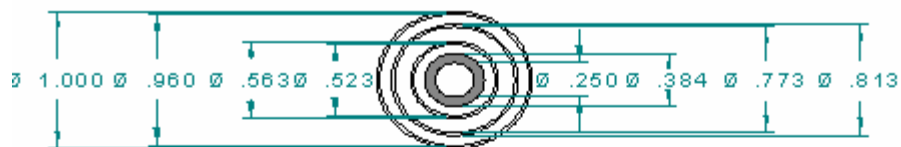


Figure A. 9 Schematic of gas sampling probe: general view



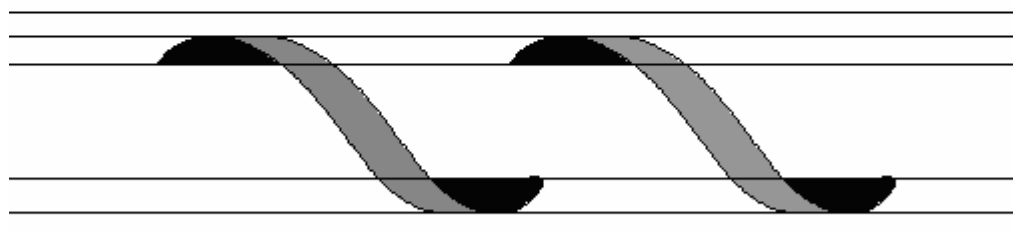
Tubing Data:

Center: ID=1/4, thickness=.067, Mott metal 316 SS, media grade 05 or 1;

2nd: OD=9/16, 25 gauge, 316 SS;

3rd: OD=13/16, 25 gauge, 316 SS;

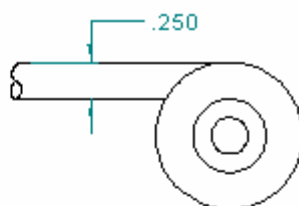
4th: OD=1, 25 gauge, 316 SS.



A ribbon is placed between each of the tubes. It is made of a thin strip of metal, providing support and improving mixing in the cooling water.

Figure A. 10 Schematic of gas sampling probe: inner structure (Length listed is in inch)

Appendix F. Description of the Cyclone and Mount



All dimensions listed are in inch.

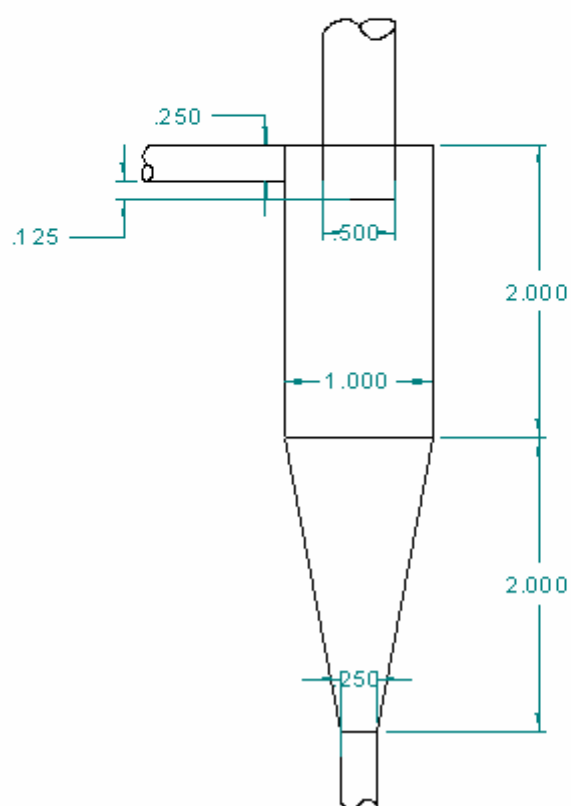


Figure A. 11 Schematic of the particle collection cyclone

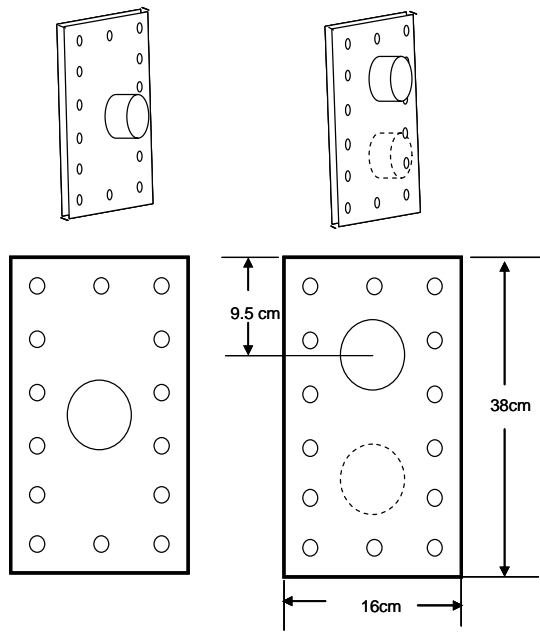


Figure A. 12

Schematic of the probe mounts

Appendix G. CFD Calculation Description

This section is based on the corresponding part in the Fluent 6.2 manual. It describes the mathematical modeling considered during the cold-flow and combustion simulations during current project.

Three dimensional modeling

Because of the highly chaotic characteristic of the fluctuations of the variables in turbulent flows, it is too computationally expensive to simulate directly in practical engineering calculations. Many manipulation methods are adopted to modify the equation sets. One of the representatives is Reynolds-averaged approach, in which the actual instant properties in the conservation are divided into their mean and fluctuating components:

$$\varphi = \overline{\varphi} + \varphi' \quad \text{G. 1}$$

After the substitution of the variable decompositions for velocities, the resulting Reynolds-averaged Navier-Stokes (RANS) equations represent transport equations for the mean flow quantities only. For steady state, isothermal 3-D turbulent airflow modeling, the mass and momentum conservation equations in Cartesian coordinates are listed as follows, dropping the overbar for convenience.

$$\frac{\partial}{\partial x_j}(\rho p_i) = 0 \quad \text{G. 2}$$

$$\begin{aligned} \frac{\partial}{\partial x_j}(\rho p_i u_j) = \\ -\frac{\partial p}{\partial x_i} + \frac{\partial}{\partial x_j} \left[\mu \left(\frac{\partial u_i}{\partial x_j} + \frac{\partial u_j}{\partial x_i} \right) - \frac{2}{3} \mu \frac{\partial u_k}{\partial x_k} \delta_{ij} \right] + F_i + \frac{\partial}{\partial x_j}(-\rho \overline{u'_i u'_j}) \end{aligned} \quad \text{G. 3}$$

On the right side, δ_{ij} is the unit tensor, and the term $-\rho \overline{u'_i u'_j}$ is designated as Reynolds stress term. This new variable is generated during the manipulation and needs to be determined in terms of known quantities by turbulence models.

Turbulent flows are characterized by fluctuating velocity fields, which make the transported quantities, such as momentum, energy, and species concentration, fluctuate as well. It is too computationally expensive to simulate these fluctuations directly in practical engineering calculations. Instead, the instantaneous governing equations can be modified into a set of equations that are computationally less expensive to solve, though modeling of additional unknown variables is involved during the manipulation.

Currently, there is no single turbulence model which is universally accepted as being superior for all classes of problems. The choice of certain models depends on many considerations including the level of accuracy required, the established practice for certain type of problem, the available computational resources, and the amount of time used.

For practical engineering calculations, the Reynolds averaged approach is generally adopted. The Reynolds-averaged Navier-Stokes (RANS) equations represent transport equations for the mean flow quantities only, with all the scales of the turbulence

being modeled. The approach of permitting a solution for the mean flow variables greatly reduces the computational effort. If the mean flow is steady, the governing equations will not contain time derivatives and a steady-state solution can be obtained economically. Furthermore, a computational advantage is seen even in transient situations, since the time step will be determined by the global unsteadiness in the mean flow rather than by the turbulence.

As one of the simplest complete models of turbulence using the Reynolds averaged approach, the standard $k - \varepsilon$ model is a two-equation model in which the solution of two separate transport equations allows the turbulent velocity and length scales to be independently determined.

Because of its robustness, economy, and reasonable accuracy for a wide range of turbulent flows, the standard $k - \varepsilon$ model gains its popularity in industrial flow and heat transfer simulations. It is a semi-empirical model, and the derivation of the model equations relies on phenomenological considerations and empiricism. The $k - \varepsilon$ turbulent models employ the Boussinesq hypothesis to relate the Reynolds stresses to the mean velocity gradients:

$$-\rho \overline{u'_i u'_j} = \mu_t \left(\frac{\partial u_i}{\partial x_j} + \frac{\partial u_j}{\partial x_i} \right) - \frac{2}{3} \left(\rho k + \mu_t \frac{\partial u_i}{\partial x_i} \right) \delta_{ij} \quad \text{G. 4}$$

where μ_t is the turbulent viscosity, defined as

$$\mu_t = \rho C_\mu \frac{k^2}{\varepsilon} \quad \text{G. 5}$$

where C_μ is a constant.

And under steady states, the scalar quantities k (turbulence kinetic energy) and ε (turbulence dissipation rate) are computed from the following equations:

$$\frac{\partial}{\partial x_i}(\rho \rho_i k) = \frac{\partial}{\partial x_i} \left[\left(\mu + \frac{\mu_t}{\sigma_k} \right) \frac{\partial k}{\partial x_i} \right] + G_k + G_b - \rho \varepsilon \quad \text{G. 6}$$

and

$$\frac{\partial}{\partial x_i}(\rho \rho_i \varepsilon) = \frac{\partial}{\partial x_i} \left[\left(\mu + \frac{\mu_t}{\sigma_\varepsilon} \right) \frac{\partial \varepsilon}{\partial x_i} \right] + C_{1\varepsilon} \frac{\varepsilon}{k} \{ G_k + (1 - C_{3\varepsilon}) G_b \} - C_{2\varepsilon} \rho \frac{\varepsilon^2}{k} \quad \text{G. 7}$$

G_k represents the generation of turbulence kinetic energy due to the mean velocity gradients, and is calculated by

$$G_k = -\overline{\rho u'_i u'_j} \frac{\partial u_j}{\partial x_i} \quad \text{G. 8}$$

G_b is the generation of turbulence kinetic energy due to buoyancy.

$$G_b = -\beta g_i \frac{u_t}{Pr_t} \frac{\partial T}{\partial x_i} \quad \text{G. 9}$$

where β is the coefficient of thermal expansion, and Pr_t is the turbulent Prandtl number with a value of 0.85.

In the isothermal air flow modeling, G_b can be omitted. The values of the constants have been determined experimentally to be $C_{1\varepsilon} = 1.44$, $C_{2\varepsilon} = 1.92$, $C_\mu = 0.09$, $\sigma_k = 1.0$, and $\sigma_\varepsilon = 1.3$.

Two dimensional combustion modeling

Continuous phase

In the axisymmetric combustion models, the conservation equations of the continuous phase are the following mass

$$\nabla \cdot (\rho \vec{v}) = S_m \quad \text{G. 10}$$

where S_m is the mass added to the continuous phase from the solid particle phase during combustion.

Momentum

$$\nabla(\rho \vec{v} \vec{v}) = -\nabla p + \nabla \cdot (\vec{\Gamma}) + \rho \vec{g} + \vec{F} \quad \text{G. 11}$$

where $\vec{\Gamma}$ is the stress tensor, defined as

$$\vec{\Gamma} = \mu \nabla \vec{v} - \rho \overline{v'v'} \quad \text{G. 12}$$

The presence of particles is assumed to have only a slight effect on the gas-phase turbulence, and FLUENT doesn't count this impact into consideration.

The energy equation can be described as

$$\nabla \cdot (\rho \vec{v} H) = \nabla \cdot \left(\frac{k_t}{c_p} \nabla H \right) + S_h \quad \text{G. 13}$$

Assuming that the Lewis number is 1, the conduction and species diffusion terms combine to be the first term on the right side of the above equation, and the second term denotes the contribution from viscous dissipation. The total enthalpy is defined as the summation of enthalpies of all the species

$$H = \sum_j Y_j H_j$$

and Y_j is the mass fraction of species j and

$$H_j = \int_{T_{ref,j}}^T c_{p,j} dT + h_j^0(T_{ref,j}) \quad \text{G. 14}$$

where $h_j^0(T_{ref,j})$ is the formation enthalpy of species j at the reference temperature $T_{ref,j}$.

Non-premixed combustion model

In the non-premixed model, the thermal chemistry is reduced to a single parameter: mixture fraction, which is the mass fraction originating from the fuel stream. The mixture fraction is the local mass fraction of burned and unburned fuel stream elements in all species. Because the atomic elements are conserved in chemical reactions, the mixture fraction is a conserved scalar quantity, whose governing transport equation does not have a source term. All thermal chemical scalars, such as mass fraction, density, and temperature, are uniquely relate to the mixture fractions. Given certain description of the reacting system, the instantaneous mixture fraction value at each point in the flow field can be used to compute the instantaneous values of individual species mole fractions, density, and temperature. In this approach, combustion is simplified into a mixing problem, avoiding the difficulties in solving large number of species transport equations involving the non-linear reaction rates. Because of its high computational efficiency, the non-premixed modeling approach has exhibited its specialty in the simulation of turbulent diffusion flames with fast chemistry, such as commercial burners, in many commercial modeling tools.

The mixture fraction fluctuates chaotically about its mean value at each point in the reactor in a turbulent environment. To characterize the mixing process and the related chemical reactions, more information is supplied regarding the fluctuations of the mixture

fraction. FLUENTTM applies the assumed shape probability density function (PDF) of the mixture fraction when the non-premixed modeling approach is used. The PDF method also accounts for the turbulence-chemistry interaction, demonstrating how the time-averaged values are related to the instantaneous values of the conserved scalars.

In the non-premixed model, the chemistry can be modeled as in chemical equilibrium or near chemical equilibrium with the laminar flamelet model, based on the assumption that the chemistry is rapid enough for chemical equilibrium to always exist at the molecular level. The equilibrium model is powerful to predict major carbonaceous or hydrogenaceous gas species under combustion conditions. It allows intermediate (radical) species prediction, dissociation effects, and rigorous turbulence-chemistry coupling. However, the equilibrium model requires that the chemical kinetics must be rapid so that the flow is near chemical equilibrium. So the species included in the equilibrium calculation should not include NO_x species, as the NO_x reaction rates are slow and should not be treated using an equilibrium assumption. Instead, NO_x concentration is predicted most accurately using the FLUENTTM NO_x postprocessor where finite rate chemical kinetics are incorporated. A detailed description of the NO_x model is available in the FLUENTTM manual.

When fuel and oxidizer are initially separated in different streams, they must be intimately contacted on a molecular level before reactions occur. Under turbulent combustion flows in the near-burner region, an assumption can be made that the overall reaction rate is dominated by the micromixing process rather than chemical kinetics. Thus, proper characterization of the mixing process is of primary importance, and the reactions can be computed using equilibrium algorithm.

The basis of the non-premixed modeling approach is the fluid instantaneous thermochemical properties (density, temperature, and elemental mass fraction) are related to a conserved scalar quantity, the mixture fraction (f). For cases with two separate inlet streams with uniform properties, named primary and secondary flows, f can be defined as

$$f = \frac{M_p}{M_p + M_s} \quad \text{G. 15}$$

Where M_p and M_s are the masses originating with the primary and secondary streams, respectively. This variable is equal to the mass fraction of the primary stream constituent. Typically, the primary source is fuel, with the secondary oxidants. All the other conserved scalars in the fluid, s , can be expressed as a function of f .

$$s = s(f) \quad \text{G. 16}$$

The validity of this approach requires the assumption that turbulent diffusivity of all the species are equal and that their boundary conditions be the same, which is acceptable when turbulent convection is overwhelming over molecular diffusion. And the species equations can be reduced equations for the mixture fraction. The time-averaged mixture fraction, \bar{f} , can be solved through the equation below.

$$\nabla(\rho \bar{v} \bar{f}) = \nabla \cdot \left(\frac{\mu_t}{\sigma_t} \nabla \bar{f} \right) + S_m \quad \text{G. 17}$$

Another equation for the mean mixture fraction variance, $\overline{f'^2}$ is given as follows:

$$\nabla(\rho \bar{v} \overline{f'^2}) = \nabla \cdot \left(\frac{\mu_t}{\sigma_t} \nabla \overline{f'^2} \right) + C_g \mu_t (\nabla^2 \bar{f}) - C_d \rho \frac{\epsilon}{k} \overline{f'^2} \quad \text{G. 18}$$

The constants, σ_t , C_g , and C_d , take the values of 0.85, 2.86, and 2.0, respectively.

The probability density function, $p(f)$, is used to describe the temporal fluctuation of f in the turbulent flows. In the axisymmetric modeling during the present project, β -function PDF is used to describe \bar{f} and $\overline{f'^2}$.

$$p(f) = \frac{f^{\alpha-1} (1-f)^{\beta-1}}{\int f^{\alpha-1} (1-f)^{\beta-1} df} \quad \text{G. 19}$$

where

$$\alpha = \bar{f} \left(\frac{\bar{f}(1-\bar{f})}{\overline{f'^2}} - 1 \right) \quad \text{G. 20}$$

$$\beta = (1-\bar{f}) \left(\frac{\bar{f}(1-\bar{f})}{\overline{f'^2}} - 1 \right) \quad \text{G. 21}$$

PDF can be used to compute time-averaged values of s under adiabatic conditions.

$$\bar{s} = \int_0^1 s(f) p(f) df \quad \text{G. 22}$$

For non-adiabatic systems including the one in current project, the instantaneous species density, elementary mass fraction, and temperature can be expressed as

$$s = s(f, H). \quad \text{G. 23}$$

And turbulent fluctuations should be considered by means of a joint PDF $p(f, H)$. However, the computation of $p(f, H)$ is not practical for most engineering applications, and significant simplification can be achieved by assuming that heat losses do not significantly impact the fluctuation of H in turbulent flows. So, $p(f)$ is still used to calculate the time-averages.

$$\bar{s} = \int_0^1 s(f, \bar{H}) p(f) df \quad \text{G. 24}$$

And the time-average of H can be determined from

$$\nabla \cdot (\rho p \bar{H}) = \nabla \cdot \left(\frac{k_t}{c_p} \nabla \bar{H} \right) + S_h \quad \text{G. 25}$$

The chemical equilibrium calculation is adopted to describe the system chemistry. This method assumes that the chemistry is rapid enough that chemical equilibrium always exists at the molecular level. FLUENT uses an algorithm based on the minimization of Gibbs free energy to compute species mole fractions from f .

Discrete phase

Particle tracking

FLUENT provides solvers for the discrete phase (particle phase for solid fuel combustion) in a Lagrangian frame of reference. The discrete phase model is based on the assumption that the condensed phase is sufficiently dilute that particle interactions and their volume fraction on the continuous phase are negligible.

Particle trajectories are predicted by integrating the force balance in a Lagrangian reference frame. In Cartesian coordinates, this equation can be expressed as follows.

$$\frac{\partial}{\partial t}(u_p) = F_D(u - u_p) + g_x \frac{(\rho_p - \rho)}{\rho_p} + F_x \quad \text{G. 26}$$

Where $F_D(u - u_p)$ is the drag force per unit particle mass, u and u_p are the fluid and particle velocities, respectively.

$$F_D = \frac{18\mu}{\rho_p d_p^2} \frac{C_D Re}{24} \quad \text{G. 27}$$

μ is the fluid molecular viscosity, and ρ and ρ_p are the fluid and particle densities, respectively. d_p is the particle diameter. Re is the relative Reynolds number, defined as

$$Re = \frac{\rho d_p |u - u_p|}{\mu} \quad G. 28$$

The drag coefficient C_D is a function of Re and shape factor a , which is ratio of the surface area of a sphere with the same volume of the particle and the actual particle surface area.

Particle size distribution is assumed to be of the Rosin-Rammler type, and the mass fraction can be expressed as

$$Y_d = e^{-(d/\bar{d})^n} \quad G. 29$$

\bar{d} is the average diameter, and n is the size distribution parameter.

Turbulent dispersion of the particles can be modeled using the particle cloud model, which is characterized with the statistical revolution of a cloud of particles about the mean trajectory. The concentration of particles within the cloud is represented by a Guassian PDF about the mean trajectory. In this model, the particles have no direct impact on the generation or dissipation of turbulence in the continuous phase.

Devolatilization

The chemical percolation devolatilization (CPD) model is used to model devolatilization process. It characterizes the behavior of rapidly heated solid fuel particles on the physical and chemical transformations of the fuel structure.

In CPD model, fuel structure is considered as a simplified lattice or network of chemical bridges that link the clusters. The process is described by modeling the cleavage of the bridges and the generation of light gas, char, and tar precursors.

A simplified illustration of the CPD model is depicted as follows:

Upon heating, the labile bridges in the coal lattice become a set of reactive bridges, with the assumption that the reactive bridges are destroyed at the same rate at which they are formed.

There are two competing paths available from the reactive bridges:

In one path, the bridges react to form side-chains. The side-chains may detach from the aromatic clusters to form light gas. As bridges between neighboring aromatic clusters are cleaved, a certain fraction of the coal becomes detached from the coal lattice. These detached aromatic clusters are the heavy-molecular-weight tar precursors that form the metaplast, which vaporizes to form coal tar. While waiting for vaporization, the metaplast can also reattach to the coal lattice matrix (crosslinking).

In the other path, the bridges react and become a char bridge, with the release of an associated light gas product. The total population of bridges in the coal lattice matrix can be represented by the sum of the char bridge and the liable bridge.

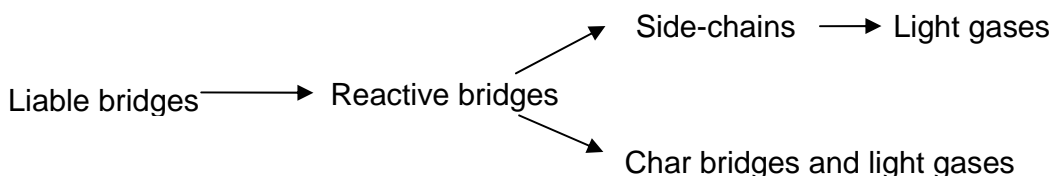


Figure A. 13 Scheme of the CPD model

The kinetic parameters in the CPD model are independent of coal structure and predefined in the submodels included which can not be input or modified during the problem setup. Five coal specific parameters to characterize the initial lattice configuration must be specified during the problem setup:

Initial fraction of bridges in the coal lattice, p_0

Initial fraction of char bridges, c_0

Lattice coordination number, $\sigma + 1$

Cluster molecular weight, $M_{w,1}$

Side-chain molecular weight, $M_{w,\delta}$

The first four of these are coal structure quantities that are obtained from NMR experimental data. The last quantity, representing the char bridges that either exist in the parent coal or are formed very early in the devolatilization process, is estimated based on the coal rank.

Heat transfer to the particle during the devolatilization process can be expressed in the equation below.

$$m_p c_p \frac{dT_p}{dt} = h A_p (T_\infty - T_p) + \frac{dm_p}{dt} h_{fg} + A_p \epsilon_p \sigma (\theta_R^4 - T_p^4) \quad \text{G. 30}$$

The three terms on the right side account for the contribution from convection, heat consumed during devolatilization, and radiation. m_p , T_p , A_p , and ϵ_p are the mass, temperature, surface area, and emissivity of the particle, respectively. θ_R is the radiation temperature, as defined by

$$\theta_R = \left(\frac{I}{4\sigma} \right)^{\frac{1}{4}} \quad \text{G. 31}$$

and I is the radiation intensity.

The discrete coordinate radiation model is used, which is amenable to numerical methods consistent with the fluid mechanics

Char oxidation

After the volatile component of the particle is completely emitted, a surface reaction begins and consumes the combustible fraction of the particle.

Because of the large size of the biomass char, it is assumed that the surface reaction proceeds at a rate determined by the diffusion of the gaseous oxidant to the surface of the particle.

$$\frac{dm_p}{dt} = -4\pi\pi_p D_{i,m} \frac{Y_{ox} T_\infty \rho}{S_b (T_p + T_\infty)} \quad \text{G. 32}$$

where $D_{i,m}$, Y_{ox} , ρ , and S_b are the diffusion coefficient for oxidant in the bulk (m^2/s), local mass fraction of oxidant in the gas, gas density, and stoichiometric ratio of the char-oxidant reaction.

For coal char, the kinetic/diffusion-limited rate model is used, which assumes that the surface reaction rate is determined either by kinetics or a diffusion rate. In this method, a diffusion rate coefficient

$$D_0 = C_1 \frac{[(T_p + T_\infty)/2]^{0.75}}{d_p} \quad \text{G. 33}$$

and a kinetic rate

$$R = C_2 e^{-(E/RT_p)} \quad \text{G. 34}$$

are weighted to yield a char combustion rate of

$$\frac{dm_p}{dt} = -A_p \frac{\rho R T_\infty Y_{ox}}{Mw_{ox}} \frac{D_0 R}{(D_0 + R)} \quad \text{G. 35}$$

where Mw_{ox} is the molecular weight of oxidant.

Both char combustion models assume a constant particle size during calculation. Similar to the devolatilization process, the heat and mass transfer balance is modeled by the following equation.

$$m_p c_p \frac{dT_p}{dt} = h A_p (T_\infty - T_p) + f_h \frac{dm_p}{dt} H_{rxn} + A_p \epsilon_p \sigma (\theta_R^4 - T_p^4) \quad \text{G. 36}$$

and H_{rxn} is the heat released by the surface reactions. f_h is the heat fraction absorbed by the particles.

NO_x formation mechanism

In FLUENT, NO_x concentrations are calculated by post-processing predictions from reacting flow simulations. This is because compared to carbon, hydrogen, and oxygen, nitrogen content is so small that the reaction involving NO_x have no significant impact on the concentrations of major species or temperature in the flow fields. Since fuel-NO_x accounts for more than 90% from total NO_x emissions in commercial low-grade fuel combustion facilities, only fuel-NO_x submodel is used in current project.

In the fuel-NO_x submodel, NO_x intermediates are assumed to be either HCN or NH₃, and the mechanisms to calculate NH₃ or HCN are similar. In the NO_x submodel description part, except special marks, i represents HCN or NH₃.

The mass transport equations for NO, HCN, and NH₃ species are solved, taking into account convection, diffusion, production and consumption of these nitrogen species.

$$\nabla \cdot (\rho \bar{v} Y_i) = \nabla \cdot (\rho D_i) + S_i$$

where Y is the mass fraction, and i represents HCN, NH₃, and NO, respectively. S is the source term for fuel-NO_x mechanisms described next.

Assuming that fuel-N is distributed between volatiles and char, with separate fuel-N content definitions, two variations of fuel-NO_x mechanisms for solid fuels are included.

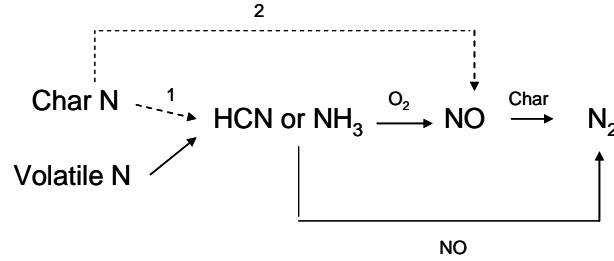


Figure A. 14 Schemes of the fuel-NO_x model in FLUENT™

In Scheme 1, all char-bound nitrogen converts to HCN or NH₃,

$$S_{char,i} = \frac{S_c Y_{N,char} Mw_i}{Mw_N V} \quad G. 37$$

$$S_{char,NO} = 0 \quad G. 38$$

where S_c is char burnout rate, and V is cell volume.

And char-N converts to NO in Scheme 2.

$$S_{char,i} = 0 \quad G. 39$$

$$S_{char,NO} = \frac{S_c Y_{N,char} Mw_{NO}}{Mw_N V} \quad G. 40$$

In these schemes, multiples mechanisms affect the concentrations of HCN, NH₃ and NO. The source terms in the transport equations can be expressed as:

$$S_i = S_{pvc,i} + S_{i,1} + S_{i,2}$$

$$S_{NO} = S_{C,NO} + S_{NO,1} + S_{NO,2} + S_{NO,3}$$

The nomenclature is explained in the following discussions.

HCN or NH₃ produced from nitrogen bound in both volatiles and char, and the overall source is

$$S_{pvc,i} = S_{V,i} + S_{C,i} \quad \text{G. 41}$$

From volatiles

$$S_{V,i} = S_V Y_{NV} \frac{Mw_i}{Mw_N} \quad \text{G. 42}$$

where S_V is rate of volatiles production, and Y_{NV} is mass fraction of nitrogen in the volatiles.

If all char-N converts to HCN or NH₃, the rate can be expressed as

$$S_{C,i} = S_C Y_{NC} \frac{Mw_i}{Mw_N} \quad \text{G. 43}$$

with

$$S_{C,NO} = 0 \quad \text{G. 44}$$

where S_C is the rate of char production, and Y_{NC} is mass fraction of nitrogen in the char.

If all char-N converts to NO, the corresponding expressions are

$$S_{C,i} = 0 \quad \text{G. 45}$$

$$S_{C,NO} = S_C Y_{NC} \frac{Mw_i}{Mw_N} \quad \text{G. 46}$$

The depletion rates of HCN or NH₃ can be calculated by the following

$$S_{i,1} = -R_1 \frac{Mw_i P}{RT} \quad \text{G. 47}$$

$$S_{i,2} = -R_2 \frac{Mw_i P}{RT} \quad \text{G. 48}$$

Where P and is the pressure in Pa. R_1 and R_2 represent the oxidation to NO and reduction to N₂, respectively.

$$R_1 = A_1 X_i X_{O_2}^a e^{-E_1/RT} \quad \text{G. 49}$$

$$R_2 = A_2 X_i X_{NO} e^{-E_2/RT} \quad \text{G. 50}$$

where A_1 is $1 \times 10^{10} s^{-1}$ for HCN, and $4 \times 10^6 s^{-1}$ for NH₃, and A_2 is $3 \times 10^{12} s^{-1}$ for HCN, and $1.8 \times 10^8 s^{-1}$ for NH₃. E_1 is 67 kcal/gmol for HCN and 32 kcal/gmol for NH₃. E_2 is 60 kcal/gmol for HCN and 27 kcal/gmol for NH₃.

a is the oxygen reaction order, which is uniquely related to oxygen mole fraction (X_{O_2}) in the flame..

$$a = \begin{cases} 1.0 & X_{O_2} \leq 4.1 \times 10^{-3} \\ -3.95 - 0.9 \ln X_{O_2} & 4.1 \times 10^{-3} < X_{O_2} < 1.1 \times 10^{-2} \\ -0.35 - 0.1 \ln X_{O_2} & 1.1 \times 10^{-2} < X_{O_2} < 0.03 \\ 0 & X_{O_2} \geq 0.03 \end{cases} \quad \text{G. 51}$$

The NO source terms can be expressed as

$$S_{NO,1} = -S_{i,1} \frac{Mw_{NO}}{Mw_i} \quad \text{G. 52}$$

$$S_{NO,2} = -S_{i,2} \frac{Mw_{NO}}{Mw_i} \quad \text{G. 53}$$

$S_{NO,3}$ denotes the source term contributed by the NO consumption on the char surface.

$$S_{NO,3} = \frac{c_s A_{BET} Mw_{NO} R_3}{1000} \quad \text{G. 54}$$

where c_s is the concentration of particles, and A_{BET} is the BET surface area. R_3 is the rate of the heterogeneous reaction of NO reduction.

$$R_3 = A_3 e^{-E_3/RT} \bar{P}_{NO} \quad \text{G. 55}$$

A_3 is 230 mole/atm/m²_{BET}/s, and E_3 is 34100 cal/mol, and \bar{P}_{NO} is mean NO partial pressure (atm).

During the foregoing discussion of models for fuel-NO_x production, the instantaneous values for species mass fraction and temperature have been used. However, RANS equations only provide time-averaged values, and the relationship among NO_x formation, temperature, and species concentrations are highly nonlinear. Hence, significant error will occur if time-averaged composition and temperature are employed to predict the mean NO_x formation rate. FLUENT uses the PDF approach to model the mean turbulent reaction rate.

Appendix H. Additional Cofiring Maps

This section includes major gas species, CO, CO₂, and O₂, spatial profiles from cofiring tests of Test 70SD30BC, Test 70SD30P, and Test 70S30P.

Species maps of the two cofiring tests: Test 70SD30BC and Test 70SD30P

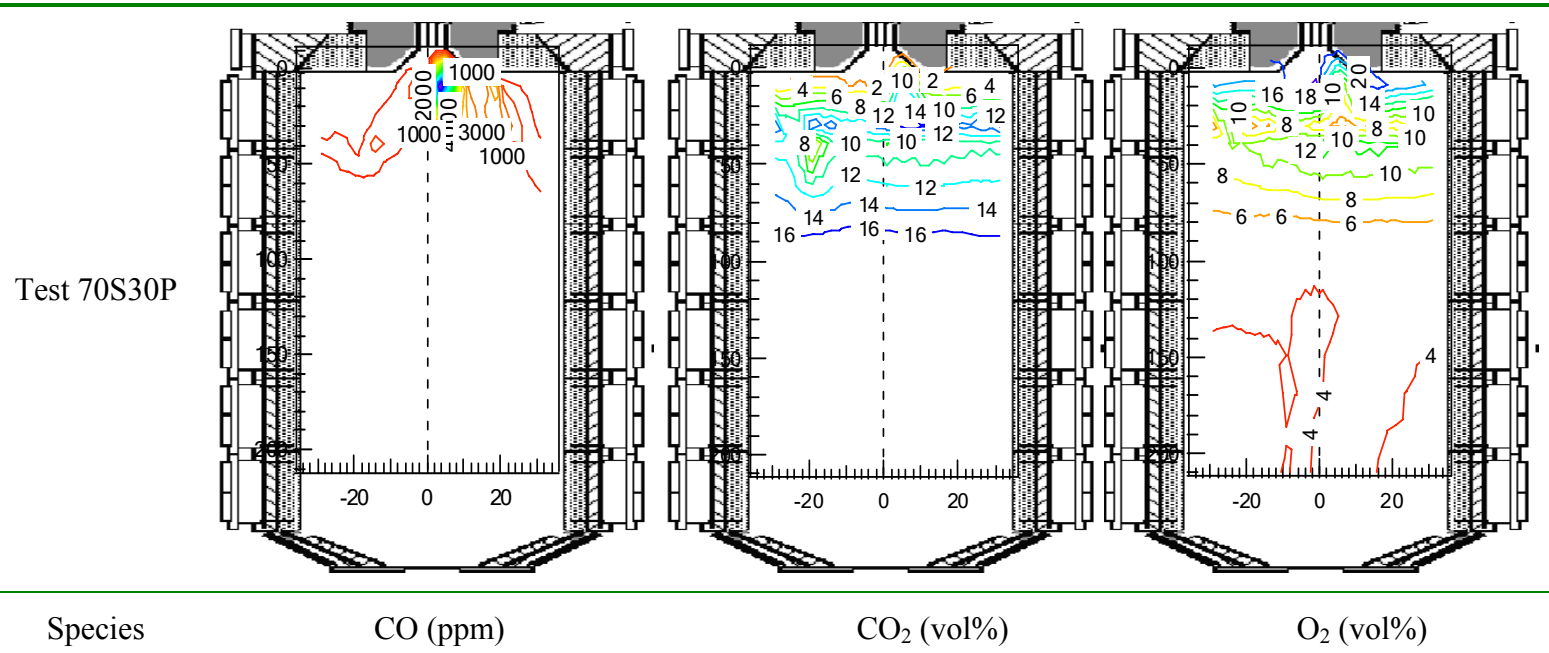


Figure A. 16 Species maps of the cofiring test of 70S30P

Appendix I. Derivation of the HCN, NH₃ Profiles Equation

This is a short derivation for the concentration of any species in the fuel-rich eddies based on measured average and assumed fuel-lean oxygen concentrations.

Designate the number of moles of fuel-rich and fuel-lean gases as N_{fr} and N_{fl} , respectively. The total amount of any species that exists only in the fuel-rich eddies ($N_{i, fr}$) can be determined by a material balance as follows:

$$N_{i, fr} = x_{i, fr} N_{fr} = x_{i, meas} N_{measured} = x_{i, meas} (N_{fr} + N_{fl}) \quad \text{I. 1}$$

Solving this equation for $x_{i, fr}$ yields

$$x_{i, fr} = x_{i, meas} \left(1 + \frac{N_{fl}}{N_{fr}}\right) \quad \text{I. 2}$$

Since, by definition, oxygen exists only in fuel-lean eddies (This is not exactly correct in that carbon dioxide and water dissociate to produce oxygen at high temperatures even if the overall stoichiometry is fuel rich. However, the amounts of oxygen produced by this mechanism are very small at the temperatures of this system (< 2000 K everywhere) and this source of oxygen is ignored in this analysis), a similar balance for oxygen leads to

$$\begin{aligned} x_{O_2, fl} &= x_{O_2, meas} \left(\frac{N_{fr}}{N_{fl}} + 1 \right) \\ \Rightarrow \frac{N_{fl}}{N_{fr}} &= \left(\frac{x_{O_2, fl}}{x_{O_2, meas}} - 1 \right)^{-1} = \left(\frac{x_{O_2, fl} - x_{O_2, meas}}{x_{O_2, meas}} \right)^{-1} = \frac{x_{O_2, meas}}{x_{O_2, fl} - x_{O_2, meas}} \end{aligned} \quad \text{I. 3}$$

Solving this equation for the ratio of fuel-lean moles to fuel-rich moles leads to

$$X_{O_2,fl} = X_{O_2,meas} \left(\frac{N_{fr}}{N_{fl}} + 1 \right)$$

$$\Rightarrow \frac{N_{fl}}{N_{fr}} = \left(\frac{X_{O_2,fl}}{X_{O_2,meas}} - 1 \right)^{-1} = \left(\frac{X_{O_2,fl} - X_{O_2,meas}}{X_{O_2,meas}} \right)^{-1} = \frac{X_{O_2,meas}}{X_{O_2,fl} - X_{O_2,meas}} \quad \text{I. 4}$$

Substituting this expression back into the second expression above (for the mole fraction of species i in the fuel-rich eddies) yields

$$X_{i, \text{fuel-rich eddy}} = X_{i, \text{measured}} \frac{X_{O_2, \text{fuel-lean eddy}}}{X_{O_2, \text{fuel-lean eddy}} - X_{O_2, \text{measured}}} \quad \text{I. 5}$$

Note that the dimensions of this equation work out regardless of the units in which species i is measured so long as they are the same units (ppm, mole fraction, or any other units).

Some notes on the equation:

This equation may not work for fuel-rich species such as CO that may exist in finite concentrations in fuel-lean regions because of slow kinetic conversion rates.

Note that the measured O₂ concentration must always be less than the O₂ concentration in the fuel-lean regions or, if there are no fuel-lean regions, the concentrations are equal.

Therefore, the equation is well behaved (never gives negative values for the fuel-rich regions and only gives infinite values in the limit of no fuel-rich region).

The fraction in this expression increases monotonically with decreasing value of the numerator, meaning the proportionality constant that corrects the measured value to the fuel-rich value is a minimum if pure air is assumed.

In reality, of course, there are eddies with varying amounts of fuel-rich species and oxygen. This approach yields the average values, not the peak values, assuming that eddy populations are distinguished by the presence or lack of oxygen (or by equivalence ratio greater or less than one).

Appendix J. Calculations with the GRI-Mech 3.0 Mechanism

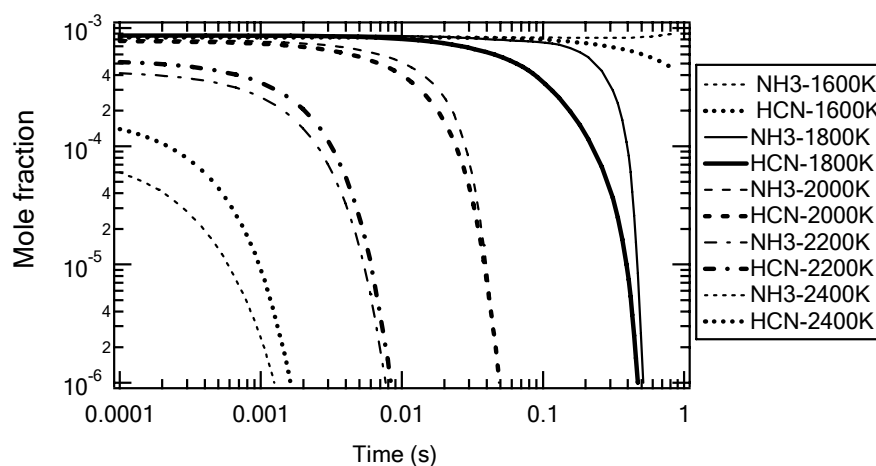


Figure A. 17 Comparison the thermal stability of HCN and NH_3 in the fuel-rich region.

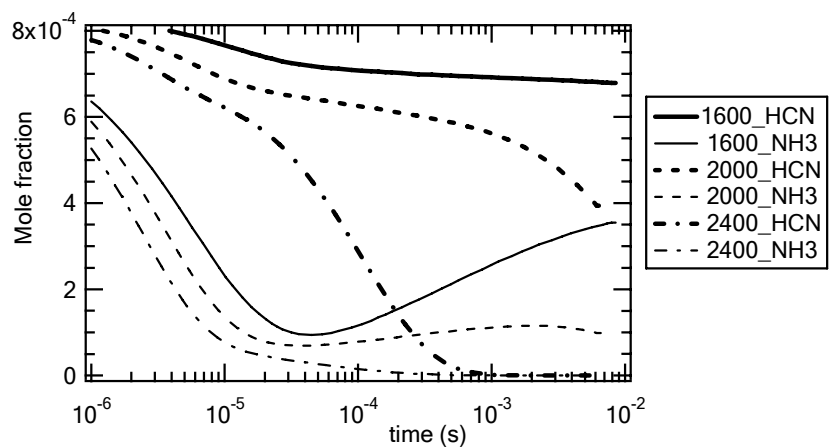


Figure A. 18 Comparison the chemical reactivity of HCN (Case 2) and NH_3 (Case 3) in the flame front.

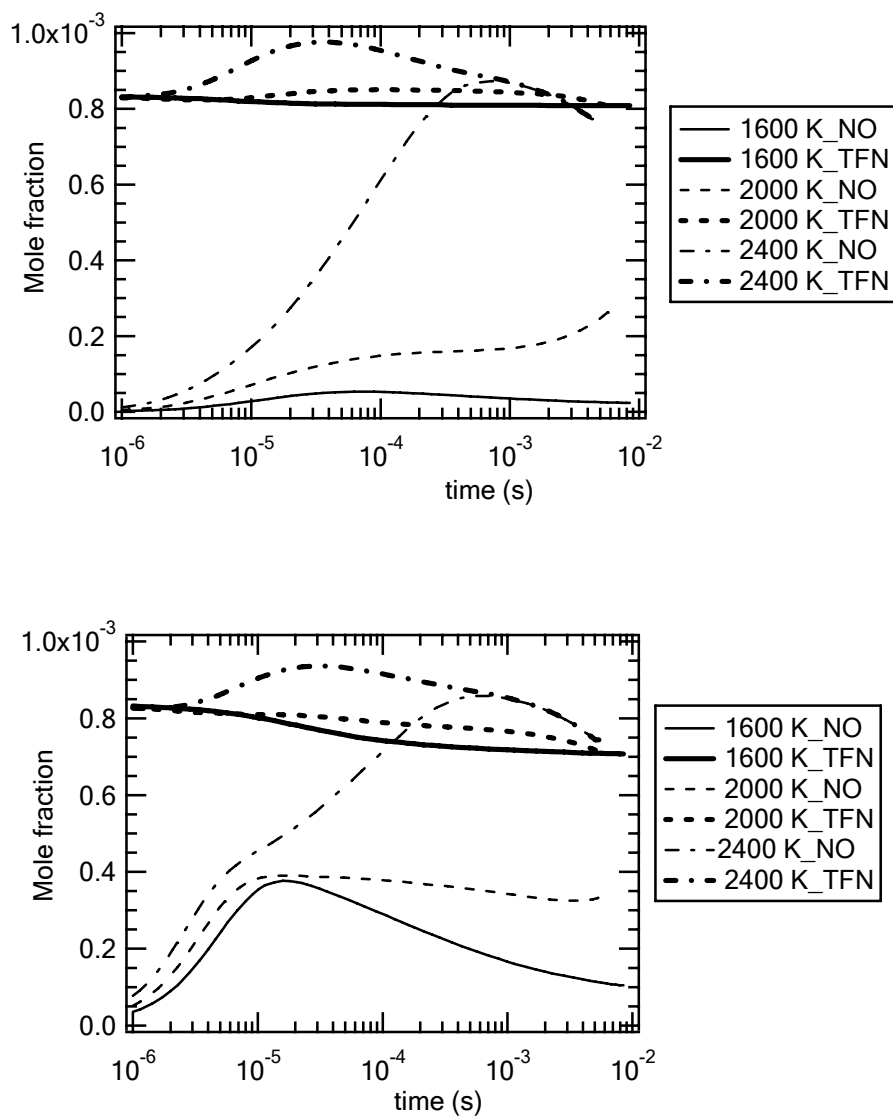


Figure A. 19

Calculated profiles of TFN and NO from cases where only one type of NO_x intermediate exists in the initial mixture, with lines representing results from HCN mixtures (Case 2, top) and markers denoting NH₃ blends (Case 3, bottom).